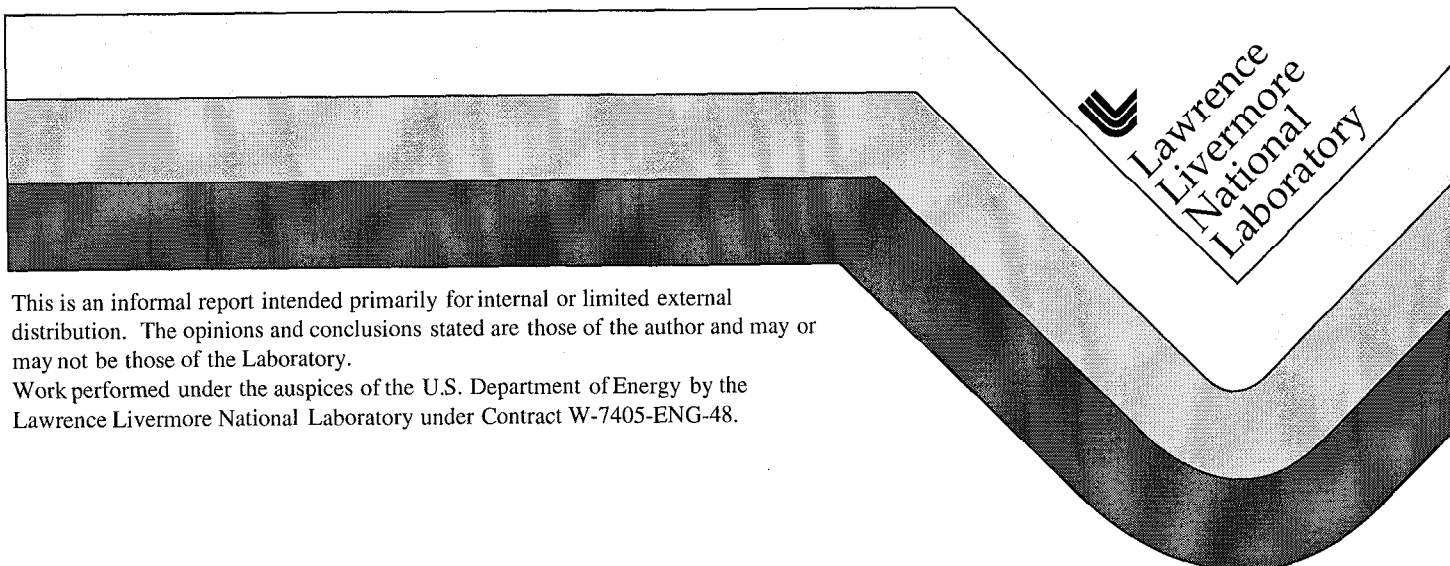


Development of Integrated Mechanistically-Based Degradation-Mode Models for Performance Assessment of High-Level Waste Containers

J. Farmer, D. McCright,
J. S. Huang, A. Roy,
K. Wilfinger, R. Hopper,
F. Wang, P. Bedrossian,
J. Estill, J. Horn

February 8, 1999



DISCLAIMER

This document was prepared as an account of work sponsored by an agency of the United States Government. Neither the United States Government nor the University of California nor any of their employees, makes any warranty, express or implied, or assumes any legal liability or responsibility for the accuracy, completeness, or usefulness of any information, apparatus, product, or process disclosed, or represents that its use would not infringe privately owned rights. Reference herein to any specific commercial product, process, or service by trade name, trademark, manufacturer, or otherwise, does not necessarily constitute or imply its endorsement, recommendation, or favoring by the United States Government or the University of California. The views and opinions of authors expressed herein do not necessarily state or reflect those of the United States Government or the University of California, and shall not be used for advertising or product endorsement purposes.

This report has been reproduced
directly from the best available copy.

Available to DOE and DOE contractors from the
Office of Scientific and Technical Information
P.O. Box 62, Oak Ridge, TN 37831
Prices available from (615) 576-8401, FTS 626-8401

Available to the public from the
National Technical Information Service
U.S. Department of Commerce
5285 Port Royal Rd.,
Springfield, VA 22161

DEVELOPMENT OF INTEGRATED MECHANISTICALLY-BASED DEGRADATION-MODE MODELS FOR PERFORMANCE ASSESSMENT OF HIGH-LEVEL WASTE CONTAINERS

Joseph Farmer, Daniel McCright, Jia-Song Huang, Ajit Roy,
Keith Wilfinger, Robert Hopper, Francis Wang, Peter Bedrossian, John Estill and JoAnne Horn
University of California, Lawrence Livermore National Laboratory
Livermore, California 94550

INTRODUCTION

Background

A key component of the Engineered Barrier System (EBS) being designed for containment of spent-fuel and high-level waste at the proposed geological repository at Yucca Mountain, Nevada is a two-layer canister. In this particular design, the inner barrier is made of a corrosion resistant material (CRM) such as Alloy 825, 625 or C-22, while the outer barrier is made of a corrosion-allowance material (CAM) such as A516 Gr 55, a carbon steel, or Monel 400. At the present time, Alloy C-22 and A516 Gr 55 are favored.

Environment and Modes of Degradation

Initially, the containers will be hot and dry due to the heat generated by radioactive decay. However, the temperature will eventually drop to levels where both humid air and aqueous phase corrosion will be possible. As the outer barrier is penetrated, corrosion of the underlying CRM will initiate. This is illustrated by Figure 1. In the case of Alloys 825, 625 and C-22, it is believed that a crevice will have to form before significant penetration of the CRM could occur. The crevice creates a localized environment with suppressed pH and elevated chloride. Jones and Wilde have prepared solutions of FeCl_2 , NiCl_2 and CrCl_3 to simulate such localized environments and measured substantial pH suppression [1]. Wang has made similar measurements with FeCl_3 solutions, which are reported here. As pointed out by McCoy, the measured pH in active, artificial crevices is: 3.3 to 4.7 if the crevice is formed with carbon steel; 2.4 to 4.0 if the crevice is formed with a Fe-Cr alloy, and ≤ 2.3 if the crevice is formed with a stainless steel [2,3]. It must be noted that crevice corrosion of candidate CRM's has been well documented. For example, Lillard and Scully have induced crevice corrosion in Alloy 625 during exposure to artificial sea water [4], though others have observed no significant localized attack in less severe environments [5]. Haynes International has published corrosion rates of Alloys 625 and C-22 in artificial crevice solutions (5-10 wt. % FeCl_3) at various temperatures (25, 50 and 75°C) [6,7]. In this case, the observed rates for Alloy C-22 appear to be due to passive dissolution. It appears that Alloy C-22 must be at an electrochemical potential above the repassivation potential to initiate localized corrosion (LC).

Selection of Materials for Inner and Outer Barriers (CAM and CRM)

From the standpoint of corrosion engineering, the current container design has several desirable attributes. For example, the thick outer barrier (10 cm of A516 Gr 55) enables construction of a

relatively low-cost, robust container which will provide substantial mechanical integrity during emplacement. Furthermore, it will provide shielding, thereby reducing the effect of radiolysis products such as H_2O_2 on the electrochemical corrosion potential (E_{corr}) [8]. After penetration of the CAM, it will suppress the electrochemical potential of the CRM at the point of penetration (crevice mouth). The thinner inner barrier (2 cm of Alloy C-22) then provides superior corrosion resistance. Note that Ti-based alloys were considered for the inner barrier, but are much more susceptible to hydrogen embrittlement (HE). Other have expressed concern that galvanic coupling of the inner barrier (CRM) to a less-noble outer barrier (CAM) could result in cathodic hydrogen charging of the CRM. Alloys 825 and 625 are more prone to localized corrosion (LC) than Alloy C-22 [6,7]. The unusual LC resistance of Alloy C-22 is believed to be due to the additions of both Mo and W, which stabilize the passive film at very low pH [9]. Consequently, this material exhibits a very high repassivation potential (E_{pass}), approaching the potential required for O_2 evolution [10]. Note that E_{pass} is accepted by most corrosion scientists as the threshold for LC initiation. Furthermore, preliminary predictions made with a modified pit stifling criterion predict that the maximum pit depth, Δx , is less than the wall thickness (2 cm) over the range of pH extending from -1 to 10. In experiments with simulated crevice solutions (10 wt. % FeCl_3), very low (passive) corrosion rates are observed. Finally, no significant attack of Alloy C-22 was observed in crevices exposed to simulated acidified water (SAW) for one year. These tests were conducted in the Long Term Corrosion Test Facility (LTCTF) at Lawrence Livermore National Laboratory (LLNL).

Ceramic Coating for Outer Barrier

The CAM may be protected with a thermally-sprayed, ceramic coating [11]. Unlike metallic alloys, the candidate ceramic coatings are thermodynamically stable oxides. Such materials exhibit very slow rates of dissolution, which was a primary consideration in the recent selection of a ceramic waste form for immobilization of plutonium. Porosities of less than 2% have been achieved with the high-velocity oxygenated fuel (HVOF) process. Samples coated with Al_2O_3 - TiO_2 have shown no corrosion at the ceramic-CAM interface after exposure to concentrated J-13 water at elevated temperature for six (6) months. It is assumed that the inhibition of corrosion is primarily due to the impedance of O_2 transport through the pores. Liquid-filled pores provide greater impedance to O_2 transport than gas-filled pores. It may be possible to completely eliminate transport through the use of inorganic sealants. These coatings have also proven to be mechanically robust.

Model Development

A variety of research is being conducted at LLNL, directed towards degradation of the CAM and CRM. Corrosion modeling for Total System Performance Assessment (TSPA) is a key component of this work. Models include simple correlations of experimental data [12], as well as detailed mechanistic models necessary for believable long-term predictions [13,14]. Several interactive modes of corrosion are illustrated by Figure 2. This publication describes: (a) a corrosion-inhibition and spallation model to account for the effects of the ceramic coating on CAM life; (b) a crevice corrosion model based upon mass transport and solution equilibria for prediction of pH suppression and Cl^- elevation in the crevice; (c) deterministic and probabilistic models for pit initiation; (d) deterministic models for pit growth and stifling; (e) a criterion for

the initiation of stress corrosion cracking at a pre-existing flaw such as a pit; and (f) a deterministic model for thermal embrittlement of the CAM based upon the diffusion of phosphorous, P, to grain boundaries. Confirmatory testing to support these mechanistic models such as the development of in situ chemical sensors (pH microprobes) is also discussed.

Testing Program

Models are also supported by a variety of other corrosion tests. For example, atmospheric corrosion is being investigated under constant temperature and various constant relative humidities by thermogravimetric analysis (quartz microbalance, TGA), and with a variety of surface analytical probes. Electrochemical testing includes both potentiostatic and cyclic polarization, as well as ac impedance spectroscopy. Mechanical testing involves double cantilever beam (DCB) experiments, slow strain rate testing (SSRT) and other techniques.

The Long Term Corrosion Test Facility (LTCTF) appears to be the most complete source of corrosion data for Alloy C-22 in environments relevant to the proposed high-level waste repository at Yucca Mountain. This facility is equipped with an array of nearly cubic fiberglass tanks. Each tank has a total volume of ~2000 liters and is filled with ~1000 liters of aqueous test solution. The solution in a particular tank is controlled at either 60 or 90°C, purged with air flowing at approximately $150 \text{ cm}^3 \text{ min}^{-1}$, and agitated. The test environments used in the LTCTF are referred to as: Simulated Dilute Water (SDW); Simulated Concentrated Water (SCW); Simulated Acidified Water (SAW); and Simulated Cement-Modified Water (SCMW). The descriptions and compositions of these solutions are summarized in Table 1. Four generic types of samples, U-bends, crevices, weight loss samples and galvanic couples, are mounted on insulating racks and placed in the tanks. Approximately half of the samples are submersed, half are in the saturated vapor above the aqueous phase, and a limited number at the water line. It is important to note that condensed water is present on specimens located in the saturated vapor. In regard to Alloys 516 Gr 70 [UNS K01800; 0.2C-0.5Mn-Fe(bal)] and C-22 [UNS N06022; 21Cr-13Mo-4Fe-3W-2Co-Ni(bal)], the rates of penetration observed in the LTCTF during the first six months of testing are included in the analyses presented here. The loss in weight and change in dimension were measured with electronic instruments calibrated to traceable standards. Since all data was digitally transferred to computer, the possibility of human key-punch error was minimized. Thus far, more than 16,000 samples have been incorporated into tests.

GENERAL CORROSION

Dry Oxidation of the Outer Barrier (CAM)

Degradation of the CAM is assumed to occur by abiotic processes that can be categorized as: (a) dry oxidation; (b) humid air corrosion; (c) aqueous phase corrosion; (d) stress corrosion cracking; or (e) thermal embrittlement. In the case of aqueous phase corrosion, attack can be general or localized. It is now assumed that general corrosion will occur below pH 10, whereas pitting is assumed to occur under more alkaline conditions. Correlations of data from the LTCTF and TGA are being developed to predict rates of generalized corrosion in the simulated NFE (SDW, SCW, SAW, and SCMW). CAM corrosion would be impeded by the presence of a thermally-sprayed ceramic coating. Ultimately, the impact of microbial influenced corrosion

will also be quantified. It should be noted that it may not be possible to maintain the environmental requirements for pitting of the CAM since the reactants will be consumed by the corrosion process. Bulk water-like conditions would have to be maintained.

The model favored for dry oxidation of the CAM (A516 Gr 55) was developed by Henshall [15]. This model is represented by Equations 1a through 1e.

$$x_{ox}(t)^2 = x_{ox}(t_0)^2 + 2k_p \int_{t_0}^t \exp[-Q/RT(t)] dt \quad (1a)$$

$$k_p = 4.3 \times 10^{-5} \frac{cm^2}{s} \quad (1b)$$

$$Q = 104 \frac{kJ}{mol} \quad (1c)$$

$$R = 8.314 \frac{J}{mol K} \quad (1d)$$

where x_{ox} is the oxide thickness, k_p is a rate constant, Q is the apparent activation energy, R is the universal gas constant, T is the absolute temperature, and t is time. Note that this expression predicts an oxide thickness of only 6.24 μm after 1000 years of dry oxidation at a fixed temperature of 150°C.

Corrosion of the Outer Barrier (CAM) in Aqueous and Vapor Phases

Data from the LTCTF is being used as the basis of empirical corrosion models for the aqueous phase and air saturated with water vapor. Data from the TGA and humidity chamber studies will be used in models for corrosion where the RH is less than one hundred percent. The following linear equation has been used to correlate the penetration rate data for Alloy 516:

$$\ln\left(\frac{\Delta p}{\Delta t}\right) = b_0 + b_1\left(\frac{1000}{T + 273}\right) + b_2(pH) + b_3(C_{NaCl}) \quad (2a)$$

where $\Delta p/\Delta t$ is the apparent penetration rate ($\mu m y^{-1}$); T is the temperature (°C); and C_{NaCl} is the equivalent concentration of NaCl (wt. %) [12]. Note that the "equivalent NaCl concentration" is used as an independent variable in correlations. This parameter is defined in terms of the concentration of free chloride as follows:

$$C_{NaCl} = C_{Cl^-} \left(1 + \frac{22.98977}{35.453}\right) \quad (2b)$$

Alternatively, the concentration of free chloride can be used, adjusting the coefficient b_3 accordingly. Within the bounds of experimental observations for Alloy 516, the coefficients are defined as given in Table 2. Six regression analyses were performed: (Case 1) all data correlated together; (Case 2) vapor phase, weight loss samples; (Case 3) aqueous phase, weight

loss samples; (Case 4) vapor phase, crevice samples; (Case 5) aqueous phase, crevice samples; and (Case 6) water line, weight loss samples. These data are illustrated graphically in Figure 3. The specific data used for Cases 2 through 6 are given in Tables 3 through 7, respectively. In Cases 1, 3, 5, and 6, which all pertain to aqueous phase exposures, the positive values of b_1 indicate that the penetration rates decrease with increasing temperature. This very surprising result may be due to either salt deposition or decreased oxygen solubility. As will be seen in the subsequent section, the correlation for Alloy C-22 indicates that rates increase with temperature, as would normally be expected.

Delay Mechanisms for Corrosion of the Outer Barrier (CAM)

Engineers are exploring several mechanisms to delay corrosive attack of the CAM by dripping water, including drip shields and ceramic coatings. Ceramic coatings deposited with HVOF have exhibited a porosity of only 2% at a thickness of 0.15 cm. A model has been developed to account for the inhibition of corrosion by these coatings. It is assumed that the overall mass transfer resistance governing the corrosion rate is due to the combined resistances of ceramic coating & interfacial corrosion products. Two porosity models (simple cylinder & cylinder-sphere chain) are considered in estimation of the mass transfer resistance of the ceramic coating. It is evident that a substantial impedance to O_2 transport is encountered if pores are filled with liquid water. It may be possible to use sealants to eliminate porosity. Spallation (rupture) of the ceramic coating is assumed to occur if the strain introduced by corrosion products at the ceramic-CAM interface exceeds fracture strain of the coating [11].

During the initial period of dry oxidation, any porosity in the ceramic coating is assumed to be filled with gas. If the porosity is interconnected, the impedance to O_2 transport and oxidation is believed to be relatively insignificant. In such a case, a good approximation is to simply apply the dry oxidation rate provided by Henshall [15]. The impact of dry oxidation underneath the porous ceramic is believed to be relatively insignificant, based upon preliminary calculations.

During the period of humid air corrosion (HAC), pores may be filled with either gas or liquid. If porosity is interconnected and gas-filled, the ceramic coating may not significantly impede the rate of HAC. However, the Kelvin effect can lead to condensation in very small pores. For example, at 100°C and 99% RH, 0.07 μm radius pores would be expected to be liquid filled [16]. In such a case, the impedance to O_2 transport and corrosion should be similar to that for aqueous phase corrosion (APC).

During the APC regime ($\text{RH} \geq 80\%$ & dripping conditions), pores are expected to be completely filled with water. It is assumed that typical aqueous phase corrosion rates apply at the ceramic-CAM interface [11]. Development of an appropriate model begins with consideration of the flux of oxygen, N_A , through multiple diffusion barriers, represented by subscripts P and Q (phases P and Q).

$$N_A = k_P(a_{PB} - a_{Pi}) = k_Q(a_{Qi} - a_{QB}) = K_A(a_{PB} - a_{QB}) \quad (3)$$

The overall mass transfer coefficient (mass transfer resistance) can be expressed in terms of the individual mass transfer coefficients for phases P and Q [17].

$$\frac{1}{K_A} = \frac{1}{k_P} + \frac{1}{k_Q} \quad (4)$$

Pores are treated as long cylinders of length δ .

$$N_A = \frac{D_A}{\delta} (a_{PB} - a_{Pi}) \quad (5a)$$

The average flux of oxygen per unit area of waste package is then:

$$\overline{N_A} = \frac{\theta}{\delta} D_A (a_{PB} - a_{Pi}) \quad (5b)$$

where θ is the fraction of the CAM exposed to the aqueous phase at the ceramic-CAM interface. This can be interpreted as porosity. Values of 0.02-0.03 have been routinely achieved with HVOF. The overall mass transfer coefficient is then:

$$\frac{1}{K} = \frac{1}{k_0} + \frac{1}{k_I} = \frac{1}{k_0} + \frac{\delta}{\theta D_A} \quad (6a)$$

$$K = \frac{1}{\frac{1}{k_0} + \frac{\delta}{\theta D_A}} \quad (6b)$$

The factor used to correct the oxygen-limited corrosion rate for the presence of a porous ceramic barrier is then:

$$g = \frac{\overline{N_A}}{N_{A,0}} = \frac{\frac{1}{k_0}}{\frac{1}{k_0} + \frac{\delta}{\theta D_A}} = \frac{1}{1 + \frac{k_0 \delta}{\theta D_A}} \quad (7a)$$

Note that this correction factor assumes simple cylindrical pores, which may be unrealistic. It is believed that the pores in ceramic coatings can be better represented by an array of chains, each link being composed of a hollow sphere and a relatively narrow hollow cylinder connected in series. In such a case, the analysis of porosity described by Hopper should be used [18]. Specifically, the mass transfer coefficient for the ceramic coating, k_I , should be reduced by a factor $f(\epsilon, \lambda)$:

$$k_{I,corrected} = f(\epsilon, \lambda) \times k_I \quad (9a)$$

where $f(\epsilon, \lambda)$ is defined as:

$$f(\varepsilon, \lambda) = \frac{3}{2} \frac{(1 + \lambda)^2}{\lambda} \varepsilon^2 \quad (9b)$$

Here the dimensionless parameters ε and λ represent the geometry of the sphere-cylinder chain:

$$\varepsilon = \frac{\text{diameter of cylinder in chain}}{\text{diameter of sphere in chain}} \quad (9c)$$

$$\lambda = \frac{\text{length of cylinder in chain}}{\text{diameter of sphere in chain}} \quad (9d)$$

Hopper has concluded that reasonable estimates for ε range from 0.01 to 0.05, depending upon the actual microstructure. Similarly, he has concluded that reasonable estimates of λ range from 5 to 10. Therefore, the $f(\varepsilon, \lambda)$ is estimated to be somewhere between 0.016 and 0.045. As an average for now, we estimate $f(\varepsilon, \lambda)$ to be approximately 0.03, which is mid range. Given this model for the interconnected porosity in a ceramic coating, the modified factor used to correct the oxygen-limited corrosion rate for the presence of a porous ceramic barrier is then:

$$g_{corrected} = \frac{1}{1 + \left(\frac{k_0 \delta}{\theta D_A} \right) \left(\frac{1}{f(\varepsilon, \lambda)} \right)} \quad (9e)$$

The following stoichiometry is assumed to exist between iron and oxygen:



The relationship between the oxygen flux in a single pore, N_A , and the corrosion rate, dp/dt , can be written as:

$$3N_{A,0} = 3k_0 (C_{oxygen}) = 4 \frac{\rho}{w} \frac{dp}{dt} \quad (11a)$$

where the atomic weight (w) is $55.847 \text{ g mol}^{-1}$ and the density of iron (ρ) is 7.86 g cm^{-3} . A very conservative value of the aqueous phase corrosion rate is assumed as a basis for calculating the apparent mass transfer coefficient representing corrosion in the absence of a porous ceramic barrier.

$$\frac{dp}{dt} \approx 300 \mu\text{m y}^{-1} = 9.513 \times 10^{-10} \text{ cm s}^{-1} \quad (11b)$$

This corrosion rate is a conservative estimate based on 6-month data from the LTCTF, which is illustrated in Figure 3 [12]. The concentration of oxygen dissolved in water (equilibrium with ambient air) at the air-ceramic interface is:

$$C_{\text{oxygen}} = 2.56 \times 10^{-7} \text{ mol cm}^{-3} \quad (11c)$$

This solubility value was provided by Andresen and can be found in Farmer's input to the Expert Elicitation Panel [9]. The solubility of oxygen is diminished by the addition of salt.

The flux of oxygen associated with this mass transfer coefficient is:

$$N_{A,0} = \left(\frac{4}{3}\right) \frac{7.86 \times 9.513 \times 10^{-10}}{55.847} \text{ mol cm}^{-2} \text{ s}^{-1} = 1.790 \times 10^{-10} \text{ mol cm}^{-2} \text{ s}^{-1} \quad (11d)$$

The mass transfer coefficient in the absence of a ceramic barrier is then estimated as:

$$k_0 = \frac{1}{C_{\text{oxygen}}} \left(\frac{4}{3}\right) \frac{\rho}{w} \frac{dp}{dt} \quad (11e)$$

$$k_0 = \frac{1.785 \times 10^{-10} \text{ mol cm}^{-2} \text{ s}^{-1}}{2.56 \times 10^{-7} \text{ mol cm}^{-3}} = 6.973 \times 10^{-4} \text{ cm s}^{-1} \quad (11f)$$

The factor needed for correction of the corrosion rate for the presence of a porous ceramic coating is then:

$$g_{\text{corrected}} = \frac{[0.02 \times 0.03 \times 10^{-5} \text{ cm}^2 \text{ s}^{-1}]}{[0.02 \times 0.03 \times 10^{-5} \text{ cm}^2 \text{ s}^{-1}] + [0.15 \text{ cm} \times 6.973 \times 10^{-4} \text{ cm s}^{-1}]} = 5.736 \times 10^{-5} \quad (12a)$$

Therefore, the porous ceramic coating would lower the aqueous phase corrosion rate from approximately $300 \mu\text{m y}^{-1}$ to only $1.721 \times 10^{-2} \mu\text{m y}^{-1}$.

$$\frac{dp}{dt} = g_{\text{corrected}} \left(\frac{dp}{dt}\right)_0 = 1.721 \times 10^{-2} \mu\text{m y}^{-1} \quad (12b)$$

An estimate of the time to fracture due to the formation of corrosion products at the ceramic-CAM interface can be estimated, provided that the mechanical properties of the ceramic are known. Estimated properties for the ceramic coating are taken from a text on engineering materials and are summarized in Table 8 [19]. The range of fracture toughness values given for typical ceramics is given as:

$$K_{IC} = 3.3 \text{ to } 5.8 \text{ MPa}\sqrt{\text{m}} = 3.0 \text{ to } 5.3 \text{ ksi}\sqrt{\text{in}} \quad (13)$$

While these properties serve as a good starting place for TSPA-VA, handbook values for mechanical properties of ceramics will probably need to be revised to better reflect those of actual coatings. Direct measurement of the elastic modulus is required.

The rate of expansion of the inner radius of the ceramic barrier coating is estimated from the penetration rate, accounting for the expansion at the interface due to the density difference between Fe_2O_3 and Fe:

$$\frac{dR}{dt} = 2 \frac{dp}{dt} = 2 \times 1.721 \times 10^{-2} \mu\text{m y}^{-1} = 3.442 \times 10^{-8} \text{ m y}^{-1} \quad (14a)$$

If the inner radius of the ceramic coating (outer radius of the CAM) is assumed to be approximately 1 meter ($R \approx 1 \text{ m}$), the strain rate in the coating can be estimated with Equation 14b:

$$\frac{de}{dt} = \frac{1}{2\pi R} 2\pi \frac{dR}{dt} = 3.442 \times 10^{-8} \text{ y}^{-1} \quad (14b)$$

The stress and strain are related through the elastic modulus:

$$\sigma = E \times e \quad (14c)$$

The fracture strain can then be estimated from the elastic modulus and the fracture stress.

$$e^* = \frac{\sigma^*}{E} = \frac{172 \text{ MPa}}{356,000 \text{ MPa}} = 4.831 \times 10^{-4} \quad (14d)$$

The time required for the strain to reach the fracture strain determines the time to fracture. This is the time required for formation of the first crack in the ceramic coating, but does not necessarily imply failure of the coating.

$$\tau^* = \frac{e^*}{de/dt} = \frac{4.831 \times 10^{-4}}{3.442 \times 10^{-8} \text{ y}^{-1}} = 14,037 \text{ y} \quad (15)$$

The critical flaw size for crack initiation in the ceramic coating is estimated with Equation 16a:

$$a^* \approx \left(\frac{K_{IC}}{\sigma^*} \right)^2 \frac{1}{\pi} = \left(\frac{3.3 \text{ MPa } \sqrt{\text{m}}}{172 \text{ MPa}} \right)^2 \frac{1}{\pi} = 1.172 \times 10^{-4} \text{ m} = 117.2 \mu\text{m} \quad (16a)$$

where the fracture toughness is defined by Equation 16b:

$$K_{IC} = \sigma \sqrt{\pi a} f(a, W) \quad (16b)$$

In addition to the contiguous coating assumed in the previous paragraphs, a variation of the model has been developed for TSPA-VA. This variation assumes that the ceramic coating spalls due to the formation of blisters as shown in Figure 4. Each blister is assumed to have a radius that is equivalent to the patch size assumed in the WAPDEG TSPA code. The volume of corrosion product (Fe_2O_3) in the blister is defined as:

$$V_{\text{blister}} = \frac{4}{3} \pi a^2 b \quad (17)$$

where a and b define the dimensions of the oblate spheroid. After significant growth of the blister, the surface area of the blister is:

$$A_{\text{blister}} = \frac{1}{2} \left[2\pi a^2 + \frac{\pi b^2}{\gamma} \ln \left(\frac{1+\gamma}{1-\gamma} \right) \right] \quad t > 0 \quad (18a)$$

where the parameter γ is defined as:

$$\gamma = \frac{\sqrt{a^2 - b^2}}{a} \quad (18b)$$

In contrast, the area of the blister is essentially that of a flat disk at time zero.

$$A_{\text{blister}} = \pi a^2 \quad t = 0 \quad (18c)$$

The strain in the ceramic coating covering the blister is then defined in terms of the exposed area of the blister after interfacial corrosion ($t > 0$) relative to the initial area ($t = 0$):

$$e = \frac{A_{\text{blister}}(t > 0)}{A_{\text{blister}}(t = 0)} - 1 \quad (19a)$$

The strain can be rewritten in terms of the blister dimensions, as shown in Equation 19b:

$$e = \left(\frac{b}{a} \right)^2 \left(\frac{1}{2\gamma} \right) \ln \left(\frac{1+\gamma}{1-\gamma} \right) \quad (19b)$$

The criterion for fracture (spallation) of the blister is then:

$$e > e^* \approx 4.831 \times 10^{-4} \quad (19c)$$

where e^* is the fracture strain of the ceramic. The relationship between the volume of corrosion product (blister) and the volume of oxidized iron is:

$$V_{\text{blister}} = 3.6055 \times V_{\text{iron}} \quad (20a)$$

This equation can be used to express the height of the blister in terms of the volume of oxidized CAM, which is assumed to be essentially iron.

$$b = \frac{3}{4} \left(\frac{3.6055 \times V_{\text{iron}}}{\pi a^2} \right) \quad (20b)$$

The volume of oxidized CAM is time dependent, and calculated from the corrosion rate at the ceramic-CAM interface during three successive phases of corrosion; dry oxidation, humid air corrosion; and aqueous phase corrosion. Note that this is an approximation, assuming growth of a cylindrical volume of oxide beneath a flat circular disk. The flux of oxygen driving the formation of corrosion product is assumed to be through the circular shaped disk of oxide.

$$V_{\text{iron}} \approx \pi a^2 \left[\int_0^{\tau_{\text{DRY}}} g_{\text{DRY}} \left(\frac{dp}{dt} \right)_{\text{DRY}} dt + \int_{\tau_{\text{DRY}}}^{\tau_{\text{HAC}}} g_{\text{HAC}} \left(\frac{dp}{dt} \right)_{\text{HAC}} dt + \int_{\tau_{\text{HAC}}}^{\tau_{\text{APC}}} g_{\text{APC}} \left(\frac{dp}{dt} \right)_{\text{APC}} dt \right] \quad (20c)$$

Given these assumptions and the above equation, the time-dependent height of the blister can be calculated with:

$$b \approx 2.7041 \left[\int_0^{\tau_{\text{DRY}}} g_{\text{DRY}} \left(\frac{dp}{dt} \right)_{\text{DRY}} dt + \int_{\tau_{\text{DRY}}}^{\tau_{\text{HAC}}} g_{\text{HAC}} \left(\frac{dp}{dt} \right)_{\text{HAC}} dt + \int_{\tau_{\text{HAC}}}^{\tau_{\text{APC}}} g_{\text{APC}} \left(\frac{dp}{dt} \right)_{\text{APC}} dt \right] \quad (20d)$$

This alternative model for impedance and spallation has been used to provide what appears to be reasonable estimates.

From preliminary calculations based upon Equations 3 through 16, it is believed that the existence of a slightly porous ceramic coating on the surface could significantly lengthen the life of the container, adding an estimated 14,037 years to the life of the waste package (Table 9). It should be possible to further increase life by taking steps to close interconnected porosity in the coating. For example, Zn or Al could be deposited on the outer surface of the ceramic, as well as inside near-surface pores. These deposits would oxidize in air, thereby sealing porosity with the corresponding metal oxides. Both Zn and Al are attractive candidates for sealing porosity since unoxidized metal would be sacrificial to the A516 Gr 55 in galvanic couples. Other possible sealants have also been identified. The modified g-factor presented here can be used as a practical means to adjust CAM corrosion rates to account for the ceramic coating.

Work is in progress at LLNL to verify the corrected g-factor through application of ac impedance spectroscopy. A PAR Model 273 with either a PAR Model 5610 dual-channel lock-in amplifier is now being used to determine the complex impedance of the electrolyte-filled ceramic barrier over the frequency range extending from 0.001 to 100,000 Hz. Preliminary data indicates that a ceramic coating with 1 to 2% porosity can increase the interfacial electrical impedance by approximately eight orders-of-magnitude (10^8). With a well planned experiment and proper interpretation of the data, insight into transport in the pores should be possible. It should also be possible to develop some understanding of the layer of corrosion products at the

base of the pores. Note that dc measurements have also been done. In the future, it would also be beneficial to include terms for the attenuation of corrosion rate due to mass transport (solid state) through the iron oxide in the pores.

Passive Corrosion of the Inner Barrier (CRM)

The modes of corrosion that are believed to be relevant to the ultimate failure of the CRM include: (a) passive corrosion; (b) crevice corrosion; (c) pitting; and (d) stress corrosion cracking. Passive corrosion of the CRM is expected to occur on surfaces where the CAM has exfoliated, as well as on surfaces that lie inside the CAM-CRM crevice, provided that environmental conditions (pH, chloride, potential, and temperature) are below the thresholds for localized attack. A correlation of Alloy C-22 passive corrosion rates with temperature, pH, equivalent NaCl concentration, and FeCl₃ concentration has been developed [12]. The rates used as a basis of this correlation are from the LTCTF, Roy's electrochemical measurements [20-23], and Haynes International [6,7]. These data are summarized in Tables 10 and 11, and illustrated by Figures 5a and 5b. The following linear equation was found to be adequate for the correlation:

$$\ln\left(\frac{\Delta p}{\Delta t}\right) = b_0 + b_1\left(\frac{1000}{T + 273}\right) + b_2(pH) + b_3(C_{NaCl}) + b_4(C_{FeCl_3}) \quad (21a)$$

where $\Delta p/\Delta t$ is the apparent penetration rate ($\mu\text{m yr}^{-1}$); T is the temperature ($^{\circ}\text{C}$); C_{NaCl} is the equivalent concentration of NaCl (wt. %); and C_{FeCl_3} is the concentration of FeCl₃ (wt. %). Within the bounds of thirty-eight (38) experimental observations for Alloy C-22, the coefficients were determined to be:

$$\begin{aligned} b_0 &= +13.409 \\ b_1 &= -5.5587 \\ b_2 &= -0.87409 \\ b_3 &= +0.56965 \\ b_4 &= +0.60801 \end{aligned} \quad (21b-f)$$

More specifically, the correlation for Alloy C-22 is:

$$\ln\left(\frac{\Delta p}{\Delta t}\right) = 13.409 - \left(\frac{5558.7}{T + 273}\right) - 0.87409(pH) + 0.56965(C_{NaCl}) + 0.60801(C_{FeCl_3}) \quad (21g)$$

Based upon this correlation, it is concluded that the apparent activation energy is approximately 12 kcal mol⁻¹, which is quite reasonable. The "standard error of estimate" ($s_{y/1234}$) and the "sample multiple variable regression coefficient" ($r_{y/1234}$) are defined by Crow, Davis and Maxfield [24]. The "standard error of estimate" is a measure of the scatter of the observed penetration rates about the regression plane. About 95% of the points in a large sample are expected to lie within $\pm 2s_{y/1234}$ of the plane, measured in the y direction. Values for the above correlation are:

$$\begin{aligned} s_{y/1234} &= 1.5092 \\ r_{y/1234} &= 0.65628 \end{aligned} \quad (22a-b)$$

The “multiple variable regression coefficient” indicates a reasonably good fit to the data set, given the large number of independent variables. As discussed in the literature, uncertainty in a given model parameter, β_j , can be determined from the standard error of estimate, as shown by Equations 23a and 23b [24]:

$$s_{b_j} = s_{y/123\dots k} \sqrt{n e_{jj}} \quad (23a)$$

$$\beta_j = b_j \pm (t_{a/2, n-k-1}) \times s_{b_j} \quad (23b)$$

This simple correlation has been tested within the bounds of anticipated conditions. The predictions appear to be reasonable for combinations of input parameters representative of the: Near Field Environment (NFE); Simulated Dilute Water (SDW), Simulated Concentrated Water (SCW), and Simulated Acidified Water (SAW) waters; Simulated Cement-Modified Water (SCMW); the unusually harsh, simulated crevice corrosion test of Haynes International (10 wt. % FeCl_3) [6,7]; and the conditions predicted during preliminary tests of the LLNL crevice transport model [13,14]. The worst case within the bounds of the regression analysis is the simulated crevice condition used by Haynes International (10 wt. % FeCl_3). In the repository, the concentration of FeCl_3 is expected to be limited to much lower values by the presence of carbonate, which precipitates iron. *It must be noted that combinations of input parameters that are clearly beyond the range of the data included in the correlation cannot be used to generate reasonable predictions. Therefore, this correlation should not be used for saturated solutions of J-13 and/or FeCl_3 . Within the limits of the experimental data, predictions are believed to be good representations of the observations.*

The estimation of passive corrosion rates from Roy's cyclic polarization measurements is now explained [12, 20-23]. It is well known that the corrosion (or penetration) rate of an alloy, dp/dt , can be calculated from the corrosion current density, i_{corr} , as follows:

$$\frac{dp}{dt} = \frac{i_{\text{corr}}}{\rho_{\text{alloy}} n_{\text{alloy}} F} \quad (24a)$$

where ρ_{alloy} is the density of the alloy, assumed to be approximately 8.4 g cm^{-3} , and F is Faraday's constant. The number of gram equivalents per gram of alloy, n_{alloy} , is calculated with the following equation:

$$n_{\text{alloy}} = \sum_j \left(\frac{f_j n_j}{a_j} \right) \quad (24b)$$

where f_j is the mass fraction of the j -th alloying element in the material, n_j are the number of electrons involved in the anodic dissolution process, which is assumed to be congruent, and a_j is the atomic weight of the j -th alloying element. These equations have been used to calculate penetration rates for Alloy C-22 from apparent corrosion currents determined during cyclic polarization measurements. In principle, such electrochemically-determined rates should be consistent with those observed in the LTCTF, though experience indicates that such electrochemically-determined rates are conservative (higher than those actually observed).

TSPA codes require that corrosion rates be represented by appropriate cumulative probability distribution functions (CDF's). In the case of passive corrosion of Alloy C-22 in 1000X J-13, CDF's can be based upon the above correlation, since the chloride concentration is within the range of data included in the correlation [12]. In the case of saturated J-13, estimates can be based upon the article by Smailos, Schwarzkopf, and Koster [25], as interpreted by Shoesmith [26]. The data quoted by Shoesmith is for "Q-Brine" and "Z-Brine" electrolytes, as shown Table 12.

Construction of CDF's for Alloy C-22 passive corrosion rates in 1000X and saturated J-13 waters requires estimation of the means, as well as the width of the distributions at those means. It is assumed that *logarithmic rates are normally distributed*. To establish a CDF for 1000X J-13, the correlation (Equation 21g) is first used to estimate the logarithmic rate (Equation 25a) at the 50th percentile:

$$y = \ln \left[\frac{\Delta p}{\Delta t} \right] \quad (25a)$$

Equations 25b through 25g are then used to estimate the logarithmic rates at the 5th, 95th, 1st, and 99th percentiles:

$$y_{5\%} \approx y_{predicted} - \delta y_{\alpha=0.05} \approx y_{predicted} - t_{\alpha=0.05} s_{y/123...k} \quad (25b)$$

$$y_{95\%} \approx y_{predicted} + \delta y_{\alpha=0.05} \approx y_{predicted} + t_{\alpha=0.05} s_{y/123...k} \quad (25c)$$

$$t_{\alpha=0.05} \approx 1.70 \quad (25d)$$

$$y_{1\%} \approx y_{predicted} - \delta y_{\alpha=0.01} \approx y_{predicted} - t_{\alpha=0.01} s_{y/123...k} \quad (25e)$$

$$y_{99\%} \approx y_{predicted} + \delta y_{\alpha=0.01} \approx y_{predicted} + t_{\alpha=0.01} s_{y/123...k} \quad (25f)$$

$$t_{\alpha=0.01} \approx 2.46 \quad (25g)$$

Equations 25h through 25k are used to construct CDF's in terms of actual rates.

$$r_{5\%} = \left[\frac{\Delta p}{\Delta t} \right]_{5\%} \approx \exp[y_{\text{predicted}} - 1.70 \times s_{y/123\dots k}] \quad (25h)$$

$$r_{95\%} = \left[\frac{\Delta p}{\Delta t} \right]_{95\%} \approx \exp[y_{\text{predicted}} + 1.70 \times s_{y/123\dots k}] \quad (25i)$$

$$r_{1\%} = \left[\frac{\Delta p}{\Delta t} \right]_{1\%} \approx \exp[y_{\text{predicted}} - 2.46 \times s_{y/123\dots k}] \quad (25j)$$

$$r_{99\%} = \left[\frac{\Delta p}{\Delta t} \right]_{99\%} \approx \exp[y_{\text{predicted}} + 2.46 \times s_{y/123\dots k}] \quad (25k)$$

Since no data for brines have been generated in the LTCTF, the CDF's for saturated J-13 are based upon the measurements of Smailos et al., which are summarized in Table 12 [25]. The rate of $0.02 \mu\text{m y}^{-1}$ for Alloy C-4 in Q-Brine at 90°C (pH ~ 5) is interpreted as a "typical" value (taken here as the rate at the 50th percentile). The rate of $10\text{-}14 \mu\text{m y}^{-1}$ for Alloy C-4 in Z-Brine at 90°C (pH ~ 2) is interpreted as the "maximum possible" value by Shoesmith (taken here as the rate at 99th percentile). According Smailos et al., "After three years of exposure until now Hastelloy C-4 has remained resistant to pitting corrosion, and to stress corrosion cracking. At 90°C local crevice corrosion attacks occurred at single points at the metal/PTFE and metal/metal contact surfaces, with maximum depths of $250 \mu\text{m}$ (metal/PTFE) and $20\text{-}70 \mu\text{m}$ (metal/metal), respectively." This translates into a maximum rate of $15\text{-}51 \mu\text{m y}^{-1}$. It must be noted that the rates from the Smailos et al. had to be scaled for pH and temperature so that all conditions of interest in this elicitation could be covered. While the base rate used was taken from the "Z-Brine" data, the activation energy used to scale the rate for temperature had to be inferred from the "Q-Brine" data. A reasonable value of the activation energy, E_a , was determined to be approximately 12 kcal mol^{-1} from the correlation (Equation 21g). The estimate was made with the following equation, which is based upon an Ahrenius-type rate expression:

$$\frac{r_1}{r_2} = \exp \left[\frac{E_a}{R} \left(\frac{1}{T_2} - \frac{1}{T_1} \right) \right] \quad (26a)$$

At 170°C (T_1), the observed penetration rates were given as 0.66 and $0.15 \mu\text{m y}^{-1}$, which were averaged to give a single value of $0.4 \mu\text{m y}^{-1}$ (r_1). At a lower temperature of 90°C (T_2), the observed rate was given as $0.02 \mu\text{m y}^{-1}$ (r_2). Rates were scaled with the pH as implied by the correlation (Equation 21g), since no better means of estimating the response is available. Therefore, the rates were assumed to obey the following empirical law:

$$\frac{r_1}{r_2} = \exp[0.87409(pH_2 - pH_1)] \quad (26b)$$

In this case, the standard deviation was estimated to be about 1.6228, the value of $u_{\alpha=0.05}$ was assumed to be 1.645 and the value of $u_{\alpha=0.01}$ was assumed to be 2.326 [9]. These CDF constructions are given in Table 13.

Data Published by Haynes International

Data published by Haynes International [6,7] and compiled by Gdowski [27] have also been used as the basis of the following correlations for Alloys 825, 625, C-4, C-22 and C-276, respectively:

$$\text{Alloy 825: } \ln(\Psi) = \ln(2.1164 \times 10^1) - 5.9141 \times 10^{-6}(T - T_0)^2 - 1.1235 \times 10^{-3}(T - T_0) \quad (27a)$$

$$\text{Alloy 625: } \ln(\Psi) = \ln(4.3493 \times 10^{-2}) - 2.4010 \times 10^{-3}(T - T_0)^2 + 2.3662 \times 10^{-1}(T - T_0) \quad (27b)$$

$$\text{Alloy C-4: } \ln(\Psi) = \ln(8.6758 \times 10^{-3}) + 2.5403 \times 10^{-3}(T - T_0)^2 - 4.2970 \times 10^{-2}(T - T_0) \quad (27c)$$

$$\text{Alloy C-22: } \ln(\Psi) = \ln(2.8539 \times 10^{-3}) + 1.2375 \times 10^{-3}(T - T_0)^2 - 2.9369 \times 10^{-2}(T - T_0) \quad (27d)$$

$$\text{Alloy C-276: } \ln(\Psi) = \ln(5.8219 \times 10^{-3}) + 1.5234 \times 10^{-3}(T - T_0)^2 - 3.7309 \times 10^{-2}(T - T_0) \quad (27e)$$

where T is the absolute temperature of the CRM and T_0 is the reference temperature of 298 K. The parameter Ψ is defined as follows:

$$\Psi = \frac{d}{\sqrt{t}} \quad (27f)$$

where d is the penetration in microns (μm) and t is the time in hours (h). Figure 6a shows actual data published by Haynes International, while Figure 6b is a graphical representation of the above correlations (Equations 27a through 27f). Figure 7a shows penetrations of the candidate CRMs in a simulated crevice solution with 10 wt. % FeCl_3 at 80°C , predicted with the correlations. Predicted penetrations for Alloy C-22 at several temperature levels between 20 and 100°C are shown in Figure 7b. Such empirical models can be used as a basis of materials selection, but may not be adequate for predictions over extremely long periods of time.

CREVICE CORROSION MODEL

Introduction to Crevice Corrosion

Crevices will be formed between waste package and supports; beneath mineral precipitates, corrosion products, dust, rocks, cement and biofilms; and between CAM and CRM. It is well known that the crevice environment will be more severe than the NFE. The hydrolysis of dissolved metal will lead to the accumulation of H^+ and the corresponding suppression of pH. As previously discussed, Jones and Wilde have prepared solutions of FeCl_2 , NiCl_2 and CrCl_3 to simulate such localized environments and measured substantial pH suppression [1]. Wang has made similar measurements with FeCl_3 solutions, which are reported here. As pointed out by

McCoy, the measured pH in active, artificial crevices is: 3.3 to 4.7 if the crevice is formed with carbon steel; 2.4 to 4.0 if the crevice is formed with a Fe-Cr alloy, and ≤ 2.3 if the crevice is formed with a stainless steel [2,3]. These data and measurements are summarized in Tables 14 through 16. Field-driven electromigration of Cl^- (and other anions) into crevice must occur to balance cationic charge associated with H^+ ions. The exacerbated conditions inside the crevice set the stage for subsequent attack of the CRM can be by passive corrosion, pitting (initiation & propagation), stress corrosion cracking (initiation & propagation), or other mechanisms. Clearly, the development of an adequate crevice corrosion model for determination of the exact nature of the local environment is prudent.

A detailed deterministic model has been developed to calculate the spatial distributions of electrochemical potential and current density in the CAM-CRM crevice, as well as transient concentration profiles of dissolved metals and ions [13,14]. The local concentration of hydrogen cation is assumed to be limited by either (a) anion transport into the crevice or (b) hydrogen ion production and transport out of the crevice. If the limitation is assumed to be due to anion transport, all hydrolysis reactions at each point inside the crevice are assumed to instantaneously reach equilibrium. Furthermore, it is assumed that electroneutrality is maintained at each point. In contrast, if the limitation is assumed to be hydrogen ion production and transport, the local generation rate of hydrogen ion must be known and is assumed to be proportional to the dissolution rates of dissolved metals, with proportionality constants being calculable from hydrolysis equilibrium constants. Note that rate constants for the hydrolysis reactions are unknown, with experimental determination being impractical. In this case, anion concentrations are calculated at each point based upon electroneutrality. This model can be used to estimate the extent of pH suppression in the CAM-CRM crevice due to the simultaneous hydrolysis and transport of dissolved Fe, Ni, Cr, Mo and W. It is assumed that crevice corrosion passes through two phases. Dissolution of the CAM at a relatively low electrochemical potential is assumed to occur during Phase 1. After anodic oxidation (consumption) of the accessible CAM, the electrochemical potential of the CRM will increase to high levels. Dissolution of the CRM is assumed to predominate during Phase 2. Lower pH values can be reached during Phase 2 crevice corrosion than during Phase 1 crevice corrosion, due primarily to the hydrolysis of dissolved chromium. In the case of crevice corrosion of Alloy 625, the predicted pH inside the crevice was 2.8 to 3.2, with a corresponding increase in chloride concentration. This calculation assumed a temperature of 25°C, an electrochemical potential at the crevice mouth that is 100 mV above the critical pitting potential, and a uniform crevice width (CAM-CRM separation) of 0.075 mm. Tighter crevices should lead to lower pH and higher chloride. It is also predicted that the electrochemical potential (E) will decrease with increasing depth. Therefore, the potential should never be more severe (closer to the threshold for LC) than at the crevice mouth.

Fluxes of ions in the crevice are calculated with the Nernst-Planck equation, which governs electromigration, diffusion, and convective transport [28]. The current density is then defined in terms of these fluxes. In cases with strong supporting electrolyte, the electromigration term can be ignored. Transient concentrations can be determined from the gradient of the flux. The concentration of dissolved iron is assumed to include Fe^{2+} , Fe^{3+} , $\text{Fe}(\text{OH})^+$ and $\text{Fe}(\text{OH})^{2+}$. Similar assumptions are made for other dissolved metals. The partial differential equations (PDE's) that describe the transport of such reactive species in the crevice can be solved numerically. Both the Crank-Nicholson and the 'explicit' methods have been used [29,30]. The assumed boundary

conditions (BC's) imply that the concentrations of dissolved metals are zero at the crevice mouth (NFE), and that crevices are symmetric about a mirror plane where the flux is zero. The BC's for H^+ and dissolved O_2 are slightly different in that non-zero concentrations are assigned at the crevice mouth. The PDE's that define transient concentrations in the crevice require determination of the potential gradient, as well as the (apparent) homogeneous rates. First, the axial current density along the length of the crevice is calculated by integrating the wall current density. The electrode potential along the length of the crevice can then be calculated from the axial current density. This technique is similar to that employed in other models [31-33].

Crevice Chemistry

Dissolution of the CAM wall will produce iron ions, whereas dissolution of the CRM wall will produce iron, nickel, chromium, molybdenum and tungsten ions. As discussed by Oldfield and Sutton, metal ions produced by anodic dissolution are assumed to undergo the following hydrolysis reactions [34]:



Relevant equilibrium constants are defined as follows [34]:

$$K_{3,1} = \frac{[Fe(OH)^+][H^+]}{[Fe^{2+}]} \quad (29a)$$

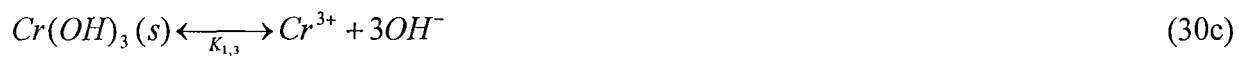
$$K_{4,1} = \frac{[Fe(OH)^{2+}][H^+]}{[Fe^{3+}]} \quad (29b)$$

$$K_{5,1} = \frac{[Ni(OH)^+][H^+]}{[Ni^{2+}]} \quad (29c)$$

$$K_{1,1} = \frac{[Cr(OH)^{2+}][H^+]}{[Cr^{3+}]} \quad (29d)$$

$$K_{1,2} = \frac{[Cr(OH)_2^+][H^+]}{[Cr(OH)^{2+}]} \quad (29e)$$

If the dissolved metals exceed the solubility limits, precipitation will occur:



The corresponding solubility products are:

$$K_{3,3} = [Fe^{2+}][OH^-]^2 \quad (31a)$$

$$K_{5,3} = [Ni^{2+}][OH^-]^2 \quad (31b)$$

$$K_{1,3} = [Cr^{3+}][OH^-]^3 \quad (31c)$$

The effects of hexavalent chromium, molybdenum and tungsten hydrolysis on pH have been ignored in this preliminary version of the model, but will be accounted for in the future. In the case of stainless steel, $Fe(OH)_2$, $Ni(OH)_2$ and $Cr(OH)_3$ precipitates are formed if solubility limits are exceeded. In the case of materials such as Alloy C-22, oxide and hydroxide precipitates of tungsten and molybdenum may also form. The hydrolysis equilibrium constants were found in the literature and are summarized in Table 17 [34-36]. Better equilibrium data from the EQ3/6 code will be used in the future, as has recently been done by others [37]. The EQ3/6 code was also developed by LLNL.

Option 1 - Limitation Due to Anion Transport

In this case, it is assumed that acidification of the crevice solution is limited by the transport of Cl^- into the crevice, instead of being limited by H^+ production and transport out of the crevice. As discussed by Xu and Pickering [32], Cl^- will be driven into the crevice by the potential gradient. The corresponding concentration in the crevice is:

$$[Cl^-] = [Cl^-]_0 \exp\left[-\frac{F}{RT}\Phi(x)\right] \quad (32)$$

where $[Cl^-]_0$ is the concentration at the crevice mouth, F is Faraday's constant, $\Phi(x)$ is the potential in the crevice relative to that at the mouth, and (x) is the distance from the crevice

mouth. After the Cl^- concentration is established, the H^+ concentration can be determined with the equation for electroneutrality. The general expression is:

$$\sum_{j=1}^{m_a} n_j^- z_j^- = \sum_{j=1}^{m_c} n_j^+ z_j^+ \quad (33a)$$

where n_j^- is the molar concentration of the j-th anion, z_j^- is the charge of that anion, m_a is the total number of anionic species, n_j^+ is the molar concentration of the j-th cation, z_j^+ is the charge of that cation, and m_c is the total number of cationic species. This can be written more specifically in terms of anticipated species:

$$\begin{aligned} & [OH^-] + [Cl^-] + [F^-] + [NO_3^-] + [HCO_3^-] + 2[CO_3^{2-}] + 2[SO_4^{2-}] + 2[S^{2-}] + 2[Cr_2O_7^{2-}] = \\ & [H^+] + [Na^+] + [K^+] + 2[Mg^{2+}] + 2[Ca^{2+}] + 2[Mn^{2+}] + 2[Ni^{2+}] + [Ni(OH)^+] + \\ & 2[Fe^{2+}] + [Fe(OH)^+] + 3[Fe^{3+}] + 2[Fe(OH)^{2+}] + [Fe(OH)_2^+] + \\ & 3[Cr^{3+}] + 2[Cr(OH)^{2+}] + [Cr(OH)_2^+] \end{aligned} \quad (33b)$$

Here too the concentrations of dissolved species are expressed in terms of the hydrogen ion concentration, equilibrium constants for the hydrolysis reactions, solubilities of corrosion products, and the dissociation constant for water. The resulting equation is a polynomial in $[H^+]$ whose roots can be used to determine the pH [13,14].

Option 2 - Limitation Based Upon Transport of Hydrogen Ion

An alternative strategy assumes that the accumulation of H^+ ions (pH suppression) in the crevice is limited by: (a) the overall production rate of H^+ due to the hydrolysis of dissolved metals; and (b) the loss rate of H^+ due to leakage from the crevice mouth. In order to quantify this effect, the net mass balance for H^+ ions must first be established:

$$[H^+] = [H^+]_{Fe(II)} + [H^+]_{Fe(III)} + [H^+]_{Ni(II)} + [H^+]_{Cr(III)} - [H^+]_{H_2} - [H^+]_{O_2} \quad (34a)$$

In the present model, the effects of hexavalent chromium, molybdenum and tungsten on pH are assumed to be insignificant. The quantity of hydrogen ions generated by the hydrolysis of divalent iron ions produced during the dissolution of either the CAM or CRM is:

$$[H^+]_{Fe(II)} = 2[Fe(OH)_2(s)] + [Fe(OH)^+] \quad (34b)$$

The dissolved Fe^{2+} can be converted to Fe^{3+} by: (I) microbial action; (ii) oxidation by naturally occurring MnO_2 or other oxidants; or (ii) anodic oxidation. Once formed, it is assumed that Fe^{3+} can also undergo hydrolysis. The quantity of hydrogen ions produced by this reaction is:

$$[H^+]_{Fe(III)} \approx [Fe(OH)^{2+}] \quad (34c)$$

Dissolution of the CRM will produce divalent nickel and trivalent chromium ions, in addition to divalent iron ions. The equations for the divalent nickel are analogous to those for the divalent iron:

$$[H^+]_{Ni(II)} = 2[Ni(OH)_2](s) + [Ni(OH)^+] \quad (34d)$$

The equations for the trivalent chromium are similar to those for the trivalent iron:

$$[H^+]_{Cr(III)} = 3[Cr(OH)_3](s) + 2[Cr(OH)_2^+] + [Cr(OH)^{2+}] \quad (34e)$$

Hydrogen ions lost due to hydrogen evolution and the cathodic reduction of oxygen to water are represented by:

$$[H^+]_{H_2} = 2[H_2] \quad (34f)$$

$$[H^+]_{O_2} = 4[O_2] \quad (34g)$$

Equations 34b through 34g are substituted into Equation 34a. The concentrations of soluble hydrolysis products are then expressed in terms of $[H^+]$ and the concentrations of unhydrolyzed metal ions. The result is then differentiated with respect to time to yield the following H^+ generation rate:

$$\frac{d[H^+]}{dt} = \frac{\left\{ \frac{K_{3,1}}{[H^+]} \frac{d[Fe^{2+}]}{dt} + \frac{K_{4,1}}{[H^+]} \frac{d[Fe^{3+}]}{dt} + \frac{K_{5,1}}{[H^+]} \frac{d[Ni^{2+}]}{dt} + \frac{K_{1,1}}{[H^+]} \frac{d[Cr^{3+}]}{dt} + \frac{2K_{1,1}K_{1,2}}{[H^+]^2} \frac{d[Cr^{3+}]}{dt} - 2 \frac{d[H_2]}{dt} - 4 \frac{d[O_2]}{dt} \right\}}{\left\{ 1 + \frac{K_{3,1}}{[H^+]^2} + \frac{K_{4,1}}{[H^+]^2} + \frac{K_{5,1}}{[H^+]^2} + \frac{K_{1,1}}{[H^+]^2} + \frac{4K_{1,1}K_{1,2}}{[H^+]^3} \right\}} \quad (34h)$$

The consumption of H^+ by hydrogen evolution and cathodic oxygen reduction is accounted for. Since the H^+ generation rate approaches zero as $[H^+]$ and the concentrations of unhydrolyzed metal ions approach infinity (large values), the extent of pH suppression in the crevice is limited. If solubility limits are exceeded, $Fe(OH)_2$, $Ni(OH)_2$ and $Cr(OH)_3$ precipitates are assumed to form. Under these conditions, the H^+ generation rate is proportional to the rates of precipitation, which are directly related to the rates of dissolution. As previously discussed, the hydrolysis equilibrium constants can be found in the literature [34-36].

Ion Transport in Crevice

Attention is now directed to the specific issue of ion transport in the crevice separating the CAM and CRM. As discussed by Newman, fluxes of ions are estimated with the Nernst-Planck equation, which governs electromigration, diffusion, and convective transport [28]:

$$\bar{N}_i = -z_i u_i F c_i \bar{\nabla} \Phi - D_i \bar{\nabla} c_i + \bar{v} c_i \quad (35)$$

where N_i is the flux, z_i is the charge, u_i is the mobility, c_i is the concentration and D_i is the diffusivity of the i -th ion; Φ is the potential in the electrolyte; and v is the convective velocity of the electrolyte. The current density ($F \sum_i \bar{N}_i$) is then defined in terms of the flux:

$$\bar{i} = -F^2 \bar{\nabla} \Phi \sum_i z_i^2 u_i c_i - F \sum_i z_i D_i \bar{\nabla} c_i \quad (36)$$

The convective transport term has not been included. In cases with strong supporting electrolyte, the electromigration term can be ignored. Transients in concentration can be dealt with through application of Equation 37:

$$\frac{\partial c_i}{\partial t} = -\bar{\nabla} \cdot \bar{N}_i + R_i \quad (37)$$

where R_i is the apparent local homogeneous rate (ALHR). The ALHR is the rate per unit volume of electrolyte. In the simple one-dimensional (1D) problem, the ALHR for each dissolved metal is assumed to be proportional to the local dissolution (corrosion) rate. The ALHR for H^+ production is also assumed to be proportional to the local dissolution rates, as illustrated by Equation 34h. Note that the concentration of dissolved iron is assumed to include all dissolved species, including Fe^{2+} , Fe^{3+} , $Fe(OH)^+$ and $Fe(OH)^{2+}$. Similar assumptions are made for other dissolved metals. The hyperbolic partial differential equations (PDE's) that describe the transport of such reactive species in the crevice can be solved numerically. Both the Crank-Nicholson and the 'explicit' methods have been used [29,30]. The assumed BC's imply that the concentrations are zero at the crevice mouth (NFE), and that crevices are symmetric about a mirror plane where the flux is zero. The BC's for H^+ and dissolved O_2 are slightly different in that non-zero concentrations are assigned at the crevice mouth.

Current and Potential

The PDE's that define transient concentrations in the crevice require determination of the potential gradient, as well as the (apparent) homogeneous rates. First, the axial current density along the length of the crevice, $i_x(x)$, is calculated by integrating the wall current density, $i_y(x)$:

$$i_x(x) = \frac{\int_x^L i_y(x) dx}{h(x)} \quad (38)$$

where L is the maximum crevice depth and $h(x)$ is the separation between the two crevice walls at position (x) . The electrode potential along the length of the crevice, $E(x)$, can then be calculated from $i_x(x)$:

$$E(x) = \int_0^x \rho(x) i_x(x) dx \quad (39)$$

where $\rho(x)$ is the resistivity of the crevice solution at position (x). This technique is very similar to that employed in other published models [31-33].

Simultaneous Numerical Solution of Transport Equations

Actual calculation of the transient concentrations is described here. First, the terms for electromigration in the Nernst-Planck equation are assumed to be insignificant, which is valid in cases involving a strong supporting electrolyte [28]. A single, lumped-sum concentration is then used to represent each dissolved metal. For example, the lumped-sum concentration of dissolved iron includes contributions of Fe^{2+} , Fe^{3+} , $\text{Fe}(\text{OH})^+$ and $\text{Fe}(\text{OH})^{2+}$. It is necessary to employ this concept of the concentration since rates of reaction (apparent homogeneous rates) for individual species are unknown. An overall generation rate for each dissolved metal can be calculated from the wall current density. Individual species must be assumed to reach instantaneous equilibrium. Equilibrium constants for hydrolysis reactions are available; kinetic rate constants are not. The hyperbolic partial differential equations (PDE's) that describe the transport of reactive species in the crevice are solved numerically with either the "explicit" method, or the Crank-Nicholson method [29,30]. The "explicit" method for solution of these PDE's is represented by the following algorithm:

$$C_{m,n+1} = A(C_{m+1,n} + C_{m-1,n}) + (1 - 2A)C_{m,n} + (\Delta t)R_{m,n} \quad (40a)$$

where $C_{m,n}$ is the lumped-sum concentration at position (m) and time (n); $R_{m,n}$ is the corresponding rate of generation or loss; A is the modulus of the equation; and Δt is the time step. The truncation error for the "explicit" method is:

$$T_{m,n} \leq \frac{A(6A - 1)}{12} Mh^4 \quad (40b)$$

The Crank-Nicholson method is represented by:

$$C_{m,n+1} = \frac{A}{2(1 + A)}(C_{m+1,n+1} + C_{m-1,n+1}) + \frac{(1 - A)}{(1 + A)}C_{m,n} + \frac{A}{2(1 + A)}(C_{m+1,n} + C_{m-1,n}) + \frac{(\Delta t)}{(1 + A)}R_{m,n} \quad (41a)$$

where the truncation error is:

$$T_{m,n} \leq \frac{A}{12} Mh^4 \quad (41b)$$

The modulae for both algorithms are identical and equivalent to:

$$A = \frac{D(\Delta t)}{(\Delta x)^2} \quad (42)$$

In cases involving dissolved metals, the following BC's apply:

$$C_{1,n} = 0 \quad \text{and} \quad C_{m+1,n} = C_{m-1,n} \quad (43a-b)$$

These BC's imply that the concentrations are zero at the crevice mouth (NFE), and that crevices are symmetric about a mirror plane where the flux is zero. The BC's for H^+ and dissolved O_2 are slightly different in that non-zero concentrations are assigned at the crevice mouth. Similar numerical techniques can be used for calculation of the current and potential.

Predicted Environment in Crevice

The Crank-Nicholson method was used to calculate concentration and pH profiles during Phase 1 crevice corrosion, as shown in Figures 8a and 8b, respectively. Soluble iron species included in the calculation were Fe^{2+} , Fe^{3+} , $Fe(OH)^{2+}$ and $Fe(OH)^+$. All precipitated iron is assumed to be $Fe(OH)_2$. Furthermore, it is assumed that: (a) the temperature is 90°C or 363 K; the potential at the mouth of the crevice is at +10 mV relative to the corrosion potential of Alloy 516, the assumed CAM; the solution conductivity is 50,000 $\mu S \text{ cm}^{-1}$; and the diffusion coefficient of all dissolved species is approximately $1.0 \times 10^{-5} \text{ cm}^2 \text{ sec}^{-1}$. Roy et al. have measured relevant corrosion, pitting and repassivation potentials for Alloys 516, 825, 625 and C-22 [20-23]. Results at 0, 600, 1200, 1800, 2400 and 3000 seconds are presented, though calculations were done at intervals of 1 second. The peak in the iron concentration near the crevice mouth is due to the combined effects of a potential that decays with increasing crevice depth (x), and the assumed BC of zero concentration at the crevice mouth. Results obtained with the explicit method are identical.

Calculations for Phase 2 crevice corrosion of Alloy 625 are shown in Figures 9 through 11. Transients in the total concentration of dissolved iron are shown at 0, 600, 1200, 1800, 2400, 3000 and 3600 seconds. Dissolved metal species included in the calculation are Fe^{2+} , $Fe(OH)^+$, Fe^{3+} , $Fe(OH)^{2+}$, Ni^{2+} , $Ni(OH)^+$, Cr^{3+} , $Cr(OH)^{2+}$, $Cr(OH)_2^+$ and Mo^{3+} . Precipitates are assumed to be $Fe(OH)_2$, $Ni(OH)_2$, $Cr(OH)_3$ and $Mo(OH)_3$. It is further assumed that: (a) the temperature is 90°C, or 363 K; the potential at the mouth of the crevice is at +100 mV relative to the pitting potential of Alloy 625, the assumed CRM; the solution conductivity is 1000 $\mu S \text{ cm}^{-1}$; and the diffusion coefficient of all dissolved species is approximately $1.9 \times 10^{-5} \text{ cm}^2 \text{ sec}^{-1}$. Based upon the work of Roy et al. [20-23], the pitting potential is assumed to be +689 mV vs. SCE. As shown in Figures 9a and 9b, the concentrations of dissolved metals rise sharply from zero at the crevice mouth to peak values inside the crevice (~0.3 cm). Recall that the concentrations are assumed to be zero at the crevice mouth. At large distances into the crevice (~0.9 cm), the concentrations fall from the peak values to plateaus. Since H^+ is generated by the hydrolysis of iron, nickel and chromium, and since it is transported in a similar fashion, its transient concentration profiles (not shown) track those of the dissolved metals. Figure 10a shows the pH profiles that correspond to Figures 9a and 9b. In this particular case, it is concluded that reasonable pH values for the crevice solution lie between 2.8 and 3.2 during Phase 2. The concentrations of dissolved metal ions and H^+ are used to calculate Cl^- concentration, as shown in Figure 10b. Alternatively, the Cl^- concentration could be calculated directly from the potential, as suggested by Pickering and Frankenthal [38], as well as Galvele [39]. As shown in Figure 11a, the potential drops to more cathodic values as the distance into the crevice increases. The applied potential at the crevice mouth is assumed to be +1,030 mV vs. NHE (+789 mV vs. SCE). At a depth of 1 cm, the

predicted potential is somewhere between +870 and +910 mV vs. NHE (+630 and +670 mV vs. SCE). The oscillations in the potential profiles are due to the antagonistic effects of chloride and potential on the anodic current density at the crevice wall. More specifically, the anodic current due to localized attack is driven by the difference between the electrode potential, E , and the pitting potential, E_{crit} . The pitting potential is assumed to obey the expression given by Galvele [39]:

$$E_{crit} = A - B \ln[Cl^-] \quad (44)$$

where A and B are constants. Note that B is given as ~ 88 mV for Fe-18Cr-8Ni in NaCl solutions. As the potential in the crevice decreases, the chloride concentration increases, thereby driving the pitting potential to more cathodic levels (less stability). Thus, the anodic current is simultaneously driven by two opposed forces, increasing chloride and decreasing potential. The axial and wall current densities also exhibit oscillations, as shown in Figure 11b. In the future, the data collected by Roy et al. should be used to establish the dependence of E_{crit} on Cl^- concentration [20-23].

Validation Experiments for the Crevice Corrosion Model

Microsensors are being developed and used to map conditions in crevice. Ultimately, fiber optic microprobes should enable in situ determination of pH, Fe(II)/Fe(III), Ni(II), Cr(III)/Cr(VI) and other species. Figure 12 shows preliminary data obtained with a new pH microprobe specifically developed by LLNL for validation of the crevice corrosion model. The 488 nm line from an argon ion laser is used to induce pH-dependent fluorescence in a dye adsorbed at the tip of a fiber optic. The small peak at 514.5 nm is residual output from the laser, while the broad band at 535 nm is the fluorescence. It should also be possible to use microelectrodes to determine local electrochemical potential, O_2 , Cl^- , NO_3^- and SO_4^{2-} , as well as Fe(II)/Fe(III), Ni(II) Cr(III)/Cr(VI) and other species. It may be possible to determine pH, Cl^- , NO_3^- , SO_4^{2-} by other techniques such as miniature ion selective electrodes (ISE's). Other techniques such as Raman spectroscopy could provide valuable insight into processes occurring inside the crevice. Post-test examination of crevice walls with scanning confocal and electron microscopes should provide detailed understanding of the distribution of penetration depth inside the crevice region.

PITTING MODELS

Published Models

Crevice corrosion will result in acidification of the electrolyte and a corresponding elevation in Cl^- concentration. This harsh localized environment may cause pitting, as well as intergranular corrosion. Several pitting models have been reviewed in detail by Farmer [40]. Those for pit initiation include: the halide nuclei theory by Okada [41,42]; the point defect model by Chao, Lin and McDonald [43]; the electrostriction model by Sato [44]; and the stochastic probability model by Shibata [45,46]. Models for pit propagation include: the Pickering-Frankenthal model [38], which assumes passive walls and an active base; the Galvele modification of the Pickering-Frankenthal model [39], which accounts for the effects of metal ion hydrolysis on pH suppression; and the Beck-Alkire model, which deals with a hemispherical pit covered by a thin,

resistive halide film [47]. Henshall was the first to apply probabilistic pitting models to the performance assessment of high-level waste containers [48-50].

Probabilistic Pitting Model

A probabilistic model has been developed for pitting of the CRM in the harsh crevice environment [13,14]. This model divides the container surface into a two-dimensional (2D) array of hypothetical cells, where probabilities for the transition from one pitting state to another can be assigned. As described by Shibata [45,46], nucleation or death of a pit embryo is determined by comparing random numbers to an environment-dependent birth or death probability, respectively. Random numbers are generated by a power residue method. After a pit embryo reaches a critical age, it is assumed to become a stable pit. This approach has already been explored for modeling pit initiation and growth on high-level waste containers by Henshall [48-50]. However, the approach employed by Henshall required additional work to enable it to deal with important environmental parameters, such as pH. Furthermore, that approach used functions for calculating the birth and death probabilities could have values much greater than unity (>1), though the code limited the values to one (≤ 1). It is better to use probability expressions where all calculated values lie between zero and one, as done by Shibata. This feature has now been incorporated into the probabilistic pitting model described here [13,14].

Based upon empirical observations regarding the roles of Cl^- and $E-E_{crit}$ on pit initiation (birth), as well as empirical observations regarding the roles of OH^- and $E-E_{pass}$ on repassivation (death), the following equations are assumed for the rates of embryo birth and death:

$$\lambda_1 = \lambda_0 [Cl^-] \exp\left(\frac{\alpha_\lambda F}{RT} (E - E_{crit})\right) \quad (45)$$

$$\mu_1 = \mu_0 [OH^-] \exp\left(-\frac{\alpha_\mu F}{RT} (E - E_{pass})\right) \quad (46)$$

where $[Cl^-]$ is the concentration of the chloride anion; $[OH^-]$ is the concentration of the hydroxyl anion; F is Faraday's constant; R is the universal gas constant; T is the absolute temperature; E is the electrochemical potential applied to the surface; E_{crit} is the critical pitting potential; E_{pass} is the repassivation potential; α_λ and α_μ are constants; and λ_0 and μ_0 are intrinsic rate constants for the birth and death of embryos, respectively. It is evident that the proposed model involves competitive adsorption of Cl^- and OH^- , which is consistent with the discussion by Strehblow and others [51]. This approach introduces the needed dependence on pH. The rate of converting an embryo into a stable pit is defined here as the transition rate, γ_1 . This conversion process is assumed to be thermally activated and governed by the Ahrenius rate law.

$$\gamma_1 = \gamma_0 \exp\left(-\frac{A_\gamma}{RT}\right) \quad (47)$$

where A_γ is the apparent activation energy and γ_0 is the intrinsic rate constant. In lieu of a transition rate, an induction or incubation time can be used. The induction time, τ_1 , is the age

that an embryo must reach before it can become a stable pit. This quantity is also assumed to obey an Arrhenius-like expression.

$$\tau_1 = \tau_0 \exp\left(-\frac{A_\tau}{RT}\right) \quad (48)$$

where A_τ is the apparent activation energy and τ_0 is the intrinsic induction time. As described by Shibata [Eqns. 63 & 64, Ref. 46], the birth probability in a single cell ($0 < \lambda < 1$) is calculated from the rate as follows.

$$\lambda = 1 - e^{-\lambda_1 \delta t} \quad (49)$$

The death and transition probabilities are calculated in a similar manner.

$$\mu = 1 - e^{-\mu_1 \delta t} \quad (50)$$

$$\gamma = 1 - e^{-\gamma_1 \delta t} \quad (51)$$

At a given time step, an embryo will be born in a vacant cell if the following criteria are met:

$$RND \leq \lambda \quad (52)$$

where RND is a random number. The random number embodies the stochastic nature of pitting events on the surface. Similarly, an existing embryo will die if:

$$RND \leq \mu \quad (53)$$

An embryo will become a stable pit if one of the following criteria are met:

$$RND \leq \gamma \quad (54)$$

$$\tau_{age} \geq \tau_1 \quad (55)$$

where τ_{age} is the age of the embryo under consideration. It was recognized by Henshall that it is necessary to let the birth probability decay with time to obtain a symmetric distribution of pits centered at the mean pit depth [50]. However, model parameters such as the birth probability should be time invariant. An expression for the birth probability is proposed that accomplishes the same end as Henshall's formulation, and avoids explicit use of time as an independent variable.

$$\lambda = \lambda \left(A \theta_p^n \exp[-B \theta_p] \right) \quad (56)$$

where A and B are constants, θ_p is the fractional coverage of the surface by stable pits, and n is the exponent of θ_p . The ability of such "shape factors" to mimic observed pit distributions may

be related to implicit memory effects recognized by Scully and others [52]. More desirable alternatives to Equation 56 should be explored in the future.

Simulations Based Upon Probabilistic Model of Pit Initiation

Figure 13a shows the calculated pit distribution, which is typical of those obtained with the stochastic pitting model with time invariant probabilities. Distinguishing characteristics include: peak near the maximum pit depth; and a long tail. Figure 13b shows the corresponding pit density (cells or number per 100 cm²) as a function of time, based upon the probabilistic model. As expected, the number of vacancies (unpitted area) decreases with time, while the number of stable pits increases. Initially, the number of pit embryos increases rapidly with time. However, the embryo density reaches a maximum and begins to fall at the point where the rate of embryo conversion to stable pits exceeds the rate of embryo births. The overall pit generation rate is proportional to the embryo density, and also passes through a maximum. Calculations were performed with parametric values shown in Table 18. These values enabled the model to mimic the experimental pit distribution data for Alloy 825 that was collected by Roy and published by Henshall [50]. In Roy's experiment, samples were exposed to 5 wt. % NaCl solution at a pH of 2.57 and a temperature of 90°C for 240 minutes. A total of 68 pits were observed in an area of approximately 1 cm². The mean depth was 0.345 mm, with a maximum pit depth of 0.505 mm. These data are used as a "bench mark" for model development.

The effect of pH suppression on pitting of the CRM was investigated with the probabilistic model. These calculations were also performed with the parametric values given in Table 18. Figure 14 shows transients in the vacancy, embryo and stable-pit densities (cells) that were predicted for two cases, direct exposure to the near field environment (NFE), and exposure to the low-pH crevice solution. In the NFE case, the assumed environment is a 1100 ppm NaCl solution at pH ~7 and 60°C. The CRM is assumed to be polarized at a level slightly above the pitting potential, approximately +90 mV vs. SCE. In the crevice case, the assumed environment is a 2000 ppm NaCl solution at pH ~3 and 60°C. Here too the potential is assumed to be approximately +90 mV vs. SCE. The number of vacancies (cells without embryos or stable pits) decreases with time in both cases, while the number of stable pits increases. Initially, the number of pit embryos increases rapidly with time. A maximum is reached at the point where the rate of embryo conversion to stable pits (loss) exceeds the rate of embryo births (generation). The overall pit generation rate is proportional to the embryo density, and also passes through a maximum. Clearly, suppressed pH increases the rate of pit generation, which is consistent with experience. The effect of polarization on the pitting of the inner barrier is illustrated by Figure 15. Case A assumes a 1000 ppm TDS NaCl solution at pH ~7, a temperature of 60°C, and an applied potential of -712 mV vs. SCE, which corresponds roughly to the corrosion potential of the CAM. Case B assumes a 2000 ppm TDS NaCl solution at pH ~3, a temperature of 60°C, and a potential of +90 mV vs. SCE, which corresponds roughly to the pitting potential of the CRM. While rapid pitting of the CRM is predicted for Case B, no pitting is predicted in Case A. The model predicts that the corrosion potential of the CAM provides some protection for the inner barrier.

Deterministic Model of Pit Initiation

A deterministic model has been formulated by Farmer, and can also be used to predict the transients in vacancy, embryo, and stable pit density [13,14]. This model gives results comparable to the stochastic pitting model proposed by Shibata [45,46], but promises to be more computationally efficient. It was motivated by the similarity between adsorption kinetics and the transition probabilities for birth and death presented by Shibata [46]. The fractions of the surface covered by vacancies, embryos and stable pits must sum to one.

$$\theta_E + \theta_V + \theta_P = 1 \quad (57)$$

where θ_E is the fraction of the surface covered by embryos, θ_V is the fraction of the surface that remains vacant, and θ_P is the fraction of the surface covered by stable pits. The accumulation rate of pit embryos on the surface is determined by the difference in birth and death rates.

$$\frac{d\theta_E}{dt} = k_{birth} [Cl^-]^a (1 - \theta_E - \theta_P) - k_{death} [OH^-]^b \theta_E - k_{pit} \theta_E \quad (58)$$

where k_{birth} is analogous to λ_1 , k_{death} is analogous to μ_1 , and k_{pit} is analogous to γ_1 . Consistent with experience, Cl^- is assumed to promote formation of pit embryos, while OH^- is assumed to promote repassivation and embryo death. It is evident that this proposed model involves competitive adsorption of Cl^- and OH^- , which is also consistent with the discussion by Strehblow and others [51]. There is no induction time per se. The accumulation rate of stable pits on the surface is then proportional to the fractional coverage of the surface by embryos.

$$\frac{d\theta_P}{dt} = k_{pit} \theta_E \quad (59)$$

This rate expression assumes that a stable pit evolves from a single embryo. In reality, several embryos may coalesce to form a pit. Thus, the dependence of the pit generation rate on θ_E may not be first order. Coalescence of "n" embryos would give rise to an "n-th order" rate expression. These two first-order, ordinary differential equations can be solved simultaneously by numeric integration with a fourth-order Runge-Kutta algorithm.

Dependence of the Pit Generation Rate on Electrochemical Potential

The probability of initiating localized corrosion are based on the stochastic probability theory of pit initiation, as discussed by Baroux [53]. First, the expression for the survival probability is:

$$\delta P_s = 1 - \bar{\omega} \times \delta S \quad (60)$$

where δP is the survival probability (probability of no pitting) of an infinitesimal area δS on a sample of area S . The survival probability of the entire surface S is then:

$$P_s = \left[1 - \bar{\omega} \times \delta S\right]^{\frac{s}{\delta s}} \quad (61)$$

The pit generation rate, PGR, is then defined in terms of the time derivative of the elementary pitting probability:

$$\frac{d\bar{\omega}}{dt} = g = PGR \quad (62)$$

$$\bar{\omega} = \int_0^t (PGR) dt \quad (63)$$

We then make the following simplification by assuming that PGR is independent of time and that $\delta S \sim S$. While it would be better to avoid such gross over simplification, it does provide some degree of insight into the expected dependence of the survival probability, and the probability of pit initiation, on electrochemical potential. This insight is needed to address the question regarding probability of pitting.

$$P_s \approx 1 - PGR \times t \times S \quad (64)$$

The probability of pitting (localized corrosion, LC) is then assumed to be:

$$P_{LC} \approx PGR \times t \times S \quad (65)$$

It is observed empirically that:

$$\ln(PGR) \approx \beta (E - E_{pit}) \quad (66a)$$

Therefore:

$$\ln\left(\frac{P_{LC,1}}{P_{LC,2}}\right) \approx \ln\left(\frac{PGR_1}{PGR_2}\right) \approx \beta (E_1 - E_2) \quad (66b)$$

We can estimate the empirical constant β as:

$$\beta = \frac{\ln(P_{LC,1}/P_{LC,2})}{(E_1 - E_2)} \quad (66c)$$

For the purpose of illustration, consider a hypothetical case where the repassivation potential is assumed to be the point at which there is a 5% chance of initiating localized corrosion. Furthermore, assume that the average repassivation potential is 800 mV vs. SHE, and that the observed scatter around the average ± 50 mV. The probability of initiating localized corrosion at

800 mV vs. SHE is assumed to be 5%, and the probability of initiating localized corrosion at 800-50 mV vs. SHE is assumed to be 1%. In this hypothetical case,

$$\beta = \frac{\ln(5/1)}{(800 \text{ mV} - 750 \text{ mV})} \approx 0.032 \text{ mV}^{-1} \quad (66d)$$

Based upon these assumptions, the maximum probability of pitting is calculated to be less than 15% at the 99th percentile, with typical values of 0.01 to 2.12% at the 50th percentile.

Electrochemical Potential

It is believed that the electrochemical potential at the mouth of the crevice will be somewhere between the mixed potential of A516 Gr 55 and Alloy C-22, in either concentrated J-13 or a representative crevice solution (10 wt. % FeCl₃). In the absence of FeCl₃, the greatest mixed potential at 90°C is expected to be somewhere between -520 and -24 mV vs. SHE. With 10 wt. % FeCl₃, potentials as high as +714 mV vs. SHE have been observed (Table 19). Since the observed mixed potential has never exceeded the pitting or repassivation potentials, localized attack is not expected. Several candidate CRM's were anodically polarized in 5 wt. % NaCl at pH 2.7, as illustrated by Figure 16. Severe pitting was observed in Alloy 825 at 600 mV vs. Ag/AgCl ($E > E_{\text{pass}}$). In contrast, no pitting was observed in Alloy C-22 at the same potential ($E < E_{\text{pass}}$). Data summarized in Table 20 also indicates no localized attack of Alloy C-22 at potentials below the repassivation potential ($E < E_{\text{pass}}$).

From transport modeling of corrosion in the CAM-CRM crevice, it is known that the electrochemical potential inside the crevice is less anodic (less severe) than the potential established or applied at the mouth of the crevice [13,14]. This is due to ohmic drop along the length of the crevice. Consequently, any estimate of corrosion rate based on the electrochemical potential at the crevice mouth, coupled with the assumption of suppressed pH and elevated chloride inside the crevice, should be conservative.

Smailos, Schwarzkopf, and Koster state [25]: "Hastelloy C-4 has also resisted pitting corrosion and stress corrosion cracking, in the absence of irradiation, and its corrosion rate has been low at all testing temperatures ($< 1 \mu\text{m y}^{-1}$), but it has been attacked by crevice corrosion." However, they go on to state that when it is exposed to gamma irradiation at $\sim 10^5 \text{ rad h}^{-1}$, pitting corrosion was observed. This pitting corrosion is believed by several investigators in the field to be due to the formation of oxidants such as H₂O₂, which shift the corrosion potential in the anodic direction, closer to the pitting and repassivation potential. Glass performed definitive radiolysis experiments at LLNL showing that the corrosion potential of 316L stainless steel in 0.018 M NaCl at 30°C shifted from approximately -100 mV vs. SCE to approximately +100 mV vs. SCE when exposed to gamma irradiation ($3.3 \times 10^6 \text{ rad h}^{-1}$) from a Co-60 source [8]. The level of radiation expected at the outer surface of the CRM at the instant of CAM penetration is estimated to be several orders-of-magnitude less than these exposures (10^5 - 10^6 rad h^{-1}). Note that radiolysis could also form other oxidants. However, such effects are not expected to be great at low levels of radiation.

Growth and Stifling of Stable Pits

Propagation of a stable pit requires that the local electrochemical potential remain above a threshold ($E > E_{pass}$). If this condition is met, propagation occurs at a rate that is depth-dependent. The depth can be calculated from the age of the pit. As the pit becomes deeper, the rate becomes slower due to mass transport limitations. The maximum possible depth can then be estimated with an appropriate stifling criterion, which is based upon a limiting mass flux.

Determination of the distribution of pit depths requires calculation of the pit penetration, d , which is a function of pit age, T_{age} . The corresponding penetration rate can be assumed to be limited by either diffusion or electromigration. Both cases yield a square-root dependence of the pit depth on time. Diffusion-limited penetration will be discussed briefly in the following section. Here, for the sake of illustration, the penetration is assumed to obey the following empirical expression:

$$d = \sqrt{2 K T_{age}} \quad (67a)$$

where the rate constant, K , is defined as:

$$K = K_0 [H^+] (E - E_{crit}) \quad (67b)$$

where K_0 is a constant; $[H^+]$ is the hydrogen ion concentration; E is the applied voltage; and E_{crit} is the critical pitting potential. It should be noted that this expression implies growth driven by the electric field. Future pitting calculations should use assumptions that are more consistent with those implicit in the crevice model, such as the assumption of a strong supporting electrolyte.

In principle, a pit will cease to grow (i.e., die) if the depth becomes so great that the current density at the base of the pit falls below the passive current density. The importance of "stifling" has also been pointed out by Marsh [54]. In the case of pit propagation in carbon steel, Marsh gives the following criterion based upon the passive current density and the diffusive flux of dissolved oxygen:

$$\frac{i_{pass}}{4F} \leq -D \left. \frac{\partial C(x,t)}{\partial x} \right|_{x=0} \quad (68)$$

where i_{pass} is the passive current density at the base of the pit, F is Faraday's constant, D and C are the diffusivity and concentration of dissolved oxygen, respectively, x is the distance into the pit from the mouth of the pit, and t is time. It was noted that careful measurements of i_{pass} are required for any theoretical analysis. The critical concentration gradient across the pit is estimated to be:

$$-\left. \frac{\Delta C}{\Delta x} \right|_{critical} \geq \frac{i_{pass}}{4FD} \quad (69)$$

Alternatively, given a maximum possible differential concentration of dissolved oxygen, the maximum possible pit depth at stifling (death) can be calculated.

$$\Delta x \leq -\frac{4FD\Delta C}{i_{pass}} \quad (70a)$$

The largest critical pit depth occurs when the dissolved oxygen is saturated at the mouth of the pit, and entirely depleted at the base of the pit ($\Delta C \approx 0 - C_{sat}$).

$$\Delta x \leq \frac{4FDC_{sat}}{i_{pass}} \quad (70b)$$

Estimates of the critical pit depth, based upon the diffusion-limited current density associated with oxygen reduction are summarized in Table 21. The following assumptions were made: (a) $F = 9.64846 \times 10^4$ C equiv⁻¹; (b) $D \sim 10^{-5}$ cm² sec⁻¹; and (c) $i_{pass} = 4 \times 10^{-6}$ A cm⁻². The oxygen solubilities were given by Andresen [55].

An alternative criterion for pit stifling can be formulated based upon the diffusion-limited flux of dissolved metal inside the pit. In the case of a multicomponent material such as Alloy C-22, the modified stifling criterion can be expressed in terms of the total concentration gradient of the i-th dissolved metal (Fe, Ni, Cr, Mo or W):

$$\left. \frac{\Delta C_i}{\Delta x} \right|_{critical} \geq \frac{f_i i_{pass}}{n_i F D_i} \quad (71a)$$

where C_i is the total concentration of the i-th dissolved metal; x is the distance from the mouth of the pit; f_i is the mole fraction of the passive current producing the i-th dissolved metal, i_{pass} is the passive current density at the base of the pit; n_i is the the number of electrons involved in the anodic dissolution of the i-th dissolved metal; F is Faraday's constant; and D_i is the apparent or overall diffusivity of the i-th dissolved metal. In order to transport dissolved metal out of the pit without accumulation, precipitation, passivation, and stifling, this critical concentration gradient must be maintained. If one assumes (a) $f_i = 0.01$, (b) $i_{pass} = 4 \times 10^{-6}$ A cm⁻², (c) $n_i = 6$, (d) $F = 9.64846 \times 10^4$ C equiv⁻¹, (e) $D_i \sim 10^{-5}$ cm² sec⁻¹ and (f) $\Delta x = 2$ cm, the critical differential concentration, ΔC_i , is estimated to be 1.38×10^{-8} mol g⁻¹ (1.38×10^{-5} mol kg⁻¹). Values of the mole fraction, f_i , are given in Table 22. Note that the solubility of WO_3 is only $\sim 10^{-10}$ mol kg⁻¹ at pH ~ 2 . If any dissolved species at the base of the pit has a solubility less than this limiting value, the pit will die before wall penetration is achieved. Alternatively, given a maximum possible differential concentration, the maximum possible pit depth at stifling (death) can be calculated.

$$\Delta x \leq \frac{n_i F D_i \Delta C_i}{f_i i_{pass}} \quad (71b)$$

The largest differential concentration and the largest critical pit depth occur when the solution at the base of the pit is saturated and when the concentration at the mouth of the pit is zero.

$$\Delta x \leq \frac{n_i F D_i C_{sat,i}}{f_i i_{pass}} \quad (71c)$$

The solubilities of various oxides and hydroxides believed to be formed during dissolution of Alloy C-22 are given by Pourbaix [56]. From the solubility vs. pH curves given by Pourbaix, it appears that the following empirical relationship is obeyed over limited ranges of pH:

$$\log[C_{sat,i}] = m_i \times [pH] + b_i \quad (71d)$$

Where $C_{sat,i}$ is the concentration of the i-th dissolved metal at saturation (mol kg^{-1}), m_i is the slope and b_i is the intercept. Values of the slope and intercept were estimated from the curves of Pourbaix and are also given in Table 23. This abstracted model for solubility was used to estimate the logarithms of solubilities given in Table 24.

Based upon the estimated solubilities given in Table 24, the critical pit depths were calculated and are given in Table 25. Ranges of pH where localized corrosion is stifled by a particular film-forming compound correspond to "maximum possible pit depths" that are less than the thickness of the CRM. The pit depth is limited to a different extent by each oxide or hydroxide. At low pH, MoO_3 and WO_3 appear to be primarily responsible for the superior corrosion performance of Alloy C-22. Based upon this calculation, one would expect the localized corrosion of Alloy C-22 to be stifled over the entire range of pH, extending from -1 to 10. This is consistent with observations in acidic media of interest (simulated crevice solution of 10 wt. % FeCl_3). There are unusual acidic environments where corrosion is known to occur. Both experience and calculation appear to indicate that pits should not propagate in Alloy C-22 during exposure to crevice conditions. Soluble oxychlorides have not been considered in the initial calculation, but should be included in future calculations.

STRESS CORROSION CRACKING

Criterion for SCC

For stress corrosion cracking (SCC) to occur three factors have to exist: stress; a flaw (crack initiation site); and a material-specific corrosive environment. Flaws can either pre-exist due to poor manufacturing practices, or be initiated at locations where high stress concentration exists, such as grooves and corrosion pits. Stress can exist due to welding residual stress, shrink-fit stress, or weight stress. These contributions to stress are illustrated by Figure 17 and are summarized in Table 26. Fracture mechanics is by far the best approach to assess the tendency for stress corrosion cracking to occur. Once a crack is initiated, the crack will grow by SCC when the applied stress intensity factor, K , is equal to or larger than SCC resistance parameter, K_{ISCC} .

$$K \geq K_{ISCC} \quad (73)$$

K_{ISCC} is a material and environment dependent property which can be obtained through fracture mechanics testing of the materials in the specified environment. The stress intensity factor can be calculated with the following fracture mechanics formula:

$$K = \beta \sigma (\pi a)^{1/2} \quad (74)$$

where β is a geometry factor dependent on the shape of the crack. For a surface elliptical crack with depth (a) and length ($2c$) under tensile loading, β depends upon the aspect ratio ($a/2c$). The solutions for β are readily available in typical fracture mechanics textbooks such as the one written by Anderson [57], and will not be duplicated here. Equation 74 applies only to an ideal crack. For a corrosion pit, a small crack must be initiated at the base of the pit before it can grow by SCC. A crack can be initiated in several ways such as over-load induced tearing, grain boundary sensitization, or breakage of a near-by inclusion. To determine exactly when a small crack will be initiated is a difficult task. In our analysis, we assume that a crack fissure with the length of δa is readily developed along the base of the pit on the plane normal to the applied stress direction. It is further assumed that δa is determined by the size of one grain, which is estimated to be approximately 40 microns (0.0015 inches). An idealized crack initiation site is illustrated in Figure 18. Under this situation, the criteria for this crack to continue to grow by SCC can be expressed by the following formula:

$$K = \alpha \beta \sigma [\pi (a_{pit} + \delta a)]^{1/2} \quad (75)$$

where a_{pit} is the depth of the pit, β is a geometry factor dependent on the depth and aspect ratio of the pit (as described in Equation 74), and α is another geometry factor that accounts for the fact that the pit and crack fissure do not constitute an ideal crack. The solution for α has been derived by Newman in graphical form [58]. It should be noted that for the asymptotic situation where the crack fissure size is much less than the depth of the corrosion pit ($\delta a \ll a_{pit}$) the applied stress intensity factor can be expressed as:

$$K = \beta K_t \sigma (\delta a)^{1/2} \quad (76)$$

where K_t is the elastic stress concentration factor at the tip of the pit and is calculated as:

$$K_t = 1 + \frac{2a}{c} \quad (77)$$

Stress Analysis

SCC of A516 Gr 55, Alloy 625 or Alloy C-22 can initiate at a pre-existing flaw or pit of critical size, provided that there is adequate stress. It is assumed that there are three contributions to the stress of an unperturbed high-level waste container: weight stress, shrink-fit stress; and weld stress. In the base metals of containers, the only stresses which exist are the weight stress and shrink-fit stress.

Weight Stress

The weight stress can be calculated by the elasticity theory of a beam, which is given as:

$$\sigma = \frac{M r}{I} \quad (73)$$

where the stress along the longitudinal direction of the container is σ and the distance of any location of interest away from the center-axis of the container is r . The moment of inertia of the cross section of the container is I :

$$I = \frac{\pi(r_o^4 - r_i^4)}{4} \quad (74)$$

where r_o and r_i are the outer and inner radius of the cylinder container. For the analysis of the outer barrier, r_o is taken as 0.825 m (32.48 in) and r_i is taken as 0.725 m (28.54 inches). For the analysis of the inner barrier, r_o is taken as 0.725 m (28.54 inches) and r_i is taken as 0.705 m (27.75 inches). Equation 75 is used to calculate M in equation 73:

$$M = \frac{1}{8pL^2} \quad (75)$$

where L is the length of the container between base supports of the container and p is the uniformly-distributed weight along the length of the container. In our analysis, L is taken as half of the total container length ($L = 2.67$ m). The weight of the package, W , is estimated to be 50,423 kg. Then p can be calculated as:

$$p = \frac{W}{2L} \quad (76)$$

Based on the above equations, the maximum weight stresses calculated for container system are 0.46 MPa in the CAM (A516 Gr 55) and 2.6 MPa in the CRM (Alloy 625 or C-22).

Shrink-fit Stress

The stresses due to the shrink fitting of two cylinders is treated by Shigley and Mischke [59]. At the outer surface of the CAM, the tangential shrink-fit stress can be calculated as

$$\sigma_o = 2p \left[\frac{R^2}{(r_o^2 - R^2)} \right] \quad (77)$$

At the CAM-CRM interface, the maximum tangential stress in the inner cylinder (CRM) can be calculated as:

$$\sigma_i = p \left[\frac{(R^2 + r_i^2)}{(R^2 - r_i^2)} \right] \quad (78)$$

where r_o is the outer radius of the CAM, taken as 0.825 m (32.48 in); R is the inner radius of the outer container, taken as 0.725 m (28.54 inches); and r_i is the inner radius of the inner container, taken as 0.705 m (27.75 inches). The contact pressure on the CAM-CRM interface due to the slight over-size of the outer radius of the CRM relative to the inner radius of the CAM is:

$$p = \frac{E \delta}{R} \left[\frac{(r_o^2 - R^2)(R^2 - r_i^2)}{2R^2(r_o^2 - r_i^2)} \right] \quad (79)$$

where the oversize is quantified through the radial interference, δ , which is assumed to be 0.89 mm (0.035 inches). The elastic modulus, E , of both the CAM and CRM was assumed to be approximately 207,000 MPa (30,000 ksi) in this preliminary analysis. Based on the above equations, the contact pressure is calculated as 5.85 MPa (847.5 psi), the shrink-fit stress at the outer surface of the CAM is calculated as 40 MPa (5,742 psi), and the maximum shrink-fit stress for the CRM is calculated as -207 MPa (30,199 psi), which is a compressive stress. It is noted that the maximum shrink-fit stress of the CRM will approach zero as the CAM undergoes corrosive dissolution. Therefore, the shrink-fit stress in the CRM is assumed to be zero.

Weld Stress

In the welds, the welding residual stress has to be considered. In the fabrication of the waste package containers, the welds will be mostly stress relieved except the final closure weld which has not been specified to be relieved. In this case, the welding residual stress can be as high as the yield strength of the material. The yield strength is 205 MPa for A516 Gr 55; 407 MPa for Alloy C-22; and 483 MPa for Alloy 625 [60].

SCC Resistance

Fracture mechanics SCC testing has been performed on Alloys 625 and C-22 by Roy [61]. Preliminary measured values of K_{ISCC} are 30 MPa $m^{1/2}$ for Alloy C-22 and 33 MPa $m^{1/2}$ for Alloy 625. These values are summarized in Table 27 and were used in this preliminary analysis to determine whether or not SCC will occur in flaws or corrosion pits developed in these alloys.

For carbon steel, a correlation between K_{ISCC} and Vicker hardness has been reported for aqueous solutions of NaCl (3.5 wt. %) [62]. Since the Vicker hardness for A516 Gr 55 carbon steel is typically 120, the K_{ISCC} of this material is estimated to be approximately 71 MPa $m^{1/2}$.

Results of SCC Analysis

Corrosion pits can be developed at welds and base metals of waste package containers after long exposure to the environment. These act as stress risers to initiate crack fissures at the bases of the pits. SCC can be initiated at these pits when the applied stress intensity factors are equal to

or larger than K_{ISCC} . Using the expression for K given as Equation 75 and the K_{ISCC} data from the previous section, the critical flaw size for initiation can be defined ($K = K_{ISCC}$). These critical flaw sizes have been calculated and are given in Table 28 as a function of aspect ratio ($a/2c$) at various stress levels. Note that the critical flaw sizes for SCC initiation is always larger than the thickness of the respective barriers, except at extremely high aspect ratio ($a/2c \sim 5$). At this very high aspect ratio ($a/2c \sim 5$), the critical flaw sizes for SCC initiation in unannealed welds of Alloys 625 and C-22 are 1.2 cm and 1.4 cm, respectively. Since these values are somewhat less than the wall thickness (2 cm), SCC may be possible in the unannealed closure weld. Since stresses in the base metals are expected to be much lower than that in the corresponding, unannealed welds, it is concluded that SCC should not occur in the base metals. Even though the weld residual stress can be very high, it has been observed by Henshall and Roy that the aspect ratio of corrosion pits in Alloy 825 seldom exceeds one ($a/2c < 1$) [50]. Such pits are shown in Figure 16. The results in Table 30 suggest that SCC will not occur at corrosion pits at welds, even if the welds are not stress relieved.

It must be noted that the current analysis is based on linear elastic fracture mechanics. When the stress applied on a crack or corrosion pit is close to or beyond yield stress, there is a possibility that the linear elastic fracture over estimates the critical flaw size for initiation of SCC. Under this situation, elastic-plastic fracture mechanics based on the J-integral approach should be used. In order to use this elastic-plastic fracture mechanics approach, accurate stress-strain curves for each material is needed to characterize its strain-hardening behavior. We will pursue such data and conduct elastic-plastic fracture mechanics analysis in the future. In the interim stage, we recommend that the maximum stress on the welds be relieved to less than 75% of the yield strength of the material.

THERMAL EMBRITTLEMENT

Background on Thermal Embrittlement

In the current repository design, the temperature of high-level waste containers loaded with 10-year spent nuclear fuel (SNF) is expected to reach a peak temperature of 200°C after 10 years of emplacement. The waste package will require approximately 1000 years to cool to 100°C. This extended period at elevated temperature has lead to concern regarding the possibility of thermal embrittlement (TE), which is also known as temper embrittlement. It is well known that fracture toughness in steels, especially in low alloy steels, is severely reduced by isothermal aging or slow cooling in the 350 to 575°C range. It is also recognized that the segregation of impurities such as Sb, P, Sn, and As at grain boundaries is the main cause of TE. The most potent embrittling elements, in order of decreasing potency, are As, Sn, P and Sb. However, Sb, Sn and As are not generally present in steels. Thus, phosphorous poses the greatest threat of TE in materials such as A516. McMahon has concluded in his review that plain carbon steels containing less than 0.5 wt. % Mn are not susceptible to TE [63]. However, higher levels of Mn may enhance P-induced TE. It is apparent that not enough data exist on the long-term aging of carbon steels to completely disregard the possibility of TE, especially in the case of high-Mn steels.

TE Predictive Model

To address this issue, we have analyzed the segregation of P in steels after both a typical thermal embrittlement cycle at 350-575°C, and a typical temperature cycle expected in a high-level waste container. These two profiles are shown in Table 29.

Estimates of the extent TE rely on both thermodynamics, kinetics and transport phenomena. McLean developed a theory of grain boundary segregation using statistical thermodynamics [64]. His expression (Equation 80) is used to calculate the segregation of P at grain boundaries after thermodynamic equilibrium is reached:

$$\frac{X_b}{(1 - X_b)} = \left[\frac{X_c}{(1 - X_c)} \right] \exp\left(-\frac{\delta G}{RT}\right) \quad (80)$$

where X_b is the equilibrium fraction of grain boundary being covered with a monolayer of the impurity of concern, X_c is the solubility of the impurity in the matrix, and δG is the Gibbs free energy of segregation. For phosphorous segregation in steel, Bruce and his coworkers have derived δG as a function of temperature, T , based upon experimental data [65]. This is represented by Equation 81.

$$\delta G(J/mol) = -63000 + 21.0 \times T(K) \quad (81)$$

The solubility of P in steels, X_c , can be estimated by inspection of the Fe-P phase diagram [66]. Two data points, one at 400°C and another at 443°C, were obtained and fit to an Arrhenius expression:

$$X_c = 0.19 \times \exp\left[-\frac{2598}{T}\right] \quad (82)$$

where T is given in Kelvins. McClean also developed a theory for the kinetics of grain boundary segregation. The fraction of grain boundary coverage ($X_b(t)$) at a given time (t) and temperature (T) is given as:

$$\frac{[X_b(t) - X_b(0)]}{[X_b - X_b(0)]} = 1 - \exp\left[-\frac{4Dt}{\beta^2 f^2}\right] \operatorname{erfc}\left[\frac{4Dt}{\beta^2 f^2}\right]^{0.5} \quad (83)$$

where D is the diffusion coefficient of the solute (phosphorous) and β is the grain boundary enrichment ratio (X_b/X_c). The remaining parameter (f) is defined as:

$$f = \frac{a^3}{b^2} \quad (84)$$

where a and b are the atomic sizes of the matrix and impurity elements, respectively. For phosphorous in steels, it is assumed that a and b are 1.24 and 1.0 Å, respectively. Bruce developed the following expressing for the diffusion coefficient.

$$D = 0.25 \exp \left[- \frac{20000(J/mol)}{RT} \right] \quad (85)$$

TE Analysis

Equations 80 through 85 were used to calculate segregation in steel (the fraction of grain boundary being covered with a monolayer of P) after the typical TE cycle in steels and the expected waste package temperature cycle. The results are shown in Table 31 and indicate that the total grain boundary segregation of P after the typical TE cycle is 0.97, while that for the expected waste package temperature cycle is only 0.012. The segregation expected for the waste package is only about 1.2% of that for the typical TE cycle in steels. Therefore, we conclude that TE in the CAM is very unlikely.

MICROBIAL INFLUENCED CORROSION

The possible acceleration of abiotic corrosion processes by microbial growth has also been a concern. Bacteria and fungi alter local environment in biofilm. For example, H^+ is known to be generated by bacterial isolates from Yucca Mountain [67]. Furthermore, thiobacillus ferrooxidans oxidize Fe^{2+} , while geobacter metallireducens reduce Fe^{3+} . Other microbes can reduce SO_4^{2-} and produce S^{2-} . In the future, we hope to calculate concentration transients in biofilms with a relatively simple bioreactor model.

SUMMARY

Concentration profiles inside the CAM-CRM crevice have been calculated, first during corrosive attack of the CAM wall, then during corrosive attack of the CRM wall. A peak is predicted in the iron concentration near the crevice mouth due to the combined effects of a potential that decays with increasing crevice depth, and the assumed BC of zero concentration at the crevice mouth. Calculations for corrosive attack of the CRM wall have also been performed. The predicted concentrations of dissolved metals rise sharply from zero at the crevice mouth to peak values inside the crevice. At large distances into the crevice, the predicted concentrations fall from the peak values to plateaus. Since H^+ is generated by the hydrolysis of dissolved metals, and since it is transported in a similar fashion, its predicted concentration profiles (not shown) track those of the dissolved metals. In general, the pH is found to approach an asymptotic value (pH~3). Such representative values can be used as input for predictive pitting models.

In simulations, the number of vacancies (unpitted area) decreases with time, while the number of stable pits increases. Initially, the number of pit embryos increases rapidly. The embryo density eventually reaches a maximum and begins to fall at the point where the rate of embryo conversion to stable pits exceeds the rate of embryo births. The overall pit generation rate is proportional to the embryo density, and passes through a maximum. The effect of pH suppression and imposed potential on pitting of the CRM has also been simulated. The predicted

rate of pit generation is enhanced by pH suppression, which is consistent with experimental observation. These models predict that the corrosion potential of the CAM provides some protection for the CRM within the crevice.

Propagation of a stable pit requires that the local electrochemical potential remain above a threshold ($E > E_{\text{pass}}$). If this condition is met, propagation occurs at a rate that is depth-dependent. The depth can be calculated from the age of the pit. As the pit becomes deeper, the rate becomes slower due to mass transport limitations. The maximum possible depth can then be estimated with an appropriate stifling criterion, which is based upon a limiting mass flux.

Corrosion pits can be developed at welds and base metals of waste package containers after long exposure to the environment. These act as stress risers to initiate crack fissures at the bases of the pits. SCC can be initiated at these pits when the applied stress intensity factors are equal to or larger than K_{ISCC} . The critical flaw size for initiation of SCC can be defined by equating K and K_{ISCC} . These critical flaw sizes have been calculated as a function of aspect ratio ($a/2c$) at various stress levels. Note that the critical flaw sizes for SCC initiation is always larger than the thickness of the respective barriers, except at extremely high aspect ratio ($a/2c \sim 5$). At this very high aspect ratio ($a/2c \sim 5$), the critical flaw sizes for SCC initiation in unannealed welds of Alloys 625 and C-22 are 1.2 cm and 1.4 cm, respectively. Since these values are somewhat less than the wall thickness (2 cm), SCC may be possible in the weld. Since stresses in the base metals are expected to be much lower than that in the corresponding, unannealed welds, it is concluded that SCC should not occur in the base metals. Even though the weld residual stress can be very high, it has been observed by Henshall and Roy that the aspect ratio of corrosion pits in Alloy 825 seldom exceeds one ($a/2c < 1$). Preliminary results suggest that SCC will not occur at corrosion pits at welds, even if the welds are not stress relieved.

It must be noted that the current analysis is based on linear elastic fracture mechanics. When the stress applied on a crack or corrosion pit is close to or beyond yield stress, there is a possibility that the linear elastic fracture overestimates the critical flaw size for initiation of SCC. Under this situation, elastic-plastic fracture mechanics based on the J-integral approach should be used [Anderson, 1995]. In order to use this elastic-plastic fracture mechanics approach, accurate stress-strain curves for each material is needed to characterize its strain-hardening behavior. We will pursue such data and conduct elastic-plastic fracture mechanics analysis in the future. In the interim stage, we recommend that the maximum stress on the welds be relieved to less than 75% of the yield strength of the material.

Estimates of the extent TE rely on both thermodynamics, kinetics and transport phenomena. Such models have been used to calculate segregation in steel (the fraction of grain boundary being covered with a monolayer of P) after the typical TE cycle in steels and the expected waste package temperature cycle. Preliminary results indicate that the total grain boundary segregation of P after the typical TE cycle is 0.97, while that for the expected waste package temperature cycle is only 0.012. The segregation expected for the waste package is only about 1.2% of that for the typical TE cycle in steels. Therefore, we conclude that TE in the CAM is very unlikely.

FUTURE WORK

The stability of the passive film formed on Alloy C-22 should be determined with the scanning tunneling microscope (STM) and the atomic force microscope (AFM). These techniques provide means of generating in situ high-resolution images of the alloy surface. In the case of STM, atomic resolution may be possible, provided that the passive film is sufficiently conductive [68-70].

Microsensors and in situ optical techniques should be employed to actually measure the localized environment inside the CAM-CRM crevice. Fiber optic microprobes (fluorescence, absorption, and inelastic Raman scattering) should be used to determine pH, as well as the concentrations of dissolved metals and anions. Microelectrodes should be used to establish potential profiles within the crevice. Such measurements will eliminate much of the need for speculation about the crevice environment. Such sensors have already been demonstrated at LLNL and will be applied to this important problem in the future, provided that funding is maintained. In specific regard to Alloy C-22, it may be possible to use interferometry and other reflection techniques (ellipsometry, etc.) to quantify the very small penetration rates anticipated in crevices. For example, an artificial crevice could be formed beneath a quartz optical window, with FeCl_3 additions to simulate the dissolved CAM.

Thin-film corrosion sensors should be fabricated and deployed in the drifts at Yucca Mountain (ESF) to continuously monitor corrosion rates of A516 Gr 55, Alloy C-22, and other metallic alloys of interest. Such films can be deposited on piezoelectric crystals so that mass change due to corrosion can be measured. Alternatively, the resistance through a sputtered thin film of the material can also be monitored. Such atmospheric corrosion studies are now being conducted at LLNL to study the impact of various gas-phase impurities on the tarnish rate of unprotected metallic mirrors in the National Ignition Facility. Phase stability could be studied with sputtered multilayers (well defined, calibrated microstructure).

Process-level (mechanistic) models for pitting and crevice corrosion should be further developed and improved so that experimental data can be used for reliable predictions on the repository time frame. The CAM-CRM crevice transport model should be enhanced to include: (a) localized concentration- and temperature-dependent solution conductivity; (b) terms to account for electromigration at low ionic strengths; (c) equations to account for sulfate, nitrate, carbonate, and other anions; (d) an appropriate activity coefficient model; (e) improved computationally-efficient model of solution equilibria, including proper hydrolysis equilibrium constants; (f) ability to deal with variable width crevice; (g) ability to account for localized breakdown of the passive film within the crevice; and (h) a rigorous criterion for cessation of localized attack. Improvements are also needed in the stochastic pitting model, as previously discussed.

The correlations presented here are viewed as a starting point, and require continuous improvement and updating. More appropriate, non-linear functional forms should be explored. Such functional forms will enable TSPA to interpret coefficients as activation energies, orders of reaction, and related kinetic parameters. Modification of the existing test matrix should be

considered. By adding additional test conditions as needed, which require additional water-filled tanks, it may be possible to achieve the advantages of a factorial design.

All cyclic polarization measurements should be accompanied by microscopic photographs, and perhaps even images generated by a scanning electron microscope (SEM), to substantiate the absence of localized corrosion below threshold potentials (repassivation potential, etc.). This approach has been successfully employed with great success by others [10], and should be emulated by LLNL.

It is believed that uncertainty regarding the waste package environment is the largest source of uncertainty on corrosion modeling. Significant effort must be expended by the entire program to reduce this uncertainty, and to provide those involved in TSPA and materials testing with well-specified anticipated environments.

ACKNOWLEDGEMENTS

This work was done under the auspices of the U.S. Department of Energy (DOE) by Lawrence Livermore National Laboratory (LLNL) under Contract No. W-7405-Eng-48.

REFERENCES

1. D. A. Jones, B. E. Wilde, "Galvanic Reactions During Localized Corrosion on Stainless Steel," *Corrosion Science*, Vol. 18, 1978, pp. 631-643.
2. J. K. McCoy, "Limits on pH for Waste Package Crevice Corrosion," Private Communication, August 11, 1997.
3. Z. Szklarski-Smialowska, "Pitting Corrosion of Metals," NACE, Houston, TX, 1986, p. 311-312.
4. R. S. Lillard, J. R. Scully, Modeling of the Factors Contributing to the Initiation and Propagation of the Crevice Corrosion of Alloy 625, *J. Electrochem. Soc.*, Vol. 141, No. 11, 1994, pp. 3006-3015.
5. H. P. Hack, Crevice Corrosion Behavior of Molybdenum-Containing Stainless Steel in Seawater, *Materials Performance* Vol. 22, No. 6, 1983, pp. 24-30.
6. Haynes International, Inc., Hastelloy Alloy C-276, Haynes Product Brochure H-2002B, Haynes International, 1987.
7. A. I. Asphahani, Corrosion Resistance of High Performance Alloys, *Materials Performance*, Vol. 19, No. 12, 1980, pp. 33-43.
8. R. S. Glass et al., Gamma Radiation Effects on Corrosion: I. Electrochemical Mechanisms for the Aqueous Corrosion Processes of Austenitic Stainless Steels Relevant to Nuclear Waste Disposal in Tuff, *Corrosion Science*, Vol. 26, No. 8, 1986, p. 577-590.

9. J. C. Farmer, Table 13 in "Waste Package Degradation Expert Elicitation Panel: Input on the Corrosion of CRM Alloy C-22," Rev. 7, Geomatrix, San Francisco, CA, March 14, 1998, 30 p.
10. K. A. Gruss, D. S. Dunn, G. A. Cragnolino, N. Sridar, "Repassivation Potential for Localized Corrosion of Alloys 625 and C-22 in Simulated Repository Environments," Paper No. 149, Symposium on Corrosion in Nuclear Systems, 98-T-2A, Annual Meeting of the National Association of Corrosion Engineers (NACE), Corrosion 98, San Diego, CA, March 22-27, 1998, 15 p.
11. R. Hopper, J. Farmer, K. Wilfinger, "Summary of Model to Account for Inhibition of CAM Corrosion by Porous Ceramic Coating," UCRL-ID-130502, University of California, Lawrence Livermore National Laboratory, April 24, 1998, 10 p.
12. J. C. Farmer, "Development of Corrosion Models for High-Level Waste Containers," Proceedings of the 6th International Conference on Nuclear Engineering, ICONE-6, May 10-15, 1998, ASME, 1998, 13 p.
13. J. C. Farmer, "Crevice Corrosion and Pitting of High-Level Waste Containers: A First Step Towards the Integration of Deterministic and Probabilistic Models," UCRL-ID-128381, University of California, Lawrence Livermore National Laboratory, July 1997, 98 p.
14. J. C. Farmer, R. D. McCright, "Crevice Corrosion and Pitting of High-Level Waste Containers: Integration of Deterministic and Probabilistic Models," UCRL-ID-127980, Part 1, University of California, Lawrence Livermore National Laboratory, October 13, 1997, 24 p.; Paper No. 160, Symposium on Corrosion in Nuclear Systems, 98-T-2A, Annual Meeting of the National Association of Corrosion Engineers (NACE), Corrosion 98, San Diego, CA March 22-27, 1998, 24 p.
15. G. A. Henshall, "Numerical Predictions of Dry Oxidation of Iron and Low-Carbon Steel at Moderately Elevated Temperatures," UCRL-JC-124639, University of California, Lawrence Livermore National Laboratory, November 1996.
16. G. E. Gdowski, "Kelvin Effect on Capillary Condensation," Unpublished Data, University of California, Lawrence Livermore National Laboratory, 1998.
17. T. K. Sherwood, P. L. Pigford, C. R. Wilke, Mass Transfer, McGraw-Hill, San Francisco, 1975, pp. 178-182.
18. R. Hopper, "Ceramic Barrier Performance Model, Version 1.0, Description of Initial PA Input," Memorandum, University of California, Lawrence Livermore National Laboratory, March 30, 1998.
19. P.A. Thornton, V. J. Colangelo, Fundamentals of Engineering Materials, Prentice Hall, Englewood Cliffs, NJ, 07632, 1985.

20. A. K. Roy, D. L. Fleming, B. Y. Lum, "Effect of Environmental Variables on Localized Corrosion of High-Performance Container Materials," UCRL-JC-125329, University of California, Lawrence Livermore National Laboratory, January 1997, 16 p.
21. A. K. Roy, D. L. Fleming, B. Y. Lum, "Localized Corrosion of Container Materials in Anticipated Repository Environments," UCRL-JC-122861, University of California, Lawrence Livermore National Laboratory, May 1996, 10 p.
22. A. K. Roy, D. L. Fleming, B. Y. Lum, "Electrochemical and Metallographic Evaluation of Alloy C-22 and 625," UCRL-ID-127355, University of California, Lawrence Livermore National Laboratory, May 1997, 10 p.
23. A. K. Roy, D. L. Fleming, B. Y. Lum, Unpublished Data, University of California, Lawrence Livermore National Laboratory, 1997.
24. E. L. Crow, F. A. Davis, M. W. Maxfield, Statistics Manual, Dover Publications, Inc., New York, NY, 1960, pp. 147-19.
25. E. Smailos, W. Schwarzkopf, R. Koster, "Corrosion Behaviour of Container Materials for the Disposal of High-Level Wastes in Rock Salt Formations," Nuclear Science and Technology, Commission of the European Communities, DUR 10400, 1986.
26. D. Shoesmith, "Passive Corrosion of the CRM," Electronic Mail, February 13, 1998.
27. G. E. Gdowski, "Survey of Degradation Modes of Four Nickel-Chromium-Molybdenum Alloys," UCRL-ID-108330, University of California, Lawrence Livermore National Laboratory, March 1991, 67 p.
28. J. S. Newman, Electrochemical Systems, 2nd Ed., Prentice Hall, Englewood Cliffs, NJ, 1991.
29. V. G. Jenson, G. V. Jeffreys, Mathematical Methods in Chemical Engineering, Academic Press, New York, NY, 1963, pp. 410-422.
30. D. D. McCracken, W. S. Dorn, Numerical Methods and Fortran Programming with Applications in Science and Engineering, John Wiley and Sons, New York, NY, 1964, pp. 377-385.
31. P. O. Gartland, "A Simple Model of Crevice Corrosion Propagation for Stainless Steels in Sea Water," Corrosion 97, Paper No. 417, National Association of Corrosion Engineers, Houston, TX, 1997, 17 p.
32. Y. Xu, H. W. Pickering, "The Initial Potential and Current Distributions of the Crevice Corrosion Process," J. Electrochemical Society, Vol. 140, No. 3, 1993, pp. 658-668.

33. E. A. Nystrom, J. B. Lee, A. A. Sagues, H. W. Pickering, "An Approach for Estimating Anodic Current Distributions in Crevice Corrosion from Potential Measurements," J. Electrochemical Society, Vol. 141, No. 2, 1994, pp. 358-361.
34. J. W. Oldfield, W. H. Sutton, "Crevice Corrosion of Stainless Steels: I. A Mathematical Model," British Corrosion Journal, Vol. 13, No. 1, 1978, pp. 13-22.
35. F. A. Cotton, G. Wilkinson, Advanced Inorganic Chemistry, 5th Ed., John Wiley & Sons, New York, NY, 1988, pp. 679-755.
36. F. Y. Saleh, G. E. Mbamalu, Q. H. Jaradat, C. E. Brungardt, "Ion Chromatography: Photodiode Array UV-Visible Detection of Cr(III) Hydrolytic Polymerization Products in Pure and Natural Waters, Analytical Chemistry, Vol. 68, No. 5, March 1, 1996, pp. 740-745.
37. J. C. Walton, G. Cragnoliino, S. K. Kalandros, "A Numerical Model of Crevice Corrosion for Passive and Active Metals," Corrosion Science, Vol. 38, No. 1, 1996, pp. 1-18.
38. H. W. Pickering, R. P. Frankenthal, "On the Mechanism of Localized Corrosion of Iron and Stainless Steel: I. Electrochemical Studies," J. Electrochemical Society, Vol. 119, No. 10, 1972, pp. 1297-1304.
39. J. R. Galvele, "Transport Processes and the Mechanism of Pitting of Metals," J. Electrochemical Society, Vol. 123, No. 4, 1976, pp. 464-474.
40. J. C. Farmer, G. E. Gdowski, R. D. McCright, H. S. Ahluwalia, "Corrosion Models for Performance Assessment of High-Level Radioactive-Waste Containers," Nuclear Engineering Design, Vol. 129, 1991, pp. 57-88.
41. T. Okada, "Halide Nuclei Theory of Pit Initiation in Passive Metals, J. Electrochemical Society, Vol. 131, No. 2, 1984, pp. 241-247.
42. T. Okada, "A Theory of Perturbation-Initiated Pitting, Proceedings of the International Symposium Honoring Professor Marcel Pourbaix on his Eightieth Birthday: Equilibrium Diagrams and Localized Corrosion, R. P. Frankenthal, J. Kruger, Eds., Electrochemical Society, Pennington, NJ, Vol. 84-9, 1984, pp. 402-431.
43. C. Y. Chao, L. F. Lin, D. D. McDonald, "A Point Defect Model for Anodic Passive Films, II. Chemical Breakdown and Pit Initiation," J. Electrochemical Society, Vol. 128, No. 6, 1981, pp. 1194-1198.
44. N. Sato, *Electrochimica Acta*, Vol. 19, 1971, p. 1683.
45. T. Shibata, T. Takeyama, "Stochastic Theory of Pitting Corrosion," Corrosion, Vol. 33, No. 7, 1977, pp. 243-251.

46. T. Shibata, "Statistical and Stochastic Approaches to Localized Corrosion," *Corrosion*, Vol. 52, No. 11, 1996, pp. 813.
47. T. R. Beck, R. C. Alkire, "Occurrence of Salt Films During Initiation and Growth of Corrosion Pits," *J. Electrochemical Society*, Vol. 123, No. 4, 1976, pp. 464-474.
48. G. A. Henshall, "Modeling Pitting Corrosion Damage of High-Level Radioactive-Waste Containers Using a Stochastic Approach," *Journal of Nuclear Materials*, Vol. 195, 1992, pp. 109-125.
49. G. A. Henshall, "Stochastic Modeling of the Influence of Environment on Pitting Corrosion Damage of Radioactive-Waste Containers," *Materials Research Society Symposium*, Vol. 353, 1995, pp. 679-686.
50. G. A. Henshall, "Modeling Pitting Degradation of Corrosion Resistant Alloys," UCRL-ID-125300, University of California, Lawrence Livermore National Laboratory, November 1996, 26 p.
51. H. -H. Strehblow, "Mechanisms of Pitting Corrosion," Chapt. 7, in Corrosion Mechanisms in Theory and Practice, P. Marcus, J. Oudar, Eds., Marcel Dekker, New York, NY, 1995, pp. 201-237.
52. J. R. Scully, "Appendix D, Elicitation Interview Summaries," Waste Package Degradation Expert Elicitation Project Final Report, K. J. Coppersmith, R. C. Perman, M. Pendleton, J. L. Younker, Civilian Radioactive Waste Management System Management and Operating Contractor, Geomatrix Consultants, San Francisco, CA, August 15, 1997, pp. JS 1-30.
53. B. Baroux, "Further Insights on the Pitting Corrosion of Stainless Steels," Chapter 9, *Corrosion Mechanisms in Theory and Practice*, P. Marcus, J. Oudar, Eds., Marcel Dekker, Inc., New York, NY, 1995, pp. 265-309.
54. G. P. Marsh, K. J. Taylor, Z. Sooi, "The Kinetics of Pitting Corrosion of Carbon Steel," SKB Technical Report 88-09, Swedish Nuclear Fuel and Waste Management Company (SKB), Box 5864, S-102 48, Stockholm, 1988, 39 p.
55. P. L. Andresen, "Assessment of Corrosion Rate Properties for the Hastelloy C-22 Inner Barrier, An Environment for Waste Packages, Background Information for Consideration," General Electric Research Center, February 27, 1998, p. 12
56. M. Pourbaix, Atlas of Electrochemical Equilibria in Aqueous Solutions, English Translation by J. A. Franklin, Pergamon Press, New York, NY; Cebecor, Brussels, Belgium, 1966, 644 p.
57. T. L. Anderson, Fracture Mechanics, 2nd Ed., CRC Press Inc., Boca Raton, FL, 1995.

58. Newman, Stress Intensity Factors, D. P. Rooke, D. J. Cartwright, Eds., Her Majesty's Stationary Office, London, UK.
59. Shigley and Mischke, Mechanical Engineering and Design, 5th Ed, McGraw Hill, 1989, p. 62-63.
60. Jia-Song Huang, "Stress Corrosion Cracking in Canistered Waste Package Containers: Weld and Base Metals," UCRL-ID-130063, University of California, Lawrence Livermore National Laboratory, March 12, 1998, 8 p.
61. A.K. Roy, D.L. Fleming, B.Y. Lum, "Stress Corrosion Cracking of Fe-Ni-Cr-Mo, Ni-Cr-Mo, and Ti Alloys in 90°C Acidic Brine, Paper 157, Symposium on Corrosion in Nuclear Systems, 98-T-2A, Annual Meeting of the National Association of Corrosion Engineers (NACE), Corrosion 98, San Diego, CA March 22-27, 1998, 6 p.
62. ASM Specialty Handbook, Carbon and Alloy Steels, J. R. Davis, Ed., ASM International, Materials Park, OH, 1996, p. 349
63. C. J. McMahon, Jr., "Temper Brittleness - An Interpretive Review," Temper Embrittlement in Steel, ASTM STP 407, ASTM, Philadelphia, PA, p. 127-167
64. D. McLean, Grain Boundaries in Metals, Oxford University Press, London, UK, 1957.
65. S. G. Bruce et al., "Effects of Aging on Properties of Pressure Vessel Steels," Acta Metallurgica, Vol. 34, 1986, p. 641-652.
66. Binary Alloy Phase Diagrams, T. B. Massalski, Ed., Vol. 1, American Society for Metals, OH, 1986.
67. J. A. Horn, A. Rivera, T. Lian, "MIC Evaluation and Testing for the Yucca Mountain Repository," Paper 152, Symposium on Corrosion in Nuclear Systems, 98-T-2A, Annual Meeting of the National Association of Corrosion Engineers (NACE), Corrosion 98, San Diego, CA March 22-27, 1998, 14 p.
68. P. Bedrossian, "One-Dimensional Ordering at the Mo/Si Interface," Surface Science, Vol. 320, 1994, p. 247; "Nucleation and Ordering of MoSi₂ on Si(100)," Surface Science, Vol. 322, 1995, p. 73.
69. "Scanning Tunneling Microscopy: Opening a New Era of Materials Engineering," Science and Technology Review, Lawrence Livermore National Laboratory, August, 1995, pp. 4-11.
70. J. Golovchenko, "The Tunneling Microscope: A New Look at the Atomic World," Science, Vol. 232, 1986, p. 48.

TABLES

Table 1. Conditions in the Long-Term Corrosion Test Facility at LLNL

Media	Temp.	pH	Ca ²⁺	Mg ²⁺	K ⁺	Na ⁺	Si	SO ₄ ²⁻	Cl ⁻	NO ₃ ⁻	F ⁻	HCO ₃ ⁻	Equiv. NaCl
	°C		ppm	ppm	ppm	ppm	ppm	ppm	Ppm	ppm	ppm	ppm	ppm
SDW	60	9.5	3.5	1.2	36	430	17	170	68	62	14	720	112
SDW	90	9.9	3.4	ND	38	460	16	180	74	64	15	700	122
SCW	60	9.2	16	29	4600	36000	18	13000	7400	7000	330	44000	12199
SCW	90	9.2	15	3.4	4500	44000	58	13000	7500	7200	1400	51000	12363
SAW	60	2.7	58	52	4300	43000	30	41000	28000	23000	0	0	46157
SAW	90	2.7	58	53	4300	43000	50	40000	27000	24000	0	0	44508
SCMW	60	7.8	400	4	85	10	10	1200	11	10	< 0.1	< 1	18

SDW: Simulated Dilute Water (10X J-13)

SCW: Simulated Concentrated Water (1000X J-13)

SAW: Simulated Acidified Water

SCMW: Simulated Cement-Modified Water

Table 2. Summary of Regression Analysis of Data for Alloy 516

Coefs.	Case 1	Case 2	Case 3	Case 4	Case 5	Case 6
	All data	VP-WLS	AP-WLS	VP-CS	AP-CS	WL-CS
b ₀	290.25	-10.035	-47.709	-2.4360	-58.993	-91.805
b ₁	3.7598	-0.46570	6.1826	-0.49354	7.8535	10.720
b ₂	2.8092	1.5795	3.5555	0.83926	4.2052	6.8424
b ₃	1.0682	1.8258	0.50585	1.2022	0.69899	1.6603
b ₄	-324.34					
b ₅	-323.50					
s _{y/123...k}	0.62425	0.071465	0.039343	0.057914	0.55798	0.031678
r _{y/123...k}	0.31931	0.90761	0.95062	0.86171	0.94379	0.98847

Note: VP is vapor phase; AP is aqueous phase; WL is water line;
WLS is weight loss sample; and CS is crevice sample.

Table 3. Alloy 516, Vapor Phase, General Corrosion (Case 2)

j	y predicted	y measured	x_1	x_2	x_3
	$\ln(dp/dt)$	$\ln(dp/dt)$	$1000/T$	pH	C_{NaCl}
	$\ln(\mu m\ y^{-1})$	$\ln(\mu m\ y^{-1})$	$K^{-1} \times 10^3$	pH	wt. %
1	3.5918	3.3206	3.0030	9.5	0.01122
2	3.5918	3.0735	3.0030	9.5	0.01122
3	3.5918	3.7363	3.0030	9.5	0.01122
4	3.5918	3.6678	3.0030	9.5	0.01122
5	3.5918	3.6138	3.0030	9.5	0.01122
6	3.5918	4.1361	3.0030	9.5	0.01122
7	4.3409	4.2603	2.7548	9.9	0.01220
8	4.3409	4.0908	2.7548	9.9	0.01220
9	4.3409	4.1575	2.7548	9.9	0.01220
10	4.3409	4.3361	2.7548	9.9	0.01220
11	4.3409	4.5501	2.7548	9.9	0.01220
12	4.3409	4.6533	2.7548	9.9	0.01220
13	5.3247	5.2926	3.0030	9.2	1.2199
14	5.3247	5.5792	3.0030	9.2	1.2199
15	5.3247	5.6870	3.0030	9.2	1.2199
16	5.3247	5.0902	3.0030	9.2	1.2199
17	5.3247	5.0400	3.0030	9.2	1.2199
18	5.3247	5.2625	3.0030	9.2	1.2199
19	5.4704	5.4882	2.7548	9.2	1.2363
20	5.4704	5.7735	2.7548	9.2	1.2363
21	5.4704	5.5528	2.7548	9.2	1.2363
22	5.4704	5.4728	2.7548	9.2	1.2363
23	5.4704	5.2742	2.7548	9.2	1.2363
24	5.4704	5.2576	2.7548	9.2	1.2363

Table 4. Alloy 516, Aqueous Phase, General Corrosion (Case 3)

J	y predicted	y measured	x ₁	x ₂	x ₃
	ln(dp/dt)	ln(dp/dt)	1000/T	pH	C _{NaCl}
	ln(μm y ⁻¹)	ln(μm y ⁻¹)	K ⁻¹ × 10 ³	pH	Wt. %
1	4.6398	4.6152	3.0030	9.5	0.01122
2	4.6398	4.6861	3.0030	9.5	0.01122
3	4.6398	4.6571	3.0030	9.5	0.01122
4	4.6398	4.4790	3.0030	9.5	0.01122
5	4.6398	4.6245	3.0030	9.5	0.01122
6	4.6398	4.7700	3.0030	9.5	0.01122
7	4.5281	4.4932	2.7548	9.9	0.01220
8	4.5281	4.2327	2.7548	9.9	0.01220
9	4.5281	4.4310	2.7548	9.9	0.01220
10	4.5281	4.4733	2.7548	9.9	0.01220
11	4.5281	4.6771	2.7548	9.9	0.01220
12	4.5281	4.8677	2.7548	9.9	0.01220
13	4.1845	3.9999	3.0030	9.2	1.2199
14	4.1845	4.0067	3.0030	9.2	1.2199
15	4.1845	3.9170	3.0030	9.2	1.2199
16	4.1845	4.2281	3.0030	9.2	1.2199
17	4.1845	4.4451	3.0030	9.2	1.2199
18	4.1845	4.5169	3.0030	9.2	1.2199
19	2.6585	2.5505	2.7548	9.2	1.2363
20	2.6585	2.6304	2.7548	9.2	1.2363
21	2.6585	2.3905	2.7548	9.2	1.2363
22	2.6585	2.9485	2.7548	9.2	1.2363
23	2.6585	2.6396	2.7548	9.2	1.2363
24	2.6585	2.7850	2.7548	9.2	1.2363

Table 5. Alloy 516, Vapor Phase, Crevice Corrosion (Case 4)

j	y predicted	y measured	x ₁	x ₂	x ₃
	ln(dp/dt)	ln(dp/dt)	1000/T	pH	C _{NaCl}
	ln(μm y ⁻¹)	ln(μm y ⁻¹)	K ⁻¹ × 10 ³	pH	wt. %
1	4.0684	4.1469	3.0030	9.5	0.01122
2	4.0684	3.9717	3.0030	9.5	0.01122
3	4.0684	3.9004	3.0030	9.5	0.01122
4	4.0684	3.9774	3.0030	9.5	0.01122
5	4.0684	4.1371	3.0030	9.5	0.01122
6	4.0684	4.2759	3.0030	9.5	0.01122
7	4.5278	4.9072	2.7548	9.9	0.01220
8	4.5278	4.8682	2.7548	9.9	0.01220
9	4.5278	4.5015	2.7548	9.9	0.01220
10	4.5278	4.1585	2.7548	9.9	0.01220
11	4.5278	4.1705	2.7548	9.9	0.01220
12	4.5278	4.5618	2.7548	9.9	0.01220
13	5.2696	4.8111	3.0030	9.2	1.2199
14	5.2696	5.1110	3.0030	9.2	1.2199
15	5.2696	5.3542	3.0030	9.2	1.2199
16	5.2696	5.3397	3.0030	9.2	1.2199
17	5.2696	5.4520	3.0030	9.2	1.2199
18	5.2696	5.5509	3.0030	9.2	1.2199
19	5.4119	5.2229	2.7548	9.2	1.2363
20	5.4119	5.4306	2.7548	9.2	1.2363
21	5.4119	5.4295	2.7548	9.2	1.2363
22	5.4119	5.6223	2.7548	9.2	1.2363
23	5.4119	5.1697	2.7548	9.2	1.2363
24	5.4119	5.5952	2.7548	9.2	1.2363

Table 6. Alloy 516, Aqueous Phase, Crevice Corrosion (Case 5)

j	y predicted	y measured	X ₁	x ₂	x ₃
	ln(dp/dt)	ln(dp/dt)	1000/T	pH	C _{NaCl}
	ln(μm y ⁻¹)	ln(μm y ⁻¹)	K ⁻¹ × 10 ³	pH	wt. %
1	4.5482	4.4751	3.0030	9.5	0.01122
2	4.5482	4.4806	3.0030	9.5	0.01122
3	4.5482	4.3657	3.0030	9.5	0.01122
4	4.5482	4.7226	3.0030	9.5	0.01122
5	4.5482	4.6365	3.0030	9.5	0.01122
6	4.5482	4.6025	3.0030	9.5	0.01122
7	4.2818	4.3433	2.7548	9.9	0.01220
8	4.2818	4.2549	2.7548	9.9	0.01220
9	4.2818	4.3080	2.7548	9.9	0.01220
10	4.2818	5.1953	2.7548	9.9	0.01220
11	4.2818	4.0618	2.7548	9.9	0.01220
12	4.2818	4.0618	2.7548	9.9	0.01220
13	4.2818	4.0618	2.7548	9.9	0.01220
14	4.2818	4.0618	2.7548	9.9	0.01220
15	4.2818	4.1937	2.7548	9.9	0.01220
16	4.1314	4.1773	3.0030	9.2	1.2199
17	4.1314	4.1793	3.0030	9.2	1.2199
18	4.1314	4.1434	3.0030	9.2	1.2199
19	4.1314	4.0610	3.0030	9.2	1.2199
20	4.1314	4.0971	3.0030	9.2	1.2199
21	4.1314	4.1354	3.0030	9.2	1.2199
22	2.1938	2.5044	2.7548	9.2	1.2363
23	2.1938	2.0852	2.7548	9.2	1.2363
24	2.1938	2.1587	2.7548	9.2	1.2363
25	2.1938	2.0001	2.7548	9.2	1.2363
26	2.1938	2.2103	2.7548	9.2	1.2363
27	2.1938	2.1995	2.7548	9.2	1.2363

Table 7. Alloy 516, Water Line, General Corrosion (Case 6)

j	y predicted	y measured	x ₁	x ₂	x ₃
	ln(dp/dt)	ln(dp/dt)	1000/T	pH	C _{NaCl}
	ln(μm y ⁻¹)	ln(μm y ⁻¹)	K ⁻¹ × 10 ³	pH	wt. %
1	5.4101	5.3912	3.0030	9.5	0.01122
2	5.4101	5.4296	3.0030	9.5	0.01122
3	5.4881	5.3679	2.7548	9.9	0.01220
4	5.4881	5.6077	2.7548	9.9	0.01220
5	5.3642	5.2877	3.0030	9.2	1.2199
6	5.3642	5.4398	3.0030	9.2	1.2199
7	2.7309	2.9382	2.7548	9.2	1.2363
8	2.7309	2.5243	2.7548	9.2	1.2363

Table 8. Mechanical Properties of Ceramic Coatings

Property	Elastic Modulus (E)	Elastic Modulus (E)	Fracture Strength (σ^*)	Fracture Strength (σ^*)
Units	MPa	Mpsi	Mpa	Ksi
Al ₂ O ₃	365,000	53	172	25
ZrO ₂	144,900	21	55	8

Table 9. Extension of WP Life with Ceramic Coating

	Life with Ceramic Coating (y)	Life without Ceramic Coating (y)
Thermal Pulse	~ 1000	~ 1000 y
Ceramic Barrier	> 14,037	~ 0
CAM - After Exfoliation	> 333	> 333

Table 10. Passive Corrosion Rate Data for Alloy C-22 - Basis of Regression - LTCTF

	Comments	Exposure	dp/dt	Temp.	PH	NaCl	FeCl ₃	Air
		hours	$\mu\text{m y}^{-1}$	°C	None	wt. %	wt. %	Sat.
1	Long Term Test - SAW	4296	2.53×10^{-2}	60	2.7	4.616	0	1
2	Long Term Test - SAW	4296	5.07×10^{-2}	60	2.7	4.616	0	1
3	Long Term Test - SAW	4296	1.13×10^{-1}	60	2.7	4.616	0	1
4	Long Term Test - SAW	4296	1.64×10^{-1}	60	2.7	4.616	0	1
5	Long Term Test - SAW	4296	6.03×10^{-2}	60	2.7	4.616	0	1
6	Long Term Test - SAW	4296	3.45×10^{-2}	60	2.7	4.616	0	1
7	Long Term Test - SAW	4296	3.47×10^{-2}	60	2.7	4.616	0	1
15	Long Term Test - SAW	4296	8.58×10^{-2}	60	2.7	4.616	0	1
16	Long Term Test - SAW	4296	1.13×10^{-1}	60	2.7	4.616	0	1
17	Long Term Test - SAW	4296	7.70×10^{-2}	60	2.7	4.616	0	1
18	Long Term Test - SAW	4296	2.81×10^{-2}	60	2.7	4.616	0	1
19	Long Term Test - SAW	4296	1.87×10^{-2}	60	2.7	4.616	0	1
20	Long Term Test - SAW	4296	9.31×10^{-3}	60	2.7	4.616	0	1
21	Long Term Test - SAW	4296	1.04×10^{-1}	60	2.7	4.616	0	1
22	Long Term Test - SAW	4296	8.11×10^{-2}	60	2.7	4.616	0	1
23	Long Term Test - SAW	4296	1.17×10^{-1}	60	2.7	4.616	0	1
24	Long Term Test - SAW	4296	6.56×10^{-2}	60	2.7	4.616	0	1
25	Long Term Test - SAW	4296	6.61×10^{-2}	60	2.7	4.616	0	1
26	Long Term Test - SAW	4296	4.71×10^{-2}	60	2.7	4.616	0	1
27	Long Term Test - SAW	4344	2.45×10^{-1}	90	2.7	4.616	0	1
28	Long Term Test - SAW	4344	7.31×10^{-1}	90	2.7	4.616	0	1
29	Long Term Test - SAW	4344	1.76×10^{-1}	90	2.7	4.616	0	1
30	Long Term Test - SAW	4344	4.16×10^{-2}	90	2.7	4.616	0	1
31	Long Term Test - SAW	4344	1.07×10^{-1}	90	2.7	4.616	0	1

Table 11. Passive Corrosion Rate Data for Alloy C-22 - Basis of Regression - LTCTF

	Comments	Exposure	dp/dt	Temp.	PH	NaCl	FeCl ₃	Air
		hours	$\mu\text{m y}^{-1}$	$^{\circ}\text{C}$	None	wt. %	wt. %	Sat.
8	Cyclic Polarization - NaCl	~1	3.00×10^{-4}	60	2.69	1	0	1
9	Cyclic Polarization - NaCl	~1	3.00×10^{-3}	60	6.53	5	0	1
10	Cyclic Polarization - NaCl	~1	2.01×10^{-2}	90	6.53	5	0	1
11	Cyclic Polarization - NaCl	~1	3.02×10^{-2}	90	6.83	10	0	1
12	Cyclic Polarization - NaCl	~1	2.01×10^{-1}	90	2.69	1	0	0
13	Cyclic Polarization - NaCl	~1	2.01×10^{-1}	90	2.67	1	0	0
14	Cyclic Polarization - NaCl	~1	2.01×10^{-1}	90	2.69	5	0	0
32	Cyclic Polarization - FeCl ₃	~1	3.00×10^{-3}	90	2.14	0	0.61	0
33	Cyclic Polarization - FeCl ₃	~1	6.00×10^{-3}	90	2.16	0	0.61	0
34	Cyclic Polarization - FeCl ₃	~1	2.01×10^{-1}	90	1.72	0	3.05	0
35	Cyclic Polarization - FeCl ₃	~1	2.01	90	1.72	0	3.05	0
36	Haynes - FeCl ₃	100	2.50	25	0.7	0	10	1
37	Haynes - FeCl ₃	100	2.50	50	0.7	0	10	1
38	Haynes - FeCl ₃	100	12.7	75	0.7	0	10	1

Table 12. Data for Passive Corrosion of Alloy C-4 in Saturated Brines (Smailos et al.; Shoesmith).

Brine	pH	NaCl	KCl	MgCl ₂	MgSO ₄	H ₂ O	90°C Rate	170°C Rate	pH
		wt. %	wt. %	wt. %	wt. %	wt. %	$\mu\text{m y}^{-1}$	$\mu\text{m y}^{-1}$	Shoesmith
Q	4.9	1.4	4.7	26.8	1.4	65.7	0.02	0.15-0.66	~5
Z	3.6	0.2	0.66	36.4	0.87	61.9	10-14		~2

Table 13. Estimates of CDF's for Passive Corrosion Rates of Alloy C-22 with Dripping.

Data Source		Regression (Farmer)	Regression (Farmer)	Regression (Farmer)	Smailos (Shoesmith)	Smailos (Shoesmith)	Smailos (Shoesmith)	Smailos (Shoesmith)
Environment		1000X J-13	1000X J-13	1000X J-13	Z-Brine	Z-Brine	Z-Brine	Z-Brine
NaCl (wt. %)		1.2	1.2	1.2	Saturated	Saturated	Saturated	Saturated
T (°C)		25	50	100	90	25	50	100
Percentile (%)	pH	$\mu\text{m y}^{-1}$	$\mu\text{m y}^{-1}$	$\mu\text{m y}^{-1}$	$\mu\text{m y}^{-1}$	$\mu\text{m y}^{-1}$	$\mu\text{m y}^{-1}$	$\mu\text{m y}^{-1}$
50	1	4.36×10^{-3}	1.85×10^{-2}	1.86×10^{-1}	6.60×10^{-1}	1.71×10^{-2}	8.29×10^{-2}	1.03
50	2	1.82×10^{-3}	7.71×10^{-3}	7.74×10^{-2}	2.75×10^{-1}	7.13×10^{-3}	3.46×10^{-2}	4.31×10^{-1}
50	3	7.59×10^{-4}	3.22×10^{-3}	3.23×10^{-2}	1.15×10^{-1}	2.98×10^{-3}	1.44×10^{-2}	1.80×10^{-1}
50	5	1.32×10^{-4}	5.60×10^{-4}	5.62×10^{-3}	2.00×10^{-2}	5.18×10^{-4}	2.51×10^{-3}	3.13×10^{-2}
50	7	2.30×10^{-5}	9.75×10^{-5}	9.79×10^{-4}	3.48×10^{-3}	9.02×10^{-5}	4.38×10^{-4}	5.46×10^{-3}
50	10	1.67×10^{-6}	7.08×10^{-6}	7.11×10^{-5}	2.53×10^{-4}	6.55×10^{-6}	3.18×10^{-5}	3.96×10^{-4}
5	1	3.35×10^{-4}	1.42×10^{-3}	1.43×10^{-2}	4.57×10^{-2}	1.18×10^{-3}	5.75×10^{-3}	7.16×10^{-2}
5	2	1.40×10^{-4}	5.93×10^{-4}	5.95×10^{-3}	1.91×10^{-2}	4.94×10^{-4}	2.40×10^{-3}	2.99×10^{-2}
5	3	5.84×10^{-5}	2.47×10^{-4}	2.48×10^{-3}	7.96×10^{-3}	2.06×10^{-4}	1.00×10^{-3}	1.25×10^{-2}
5	5	1.02×10^{-5}	4.31×10^{-5}	4.32×10^{-4}	1.39×10^{-3}	3.59×10^{-5}	1.74×10^{-4}	2.17×10^{-3}
5	7	1.77×10^{-6}	7.49×10^{-6}	7.53×10^{-5}	2.41×10^{-4}	6.25×10^{-6}	3.03×10^{-5}	3.78×10^{-4}
5	10	1.29×10^{-7}	5.44×10^{-7}	5.47×10^{-6}	1.75×10^{-5}	4.54×10^{-7}	2.20×10^{-6}	2.75×10^{-5}
95	1	5.67×10^{-2}	2.40×10^{-1}	2.41	9.52	2.47×10^{-1}	1.20	14.9
95	2	2.37×10^{-2}	1.00×10^{-1}	1.01	3.97	1.03×10^{-1}	4.99×10^{-1}	6.23
95	3	9.88×10^{-3}	4.19×10^{-2}	4.20×10^{-1}	1.66	4.30×10^{-2}	2.08×10^{-1}	2.60
95	5	1.72×10^{-3}	7.29×10^{-3}	7.32×10^{-2}	2.89×10^{-1}	7.48×10^{-3}	3.63×10^{-2}	4.52×10^{-1}
95	7	2.99×10^{-4}	1.27×10^{-3}	1.27×10^{-2}	5.03×10^{-2}	1.30×10^{-3}	6.31×10^{-3}	7.87×10^{-2}
95	10	2.17×10^{-5}	9.21×10^{-5}	9.25×10^{-4}	3.65×10^{-3}	9.46×10^{-5}	4.59×10^{-4}	5.72×10^{-3}
1	1	1.06×10^{-4}	4.51×10^{-4}	4.53×10^{-3}	1.51×10^{-2}	3.92×10^{-4}	1.90×10^{-3}	2.37×10^{-2}
1	2	4.44×10^{-5}	1.88×10^{-4}	1.89×10^{-3}	6.32×10^{-3}	1.64×10^{-4}	7.94×10^{-4}	9.90×10^{-3}
1	3	1.85×10^{-5}	7.85×10^{-5}	7.89×10^{-4}	2.64×10^{-3}	6.83×10^{-5}	3.31×10^{-4}	4.13×10^{-3}
1	5	3.23×10^{-6}	1.37×10^{-5}	1.37×10^{-4}	4.59×10^{-4}	1.19×10^{-5}	5.77×10^{-5}	7.19×10^{-4}
1	7	5.62×10^{-7}	2.38×10^{-6}	2.39×10^{-5}	7.99×10^{-5}	2.07×10^{-6}	1.00×10^{-5}	1.25×10^{-4}
1	10	4.08×10^{-8}	1.73×10^{-7}	1.74×10^{-6}	5.80×10^{-6}	1.50×10^{-7}	7.29×10^{-7}	9.09×10^{-6}
99	1	1.79×10^{-1}	7.57×10^{-1}	7.60	28.8	7.45×10^{-1}	3.61	45.1
99	2	7.45×10^{-2}	3.16×10^{-1}	3.17	12.0	3.11×10^{-1}	1.51	18.8
99	3	3.11×10^{-2}	1.32×10^{-1}	1.32	5.01	1.30×10^{-1}	6.29×10^{-1}	7.84
99	5	5.41×10^{-3}	2.29×10^{-2}	2.30×10^{-1}	8.72×10^{-1}	2.26×10^{-2}	1.10×10^{-1}	1.37
99	7	9.43×10^{-4}	3.99×10^{-3}	4.01×10^{-2}	1.52×10^{-1}	3.93×10^{-3}	1.91×10^{-2}	2.38×10^{-1}
99	10	6.85×10^{-5}	2.90×10^{-4}	2.91×10^{-3}	1.10×10^{-2}	2.86×10^{-4}	1.39×10^{-3}	1.73×10^{-2}

Table 14. Measured pH of Metal Salt Solutions at 25°C (Denny Jones)

Salt	1 N	3 N	Sat'd.
FeCl ₂	2.1	0.8	0.2
NiCl ₂	3.0	2.7	2.7
CrCl ₃	1.1	-0.3	-1.4

Table 15. Measured pH of FeCl₃ Solutions at 25°C (Francis Wang)

Conc. (wt. %)	pH
1	1.92
2	1.83
3	1.71
4	1.63
10	0.70

Table 16. Transport Limited pH in Crevice (Kevin McCoy & Joe Farmer)

Source of Information	pH
EEP (Expected for WP)	2.5
Transport Model (Alloy 625)	2.8 to 3.2
Artificial Crevices (Carbon Steel)	3.3-4.7
Artificial Crevices (Fe-Cr Alloys)	2.4-4.0
Artificial Crevices (Stainless Steels)	≤ 2.3

Table 17. K_{ij} for i-th Species and j-th Reaction at 25 °C

Species	i	Ref.	K _{i,1}	K _{i,2}	K _{i,3}	K _{i,4}	K _{i,5}	K _{i,6}
Cr(III)	1	34,36	1.58x10 ⁻⁴	6.31x10 ⁻⁷	4.0x10 ⁻³⁸	2.00x10 ³	3.16x10 ⁴	3.16x10 ³
Cr(VI)	2	36	6.92x10 ⁻¹¹					
Fe(II)	3	34	5.0x10 ⁻⁹		7.9x10 ⁻¹⁶			
Fe(III)	4	35	1.84x10 ⁻³	unknown	unknown			
Ni(II)	5	34	3.16x10 ⁻⁴		1.35x10 ⁻¹⁵			

Table 18. Parameter Values Used in Probabilistic Pitting Model

Parameter	Units	Assumed Value
λ ₀	min ⁻¹	6.7572 x 10 ⁻²
α _λ	none	0.5
E _{crit}	mV vs. SCE	+86
μ ₀	min ⁻¹	2.2137 x 10 ¹²
α _μ	none	0.5
E _{pass}	mV vs. SCE	+1
γ ₀	min ⁻¹	5.0 x 10 ²
A _γ	J mole ⁻¹	3.0 x 10 ⁴
τ ₀	min	1.0
A _τ	J mole ⁻¹	3.0 x 10 ⁴
A	none	9.0
B	none	3.0
N	none	1.0
K ₀	cm ² L mole ⁻¹ sec ⁻¹ V ⁻¹	4.4106 540 x 10 ⁻⁴

Table 19. Expected Electrochemical Potentials in Repository –
Based on Measurements of A516 Gr 12 (CAM) and Alloy C-22 (CRM)

Case	A	B	C	D	E
T (°C)	90	90	90	90	90
NaCl (wt. %)	10	1	0	0	5
FeCl ₃ (wt. %)	0	0	0.6	3.1	0
pH	6.8	2.7	2.14	1.72	2.7
Radiolysis	No	No	No	No	No
Deaerated	No	Yes	Yes	Yes	No
E _{corr} (mV vs. SHE): A516 Gr 55					-520
E _{corr} (mV vs. SHE): C-22	-24	-29	+661	+714	
E _{pit} (mV vs. SHE): C-22	+442	+758	+905	+889	> +730
E _{pass} (mV vs. SHE): C-22	+550	+793	+857	+896	> +730
Above Threshold Potential	No	No	No	No	No

Table 20. Potentiostatic Polarization of Alloy C-22 in Acidic Salt Solutions at LLNL (Ajit Roy)

T	NaCl	FeCl ₃	pH	E _{corr}	E _{cont}	Duration	Observation	ID #
°C	wt. %	wt. %		mV vs. Ag/AgCl	mV vs. E _{corr}	hours		
30	5	0	2.6-2.7	-31	681	167	No Attack	062797C1.PS
30	5	0	2.6-2.7	177	423	167	No Attack	041497C1.PS
30	5	0	2.6-2.7	155	545	167	No Attack	041497C2.PS
60	5	0	2.6-2.7	-147	847	167	Slight Crevice	042197C2.PS
90	5	0	2.6-2.7	247	600	26.5	No Attack	112097C1.PS
90	0	3.05	1.68	447	880	167	Slight Crevice	110697C1.PS

Table 21. Pit Stifling Criterion Based on Flux of Dissolved Oxygen at 25°C

NaCl (wt. %)	O ₂ (ppm)	O ₂ (mol/cm ³)	Δx (cm)
0	8.2	2.56x10 ⁻⁷	0.25
3.5	6.8	2.13x10 ⁻⁷	0.20
5	6.0	1.88x10 ⁻⁷	0.18
16	2.9	9.06x10 ⁻⁸	0.09
Satd.	< 2.0	< 6.25x10 ⁻⁸	< 0.06

Table 22: Alloy Composition Assumed for Congruent Dissolution of Alloy C-22 –
Required by Modified Pit Stifling Criterion.

Component	wt. fract.	MW	mol/gram	mol fract. (f _i)
Fe	0.04	55.847	0.000716243	0.043879444
Co	0.02	58.9332	0.000339367	0.020790788
Cr	0.21	51.996	0.004038772	0.24742885
W	0.03	183.85	0.000163177	0.009996745
Mo	0.13	95.94	0.001355014	0.083012714
Ni	0.57	58.7	0.009710392	0.594891456
Total	1			1

Table 23. Solubilities Given by Pourbaix for Various Compounds Responsible for Passivation of Alloy C-22

Film Species	$\log(C_{i,1})$	pH_1	$\log(C_{i,2})$	pH_2	m_i	b_i	Ref.
$\text{Fe}(\text{OH})_2$	-2.5	8	-6.5	10	-2	13.5	Pourbaix p. 311
$\text{Fe}(\text{OH})_3$	-1	2	-3	3	-2.00	3.00	Pourbaix p. 311
Fe_2O_3	-1	0	-8	2.5	-2.80	-1.00	Pourbaix p. 311
$\text{Ni}(\text{OH})_2$	-1	6.5	-8	10	-2.00	12.00	Pourbaix p. 336
$\text{Cr}(\text{OH})_3$	-3	2.5	-12	5.7	-2.81	4.03	Pourbaix p. 268
Cr_2O_3	-3	3.7	-9.5	6	-2.83	7.46	Pourbaix p. 268
$\text{Cr}(\text{OH})_3 \cdot n\text{H}_2\text{O}$	0	4	-4	6	-2.00	8.00	Pourbaix p. 268
MoO_3	-3.7	0	1	4.7	1.00	-3.70	Pourbaix p. 276
WO_3	-8	3	0	7	2.00	-14.00	Pourbaix p. 283

Table 24. Predicted Logarithms of Solubilities at Various pH Values – Based on Slopes and Intercepts in Table 14

PH	$\text{Fe}(\text{OH})_2$	$\text{Fe}(\text{OH})_3$	Fe_2O_3	$\text{Ni}(\text{OH})_2$	$\text{Cr}(\text{OH})_3$	Cr_2O_3	$\text{Cr}(\text{OH})_3 \cdot n\text{H}_2\text{O}$	MoO_3	WO_3
-1	15.50	5.00	1.80	14.00	6.84	10.29	10.00	-4.70	-16.00
0	13.50	3.00	-1.00	12.00	4.03	7.46	8.00	-3.70	-14.00
1	11.50	1.00	-3.80	10.00	1.22	4.63	6.00	-2.70	-12.00
2	9.50	-1.00	-6.60	8.00	-1.59	1.80	4.00	-1.70	-10.00
3	7.50	-3.00	-9.40	6.00	-4.40	-1.03	2.00	-0.70	-8.00
4	5.50	-5.00	-12.20	4.00	-7.21	-3.86	0.00	0.30	-6.00
5	3.50	-7.00	-15.00	2.00	-10.02	-6.69	-2.00	1.30	-4.00
6	1.50	-9.00	-17.80	0.00	-12.83	-9.52	-4.00	2.30	-2.00
7	-0.50	-11.00	-20.60	-2.00	-15.64	-12.35	-6.00	3.30	0.00
8	-2.50	-13.00	-23.40	-4.00	-18.45	-15.18	-8.00	4.30	2.00
9	-4.50	-15.00	-26.20	-6.00	-21.26	-18.01	-10.00	5.30	4.00
10	-6.50	-17.00	-29.00	-8.00	-24.07	-20.84	-12.00	6.30	6.00

Table 25. Maximum Possible Pit Depths ($\Delta x/\text{cm}$) in Alloy C-22 Predicted with Modified Stifling Criterion –Assuming $\Delta C \sim 100\% C_{\text{sat}}$ & $i_{\text{pass}} \sim 4 \mu\text{A cm}^{-2}$

PH	$\text{Fe}(\text{OH})_2$	$\text{Fe}(\text{OH})_3$	Fe_2O_3	$\text{Ni}(\text{OH})_2$	$\text{Cr}(\text{OH})_3$	Cr_2O_3	$\text{Cr}(\text{OH})_3 \cdot n\text{H}_2\text{O}$	MoO_3	WO_3
-1	3.48×10^{19}	1.65×10^9	1.04×10^6	8.11×10^{16}	2.02×10^{10}	5.70×10^{13}	2.92×10^{13}	3.48×10^{-1}	1.45×10^{-11}
0	3.48×10^{17}	1.65×10^7	1.65×10^5	8.11×10^{14}	3.13×10^7	8.43×10^{10}	2.92×10^{11}	3.48	1.45×10^{-9}
1	3.48×10^{15}	1.65×10^5	2.61	8.11×10^{12}	4.85×10^4	1.25×10^8	2.92×10^9	3.48×10^1	1.45×10^{-7}
2	3.48×10^{13}	1.65×10^3	4.14×10^{-3}	8.11×10^{10}	7.52×10^1	1.85×10^5	2.92×10^7	3.48×10^2	1.45×10^{-5}
3	3.48×10^{11}	1.65×10^1	6.57×10^{-5}	8.11×10^8	1.16×10^{-1}	2.73×10^2	2.92×10^5	3.48×10^5	1.45×10^{-3}
4	3.48×10^9	1.65×10^{-1}	1.04×10^{-8}	8.11×10^6	1.80×10^{-4}	4.04×10^{-1}	2.92×10^3	3.48×10^4	1.45×10^{-1}
5	3.48×10^7	1.65×10^{-3}	1.65×10^{-11}	8.11×10^4	2.79×10^{-7}	5.97×10^{-4}	2.92×10^1	3.48×10^5	1.45×10^1
6	3.48×10^5	1.65×10^{-5}	2.61×10^{-14}	8.11×10^2	4.33×10^{-10}	8.83×10^{-7}	2.92×10^{-1}	3.48×10^6	1.45×10^3
7	3.48×10^3	1.65×10^{-7}	4.14×10^{-17}	8.11	6.70×10^{-13}	1.31×10^{-9}	2.92×10^{-3}	3.48×10^7	1.45×10^5
8	3.48×10^1	1.65×10^{-9}	6.57×10^{-20}	8.11×10^{-2}	1.04×10^{-15}	1.93×10^{-12}	2.92×10^{-5}	3.48×10^8	1.45×10^7
9	3.48×10^{-1}	1.65×10^{-11}	1.04×10^{-22}	8.11×10^{-4}	1.61×10^{-18}	2.86×10^{-15}	2.92×10^{-7}	3.48×10^9	1.45×10^9
10	3.48×10^{-3}	1.65×10^{-13}	1.65×10^{-25}	8.11×10^{-6}	2.49×10^{-21}	4.23×10^{-18}	2.92×10^{-9}	3.48×10^{10}	1.45×10^{11}

Notes: (1) Ranges of pH where localized corrosion is stifled by a particular film-forming compound are in bold-face type. (2) At low pH, MoO_3 and WO_3 appear to be primarily responsible for the superior corrosion performance of Alloy C-22. (3) Localized corrosion should be stifled over the entire range of pH, extending from -1 to 10. (4) This is consistent with observations in relevant (anticipated) acidic media. (5) Soluble oxychlorides have not been included in initial calculation, but will be included in future.

Table 26. Three Contributions to Stress in Unperturbed Waste Package

Quantity	Weight Stress	Shrink-Fit Stress	Maximum Residual Weld Stress	Maximum Total Stress
Units	MPa	MPa	MPa	MPa
A516 Gr 55	0.46	40	205	245
Alloy C-22	2.6	0	407	409.6
Alloy 625	2.6	0	483	485.6

Table 27. Measured Values of K_{ISCC} (Ajit Roy)

Material	K_{ISCC} (MPa m ^{1/2})
A516 Gr 55	~71
Alloy 625	~33
Alloy C-22	~30

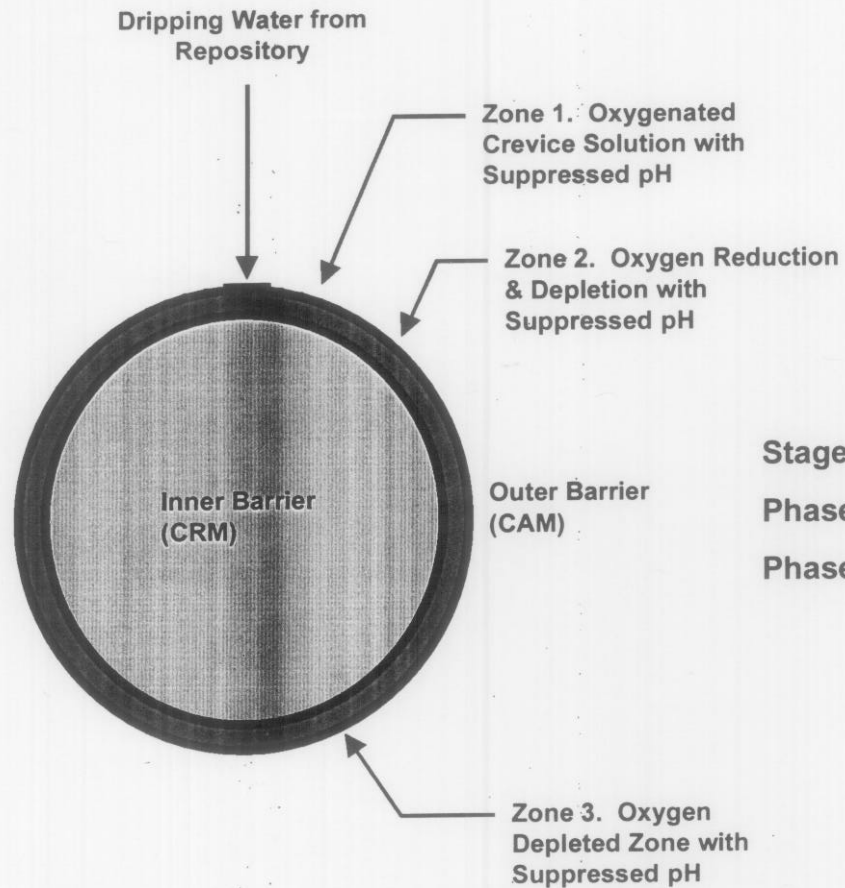
Table 28. Critical Flaw Size Required to Initiate Stress Corrosion Cracking

	a/2c = 0.25	a/2c = 0.5	a/2c = 1	a/2c = 2	a/2c = 5
A516 Gr 55 (t = 100 mm)					
245 MPa	> t	> t	> t	> t	> t
153.8 MPa	> t	> t	> t	> t	> t
102.5 MPa	> t	> t	> t	> t	> t
Alloy 625 (t = 20 mm)					
485.6 MPa	> t	> t	> t	> t	12 mm
362.3 MPa	> t	> t	> t	> t	> t
241.5 MPa	> t	> t	> t	> t	> t
Alloy C-22 (t = 20 mm)					
409.6 MPa	> t	> t	> t	> t	14 mm
305.3 MPa	> t	> t	> t	> t	> t
203.5 MPa	> t	> t	> t	> t	> t

Note: values greater than the wall thickness (t) will not lead to SCC.

Table 29. Predicted Segregation of Phosphorous at Grain Boundaries of Carbon Steel

Temperature (°C)	Time (days)	Segregation of P
Typical Thermal Embrittlement Cycle in Steels		
575	0.04	0.84
538	0.08	0.88
524	0.5	0.89
496	2	0.91
468	3	0.93
350	5	0.97
Expected Waste Package Temperature Cycle		
200	1825	0.005
180	36500	0.011
140	365000	0.012
80	3650000	0.012



Stages of crevice corrosion:

Phase 1 - anodic dissolution of CAM

Phase 2 - attack of CRM after consumption of CAM

Figure 1. Conceptual representation of corrosive attack of horizontal high-level waste container with outer barrier made of corrosion allowance material (CAM) and inner wall made of corrosion resistant material (CRM).

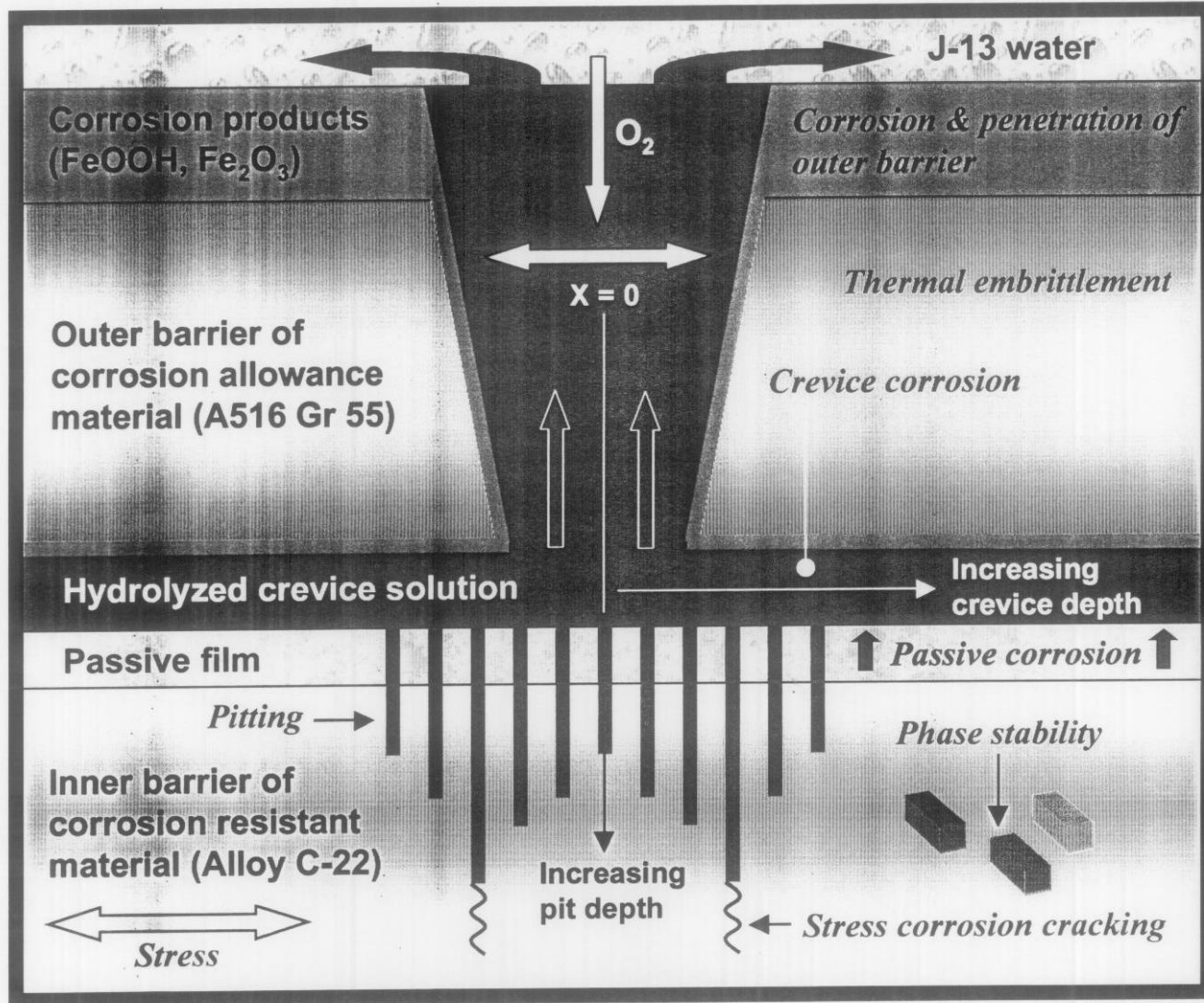


Figure 2. Conceptual representation of interactive modes of corrosion and degradation in CAM-CRM crevice.

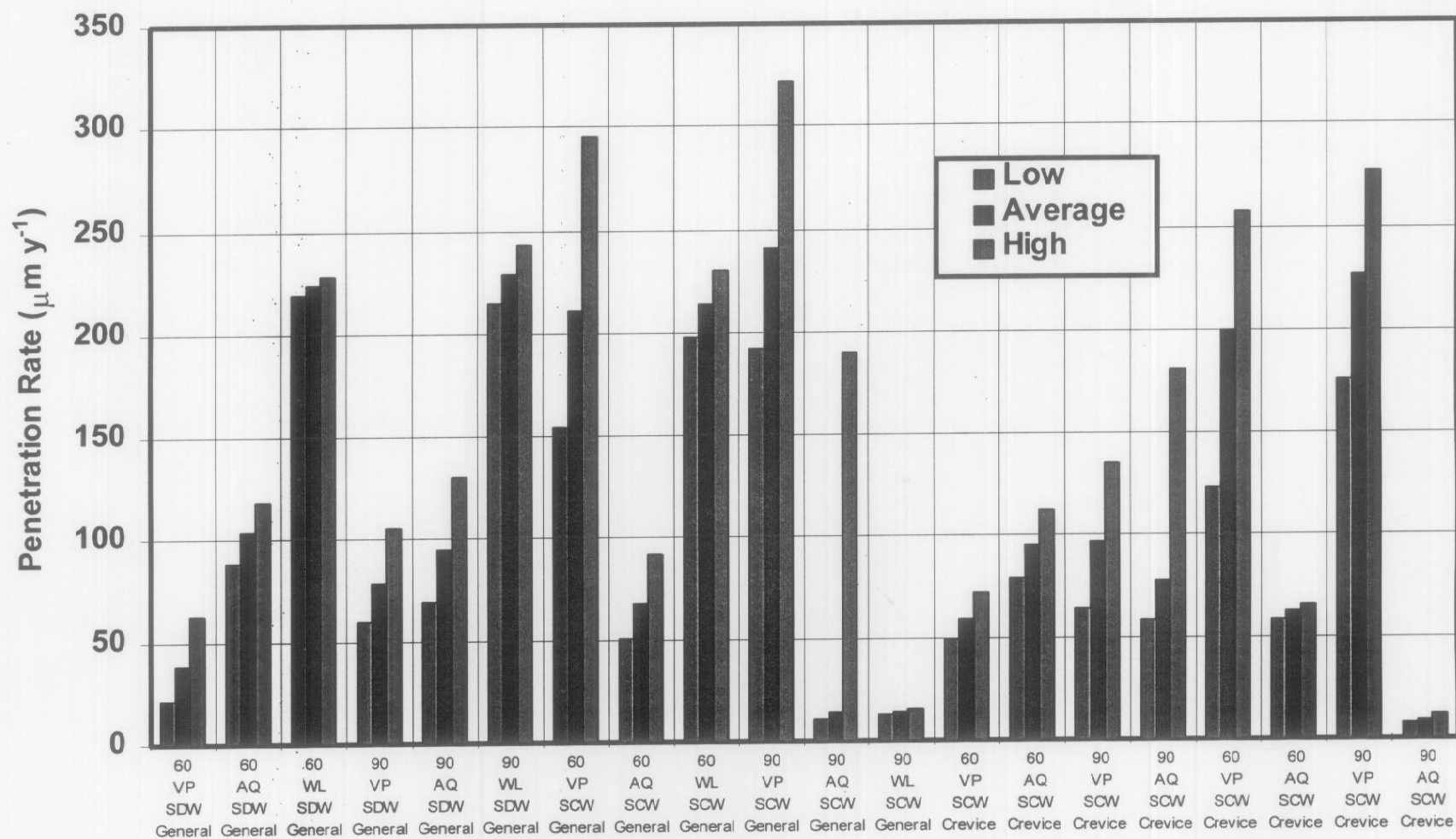


Figure 3. General corrosion (penetration) rates of A516 Gr 55 after 6 months of exposure in the Long Term Corrosion Test Facility at LLNL. Data are for tests with simulated dilute water (SDW), simulated concentrated water (SCW), and simulated acidified water (SAW). Samples were placed in the aqueous phase (AQ), the vapor phase (VP), and at the water line (WL). The maximum observed rate was about 300 microns per year.

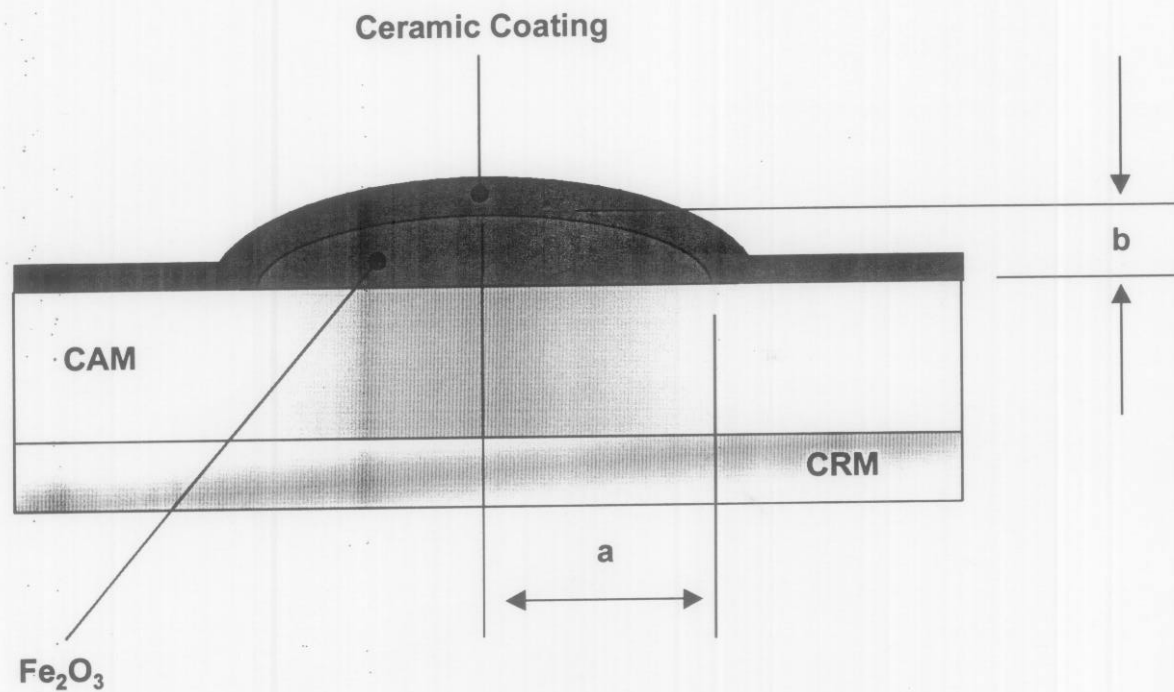


Figure 4. Conceptual representation of degradation-mode model for ceramic coating. In this case, it is assumed that a blister is formed with the geometry of an oblate spheroid.

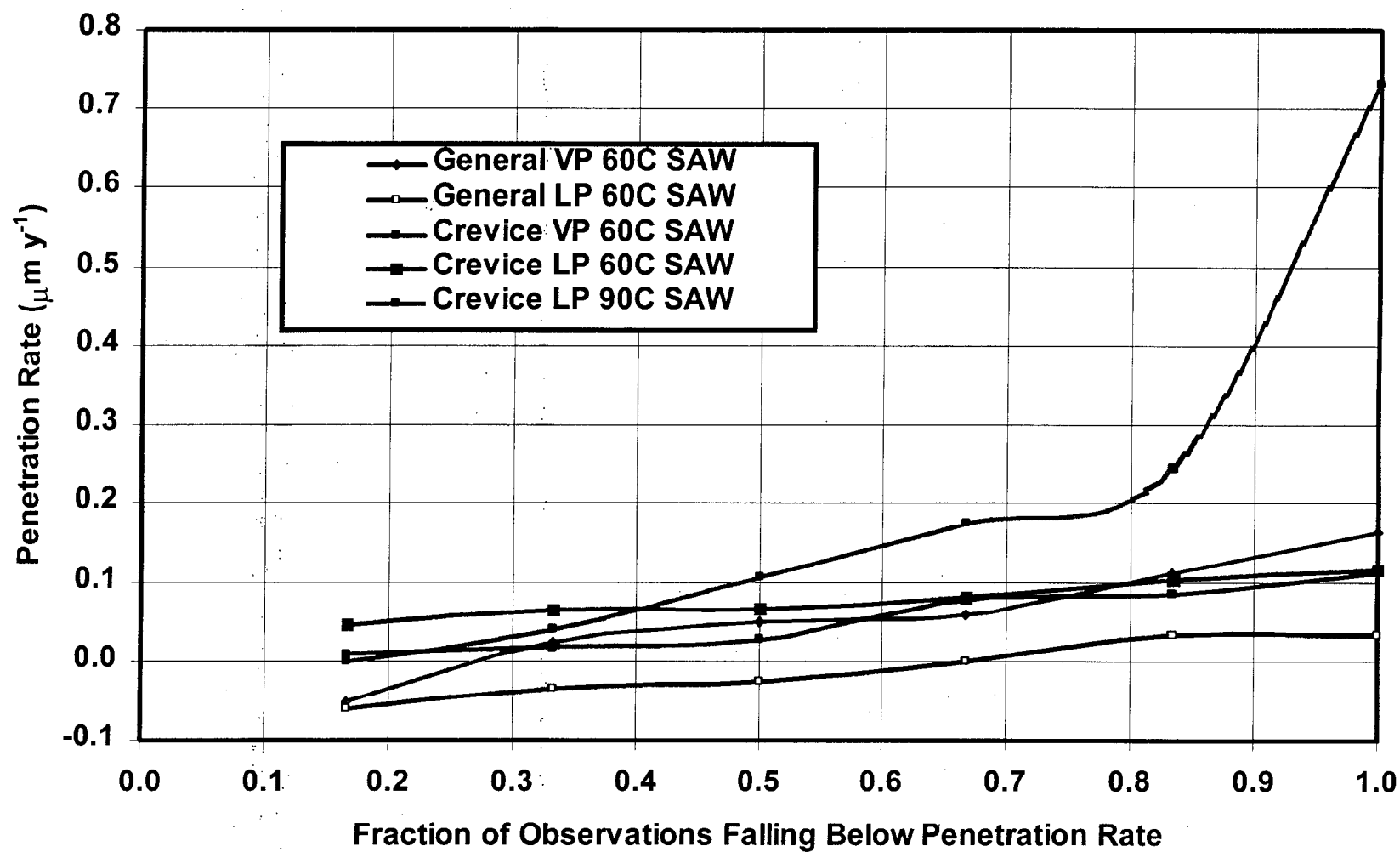


Figure 5a. Passive corrosion (penetration) rates of Alloy C-22 after 6 months of exposure in the Long Term Corrosion Test Facility at LLNL. These data are for simulated acidified water (SAW). Samples were placed in the aqueous phase (AQ), the vapor phase (VP), and at the water line (WL). Rates were below 1 micron per year.

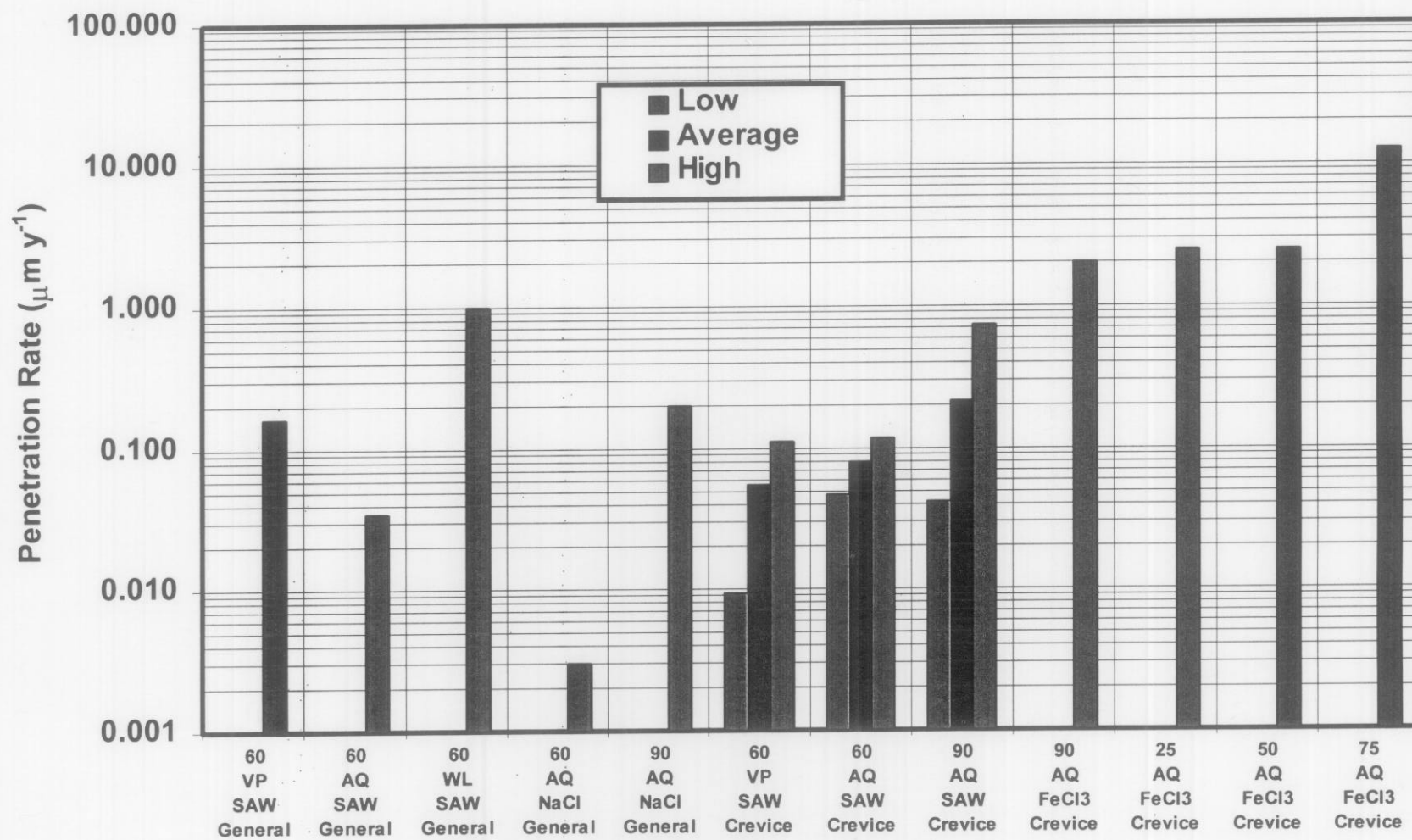


Figure 5b. Passive corrosion (penetration) rates of Alloy C-22 after 6 months of exposure in the Long Term Corrosion Test Facility at LLNL. These data are for simulated acidified water (SAW). Samples were placed in the aqueous phase (AQ), the vapor phase (VP), and at the water line (WL). Rates were below 1 micron per year. Data published by Haynes International for simulated crevice solutions (10 wt. % FeCl₃) is shown for comparison.

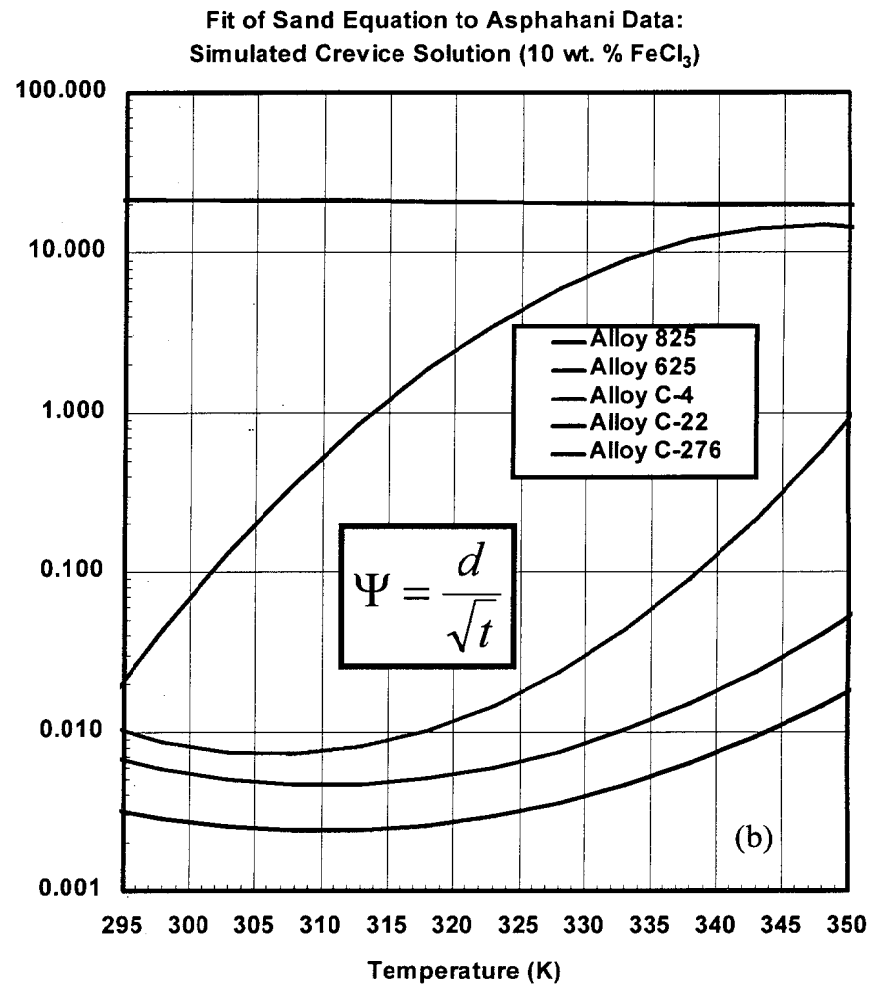
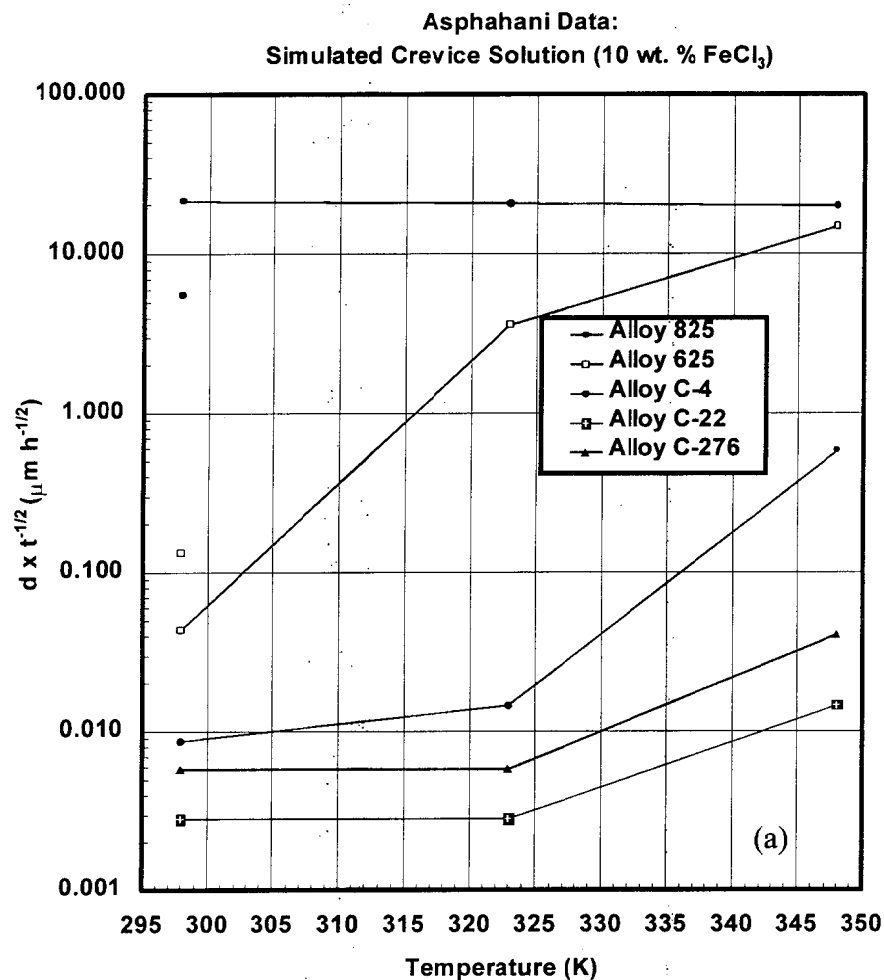


Figure 6. (a) Corrosion data published by Haynes International (Asphahani et al.) for exposure of candidate CRM's to simulated crevice solutions (10 wt. % FeCl₃). In each case, it was assumed that the time-dependent penetration would fit the Sand equation ($d = \Psi t^{1/2}$). (b) The apparent rate constant (Ψ) was fit to a polynomial of temperature since it did not appear to fit the classical Arrhenius expression. Observed rates for Alloys C-4, C-276 and C-22 are indicative of passive corrosion. Alloys C-276 and C-22 appear to exhibit the best corrosion resistance, probably due to the addition of both Mo and W.

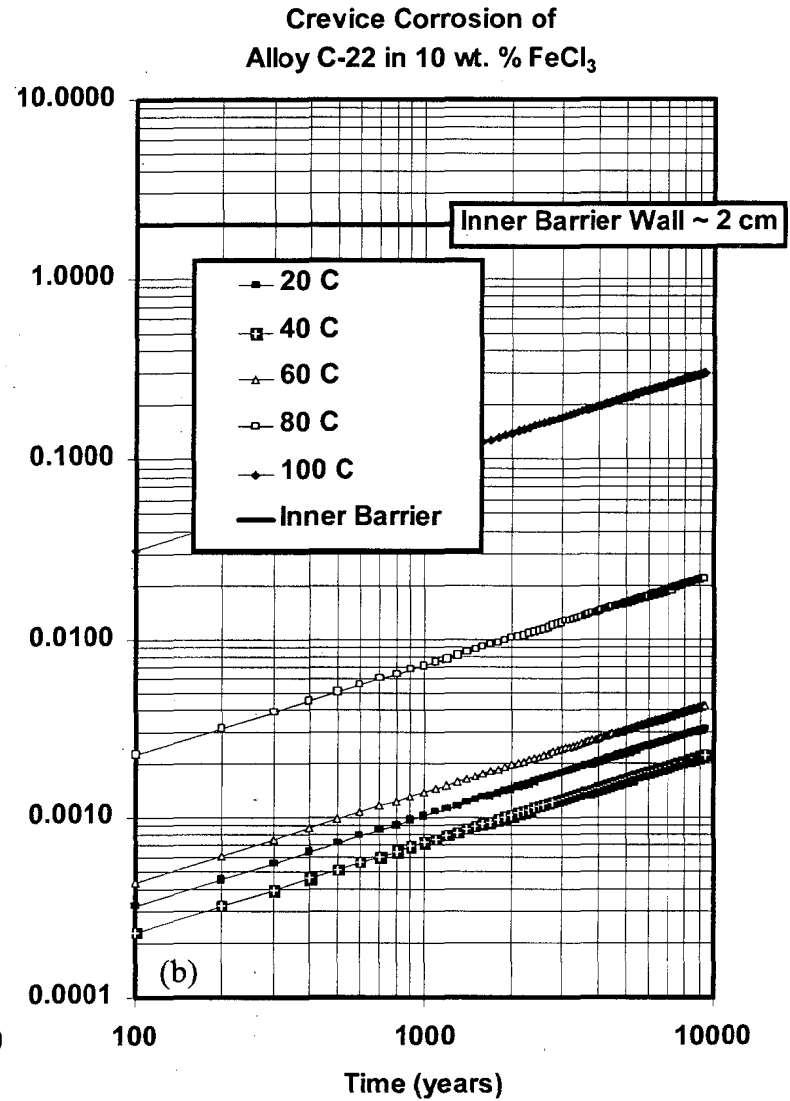
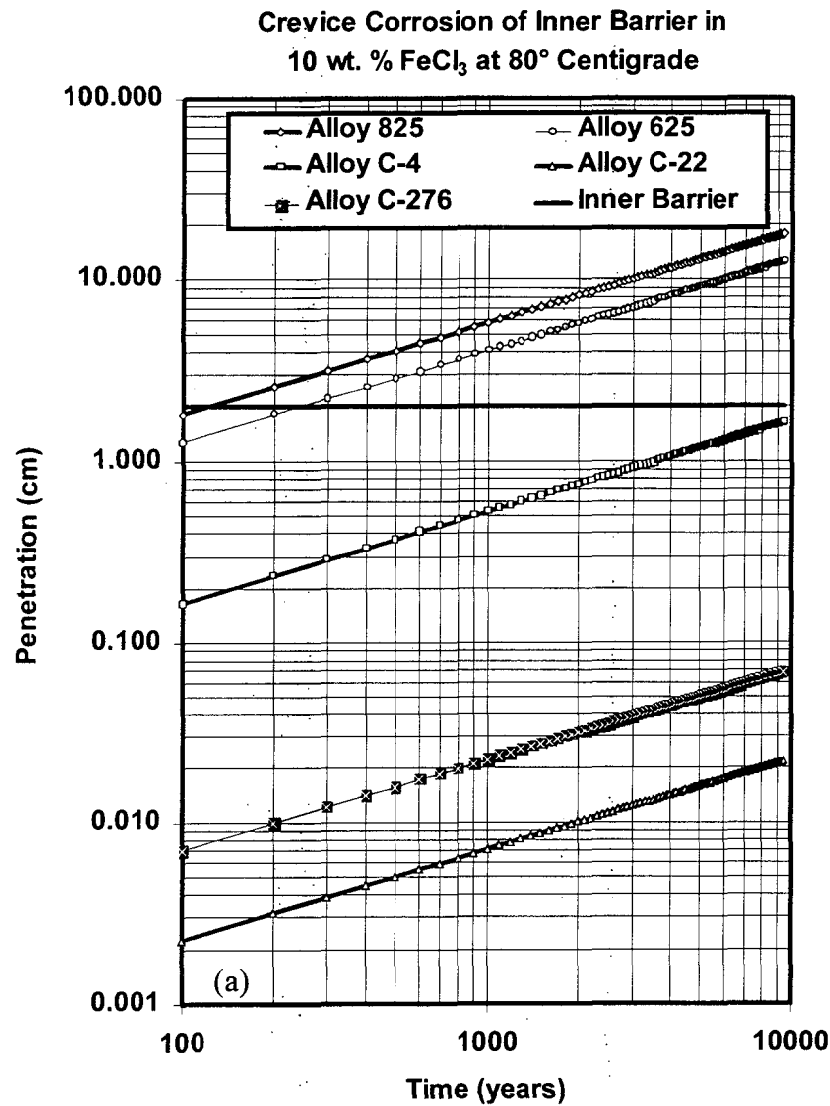


Figure 7. Extrapolations of corrosion data published by Haynes International (Asphahani et al.) based upon the analysis shown in Figure 6 (which assumes that $d = \Psi t^{1/2}$). Alloys C-276 and C-22 appear to exhibit the best corrosion resistance, probably due to the addition of both Mo and W. Based upon this simple bounding calculation, passive corrosion in the crevice would not be expected to penetrate an Alloy C-22 inner barrier during the first 10,000 years of emplacement.

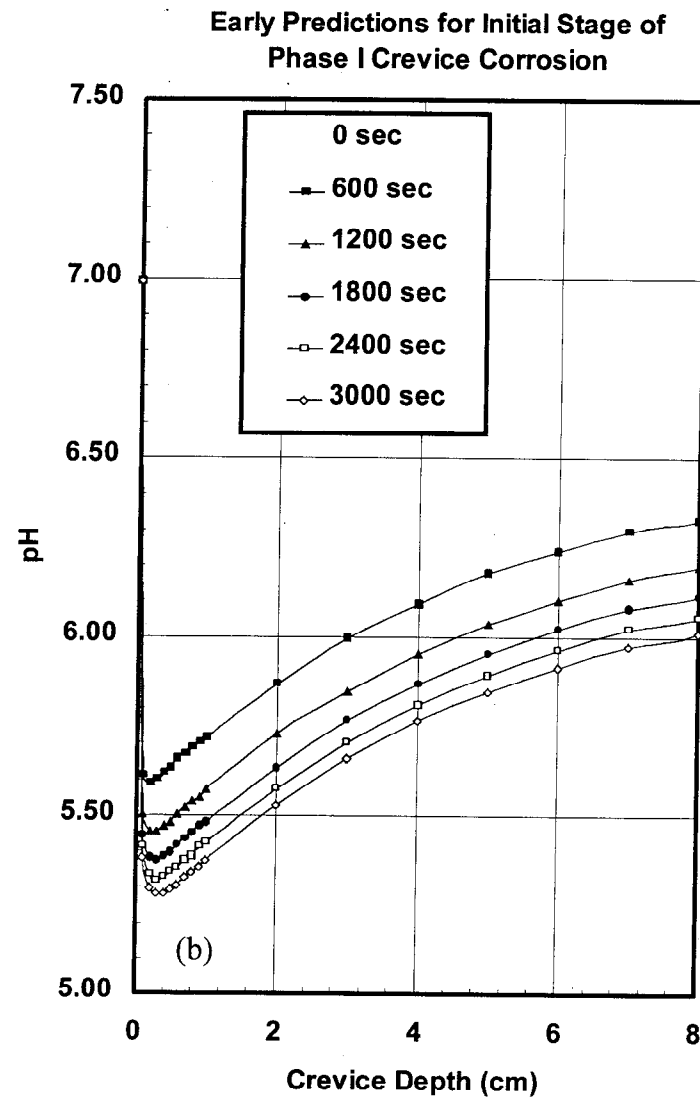
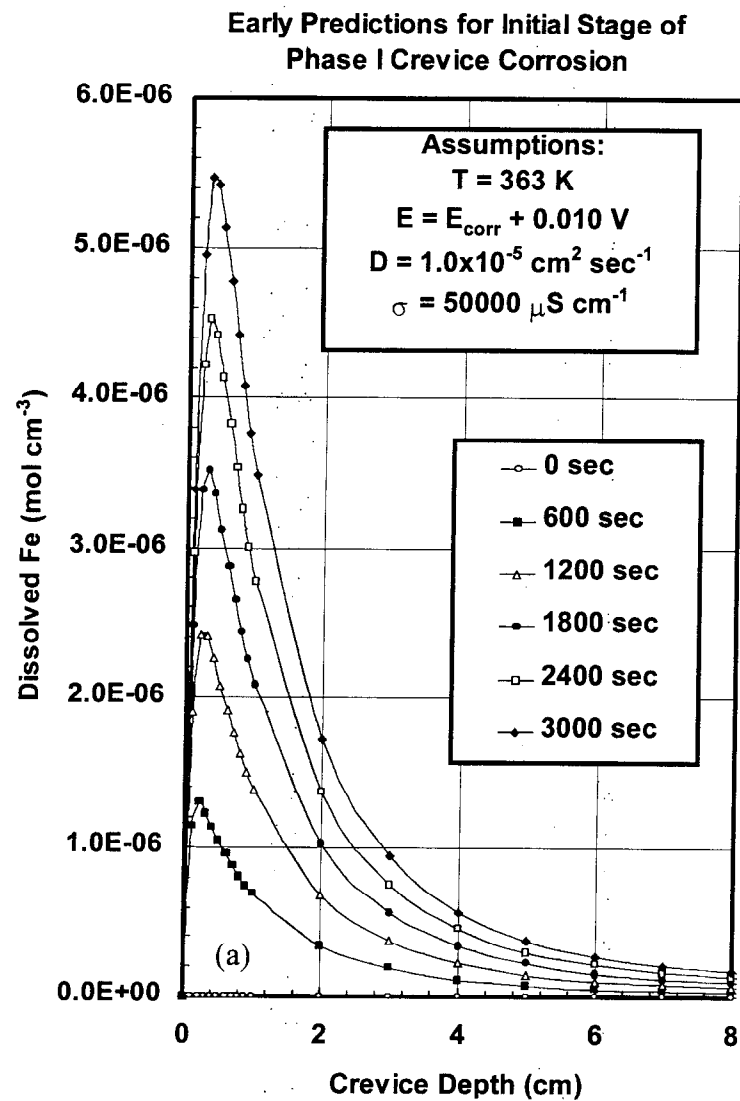


Figure 8. Transient concentrations of (a) dissolved iron and (b) hydrogen ion, given as pH, as functions of crevice depth during phase I crevice corrosion, which assumes preferential attack of CAM wall.

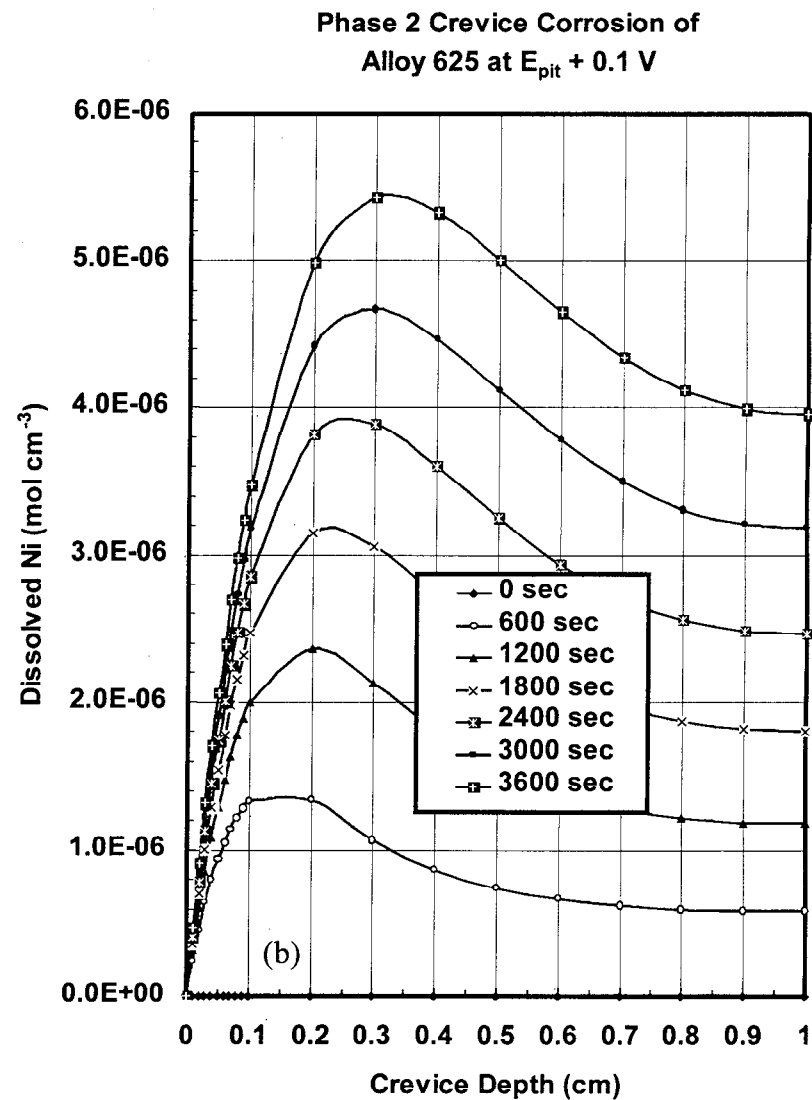
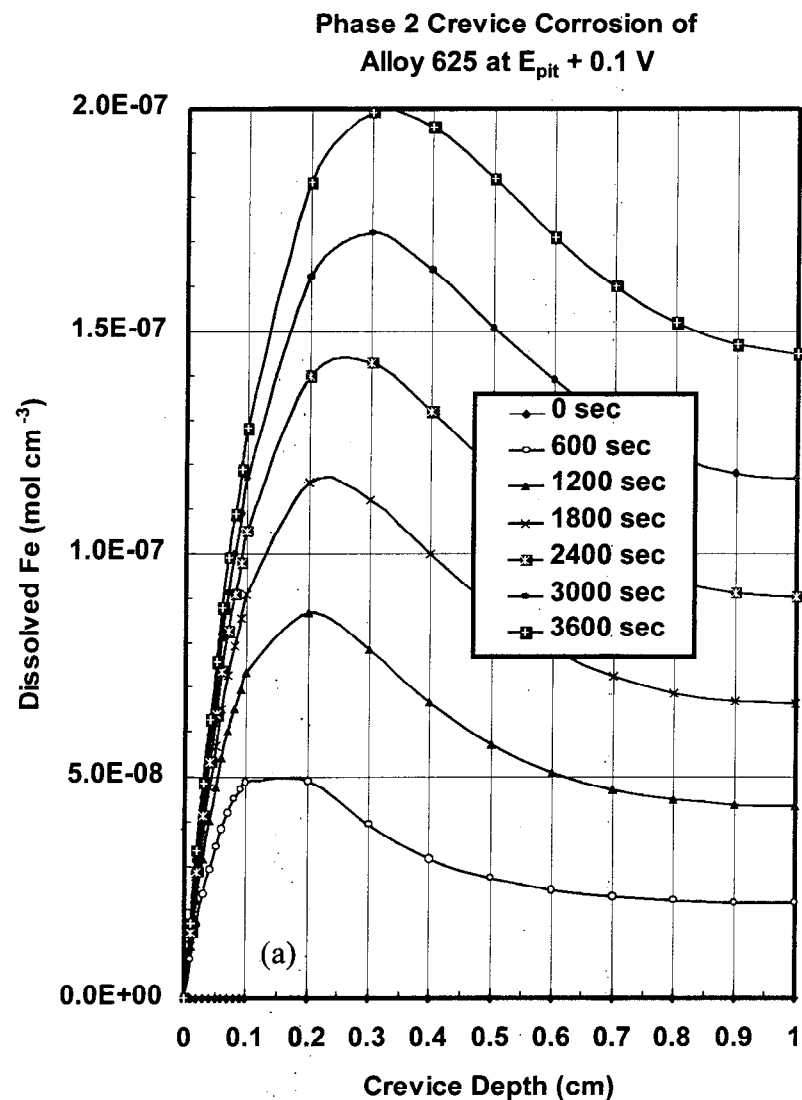


Figure 9. Transient concentrations of dissolved (a) iron and (b) nickel as functions of crevice depth during phase 2 crevice corrosion (attack of CRM). In this case it is assumed that the CRM is Alloy 625 and that electrochemical potential at the mouth of the crevice is maintained 100 mV above the critical pitting potential. Results for other metals not shown.

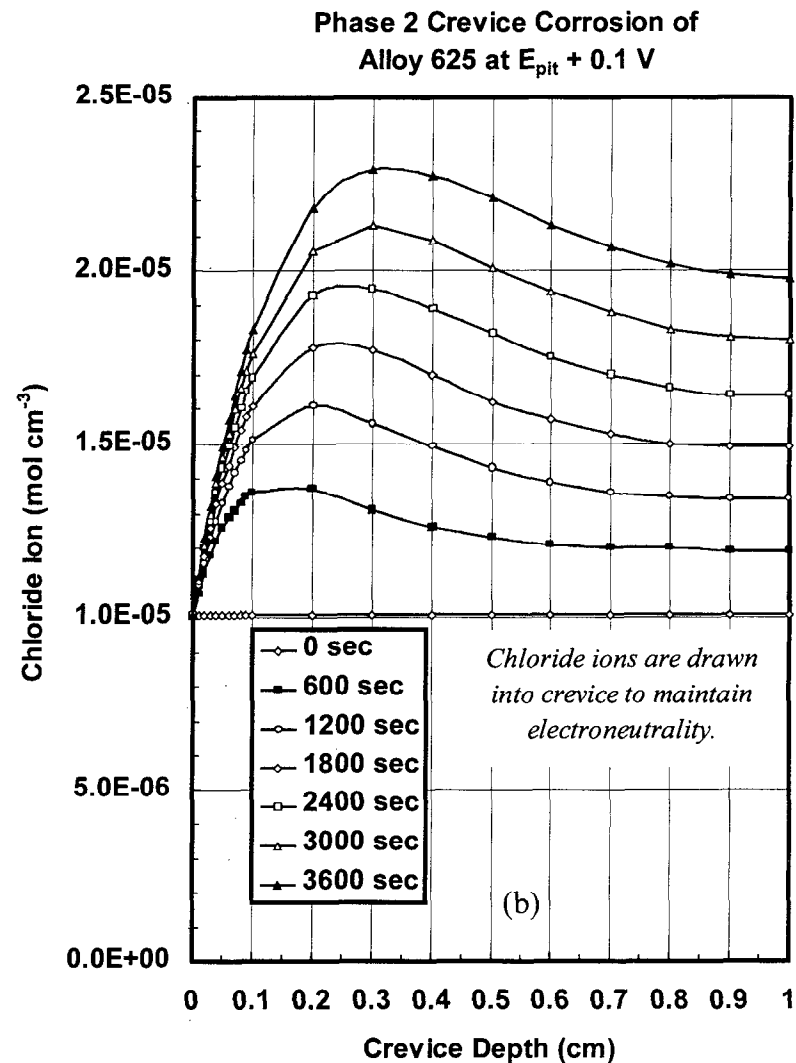
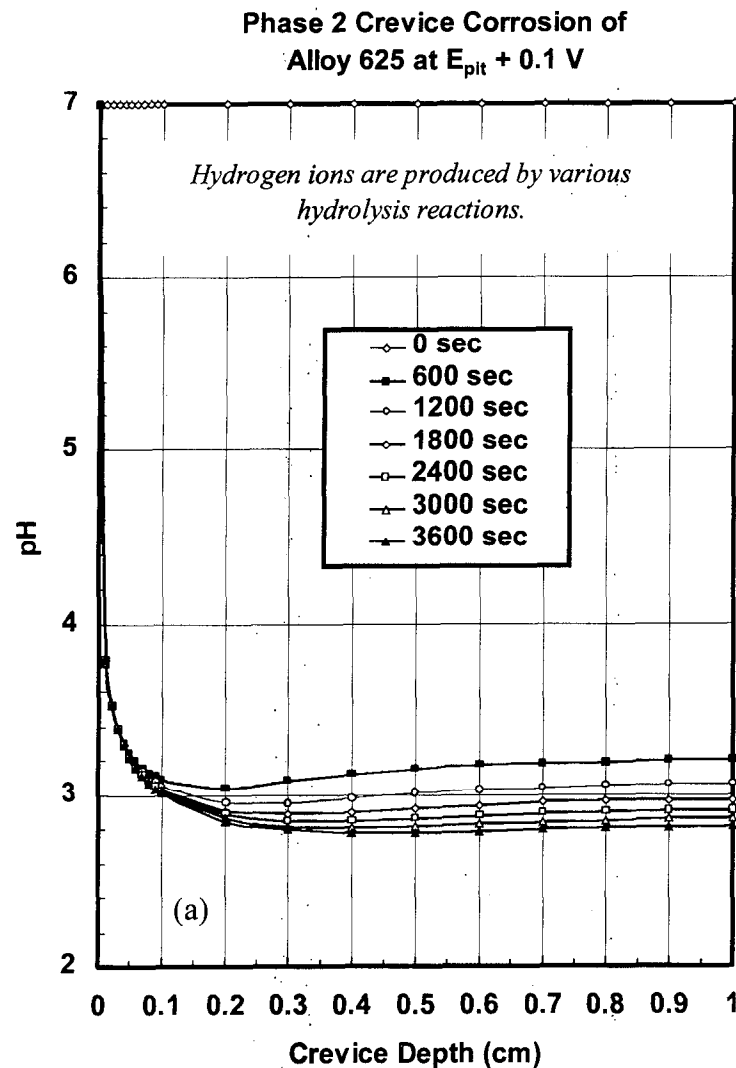


Figure 10. Transient (a) pH and (b) chloride anion concentration as functions of crevice depth during phase 2 crevice corrosion (attack of CRM). In this case it is assumed that the CRM is Alloy 625 and that electrochemical potential at the mouth of the crevice is maintained 100 mV above the critical pitting potential. Same calculation as Figure 9.

Potential becomes less damaging inside crevice.

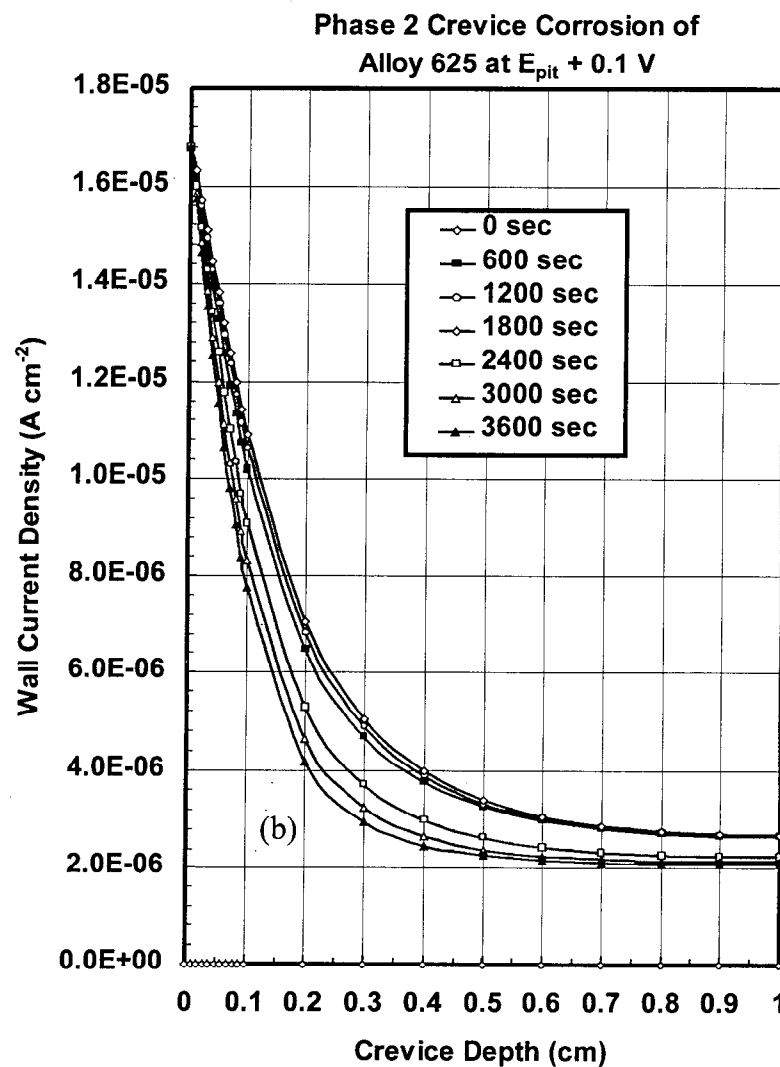
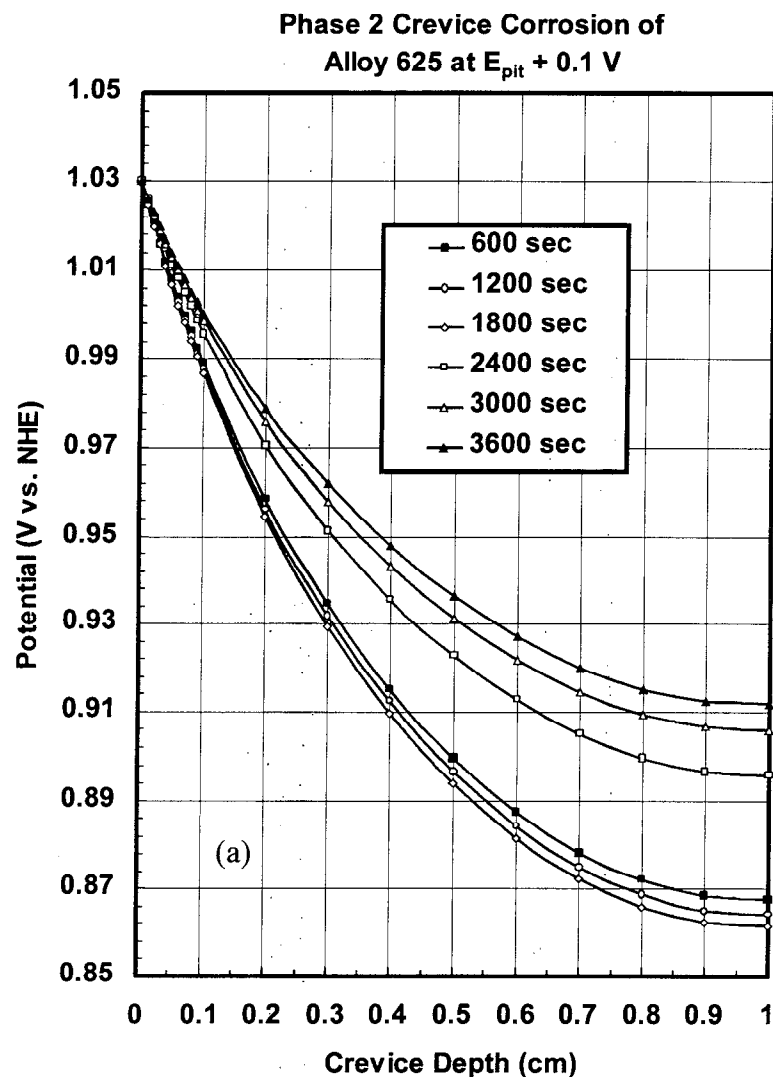


Figure 11. Transient (a) potential and (b) current density as functions of crevice depth during phase 2 crevice corrosion (attack of CRM). In this case it is assumed that the CRM is Alloy 625 and that electrochemical potential at the mouth of the crevice is maintained 100 mV above the critical pitting potential. Same calculation at Figures 9 and 10.

**New Fiber Optic Microsensor Developed by LLNL for
In Situ Determination of pH in Crevice**

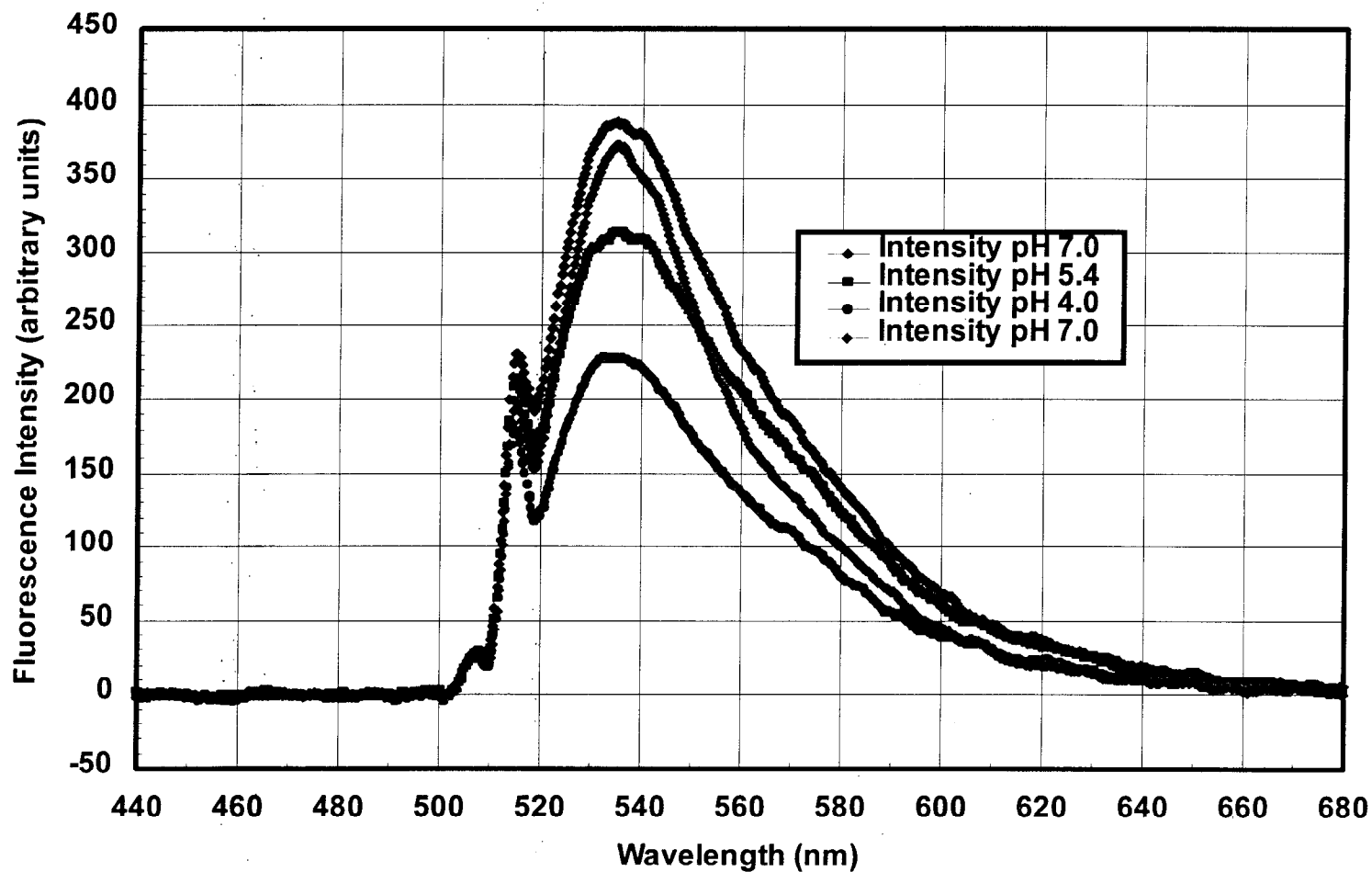


Figure 12. Results from new pH microprobe developed by LLNL for validation of the crevice corrosion model. The 488 nm line from an argon ion laser is used to induce pH-dependent fluorescence in a dye adsorbed at the tip of a fiber optic. The small peak at 514.5 nm is residual output from the laser, while the broadband centered at 535 nm is the fluorescence.

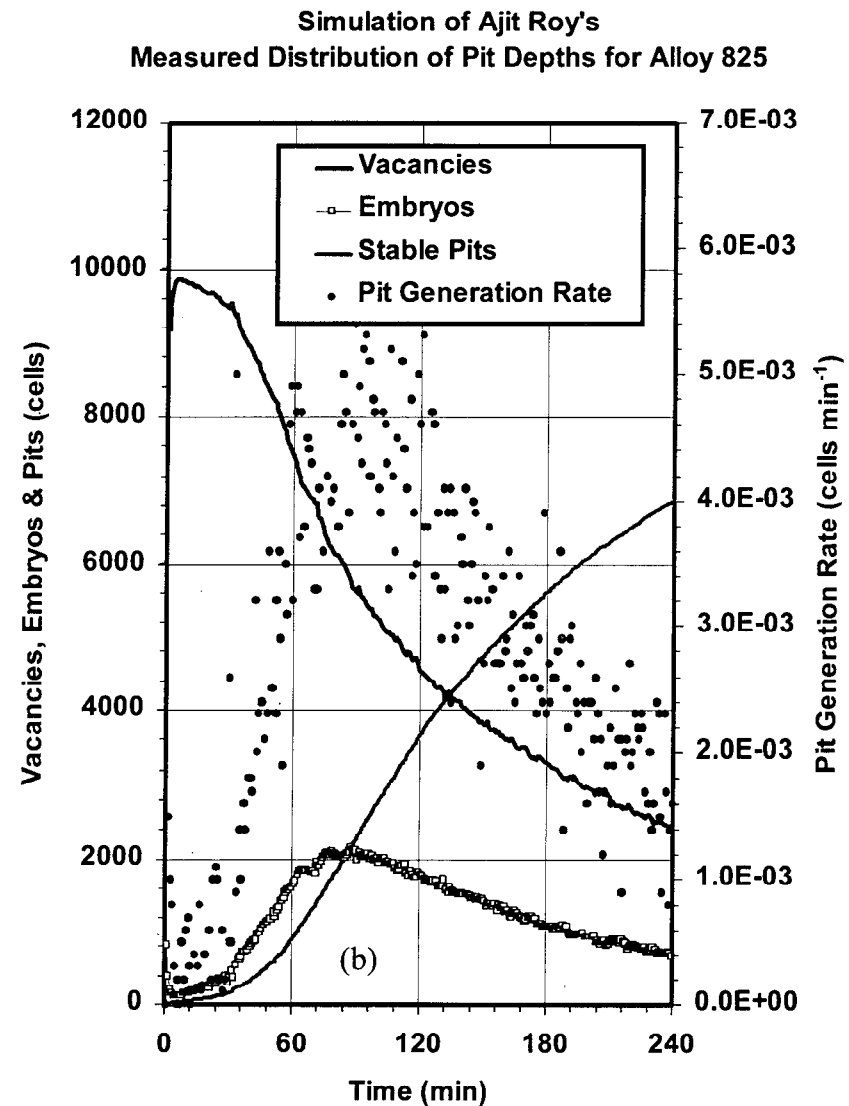
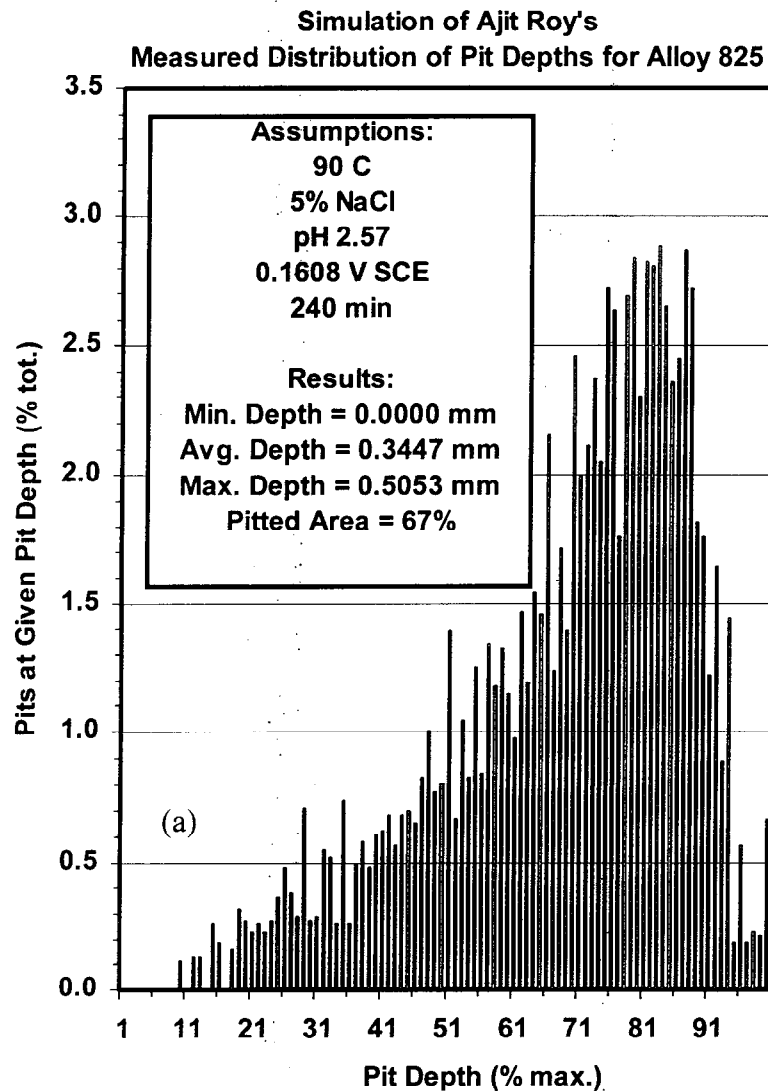


Figure 13. Use of probabilistic pit initiation model to simulate (a) the distribution of pit depth and (b) the fraction of pitted surface observed during experiments with Alloy 825 (data of Ajit Roy). Parameters in the model were adjusted so that the fractional coverage of the surface by stable pits, the average pit depth, and the maximum pit depth could be accurately predicted.

Effect of pH on Transients in Surface Coverage - Alloy 825

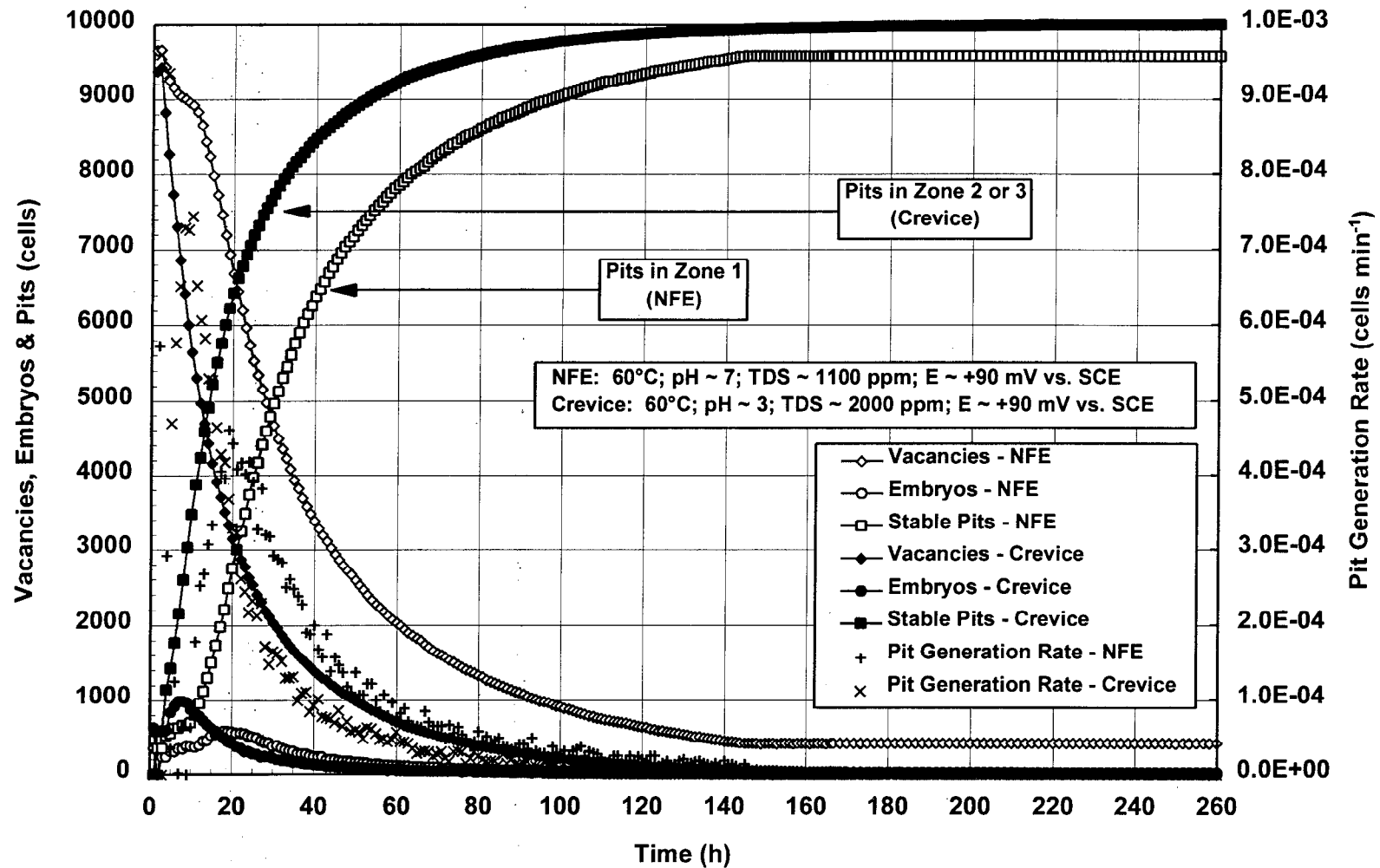


Figure 14. Application of the probabilistic pit initiation model to predict transients in the density of vacancies, embryos and stable pits during the polarization of Alloy 825 near the critical pitting potential. Predictions for two assumed cases are compared: 1100 ppm TDS and pH 7, assumed NFE; 2000 ppm TDS and pH 3, assumed crevice condition.

Effect of Potential on Transients in Surface Coverage - Alloy 825

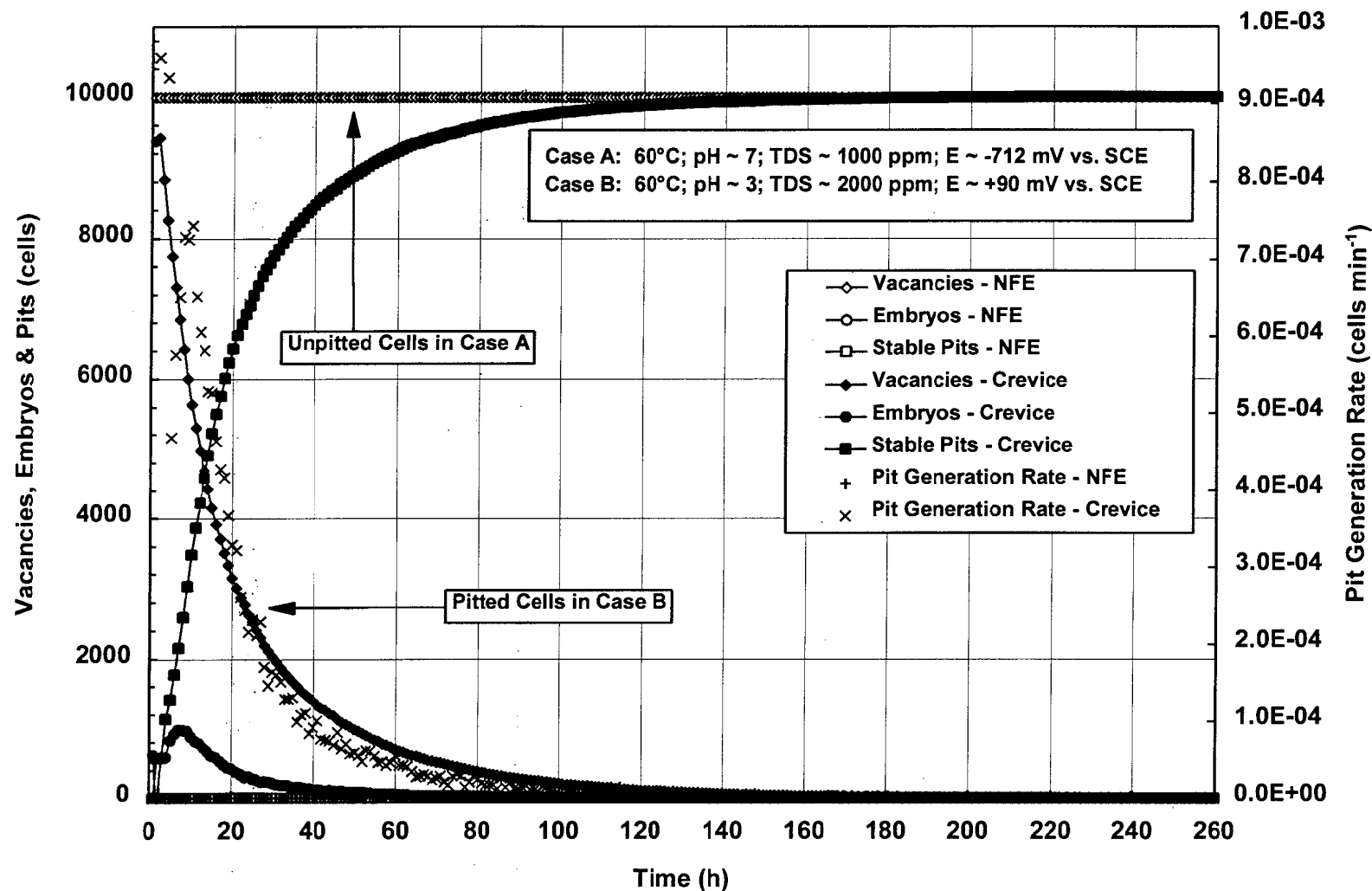
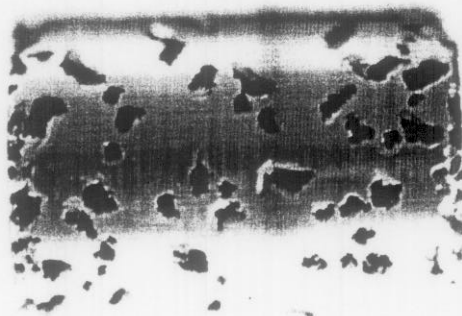
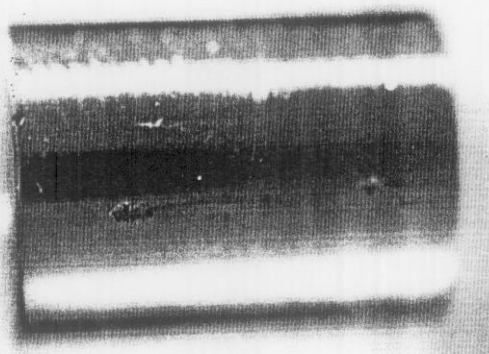


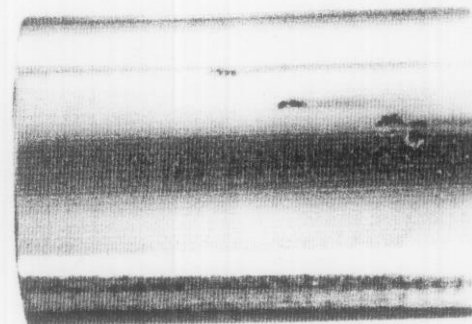
Figure 15. Application of the probabilistic pit initiation model to predict transients in the density of vacancies, embryos and stable pits at 60°C. Predictions for two assumed cases are compared: [Case A] 1000 ppm TDS, pH 7, and -712 mV SCE (the corrosion potential of CAM); [Case B] 2000 ppm TDS, pH 3, and +90 mV vs. SCE (pitting potential of CRM).



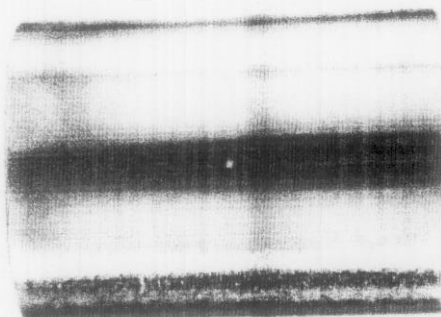
Alloy 825



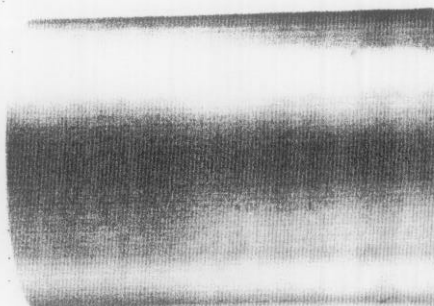
Alloy G-3



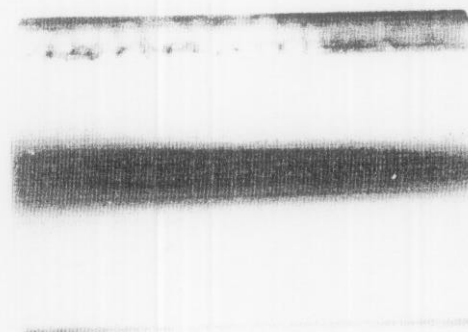
Alloy G-30



Alloy C-4



Alloy C-22



TiGr-12

Figure 16. Photographs of candidate CRM materials subjected to severe polarization in acid chloride solutions (LLNL data collected by Ajit Roy). Alloy 825 is much more prone to pitting than Alloy C-22. It is believed that no pitting of Alloy C-22 has been observed below the repassivation potential, which is assumed to be the threshold for localized corrosion.

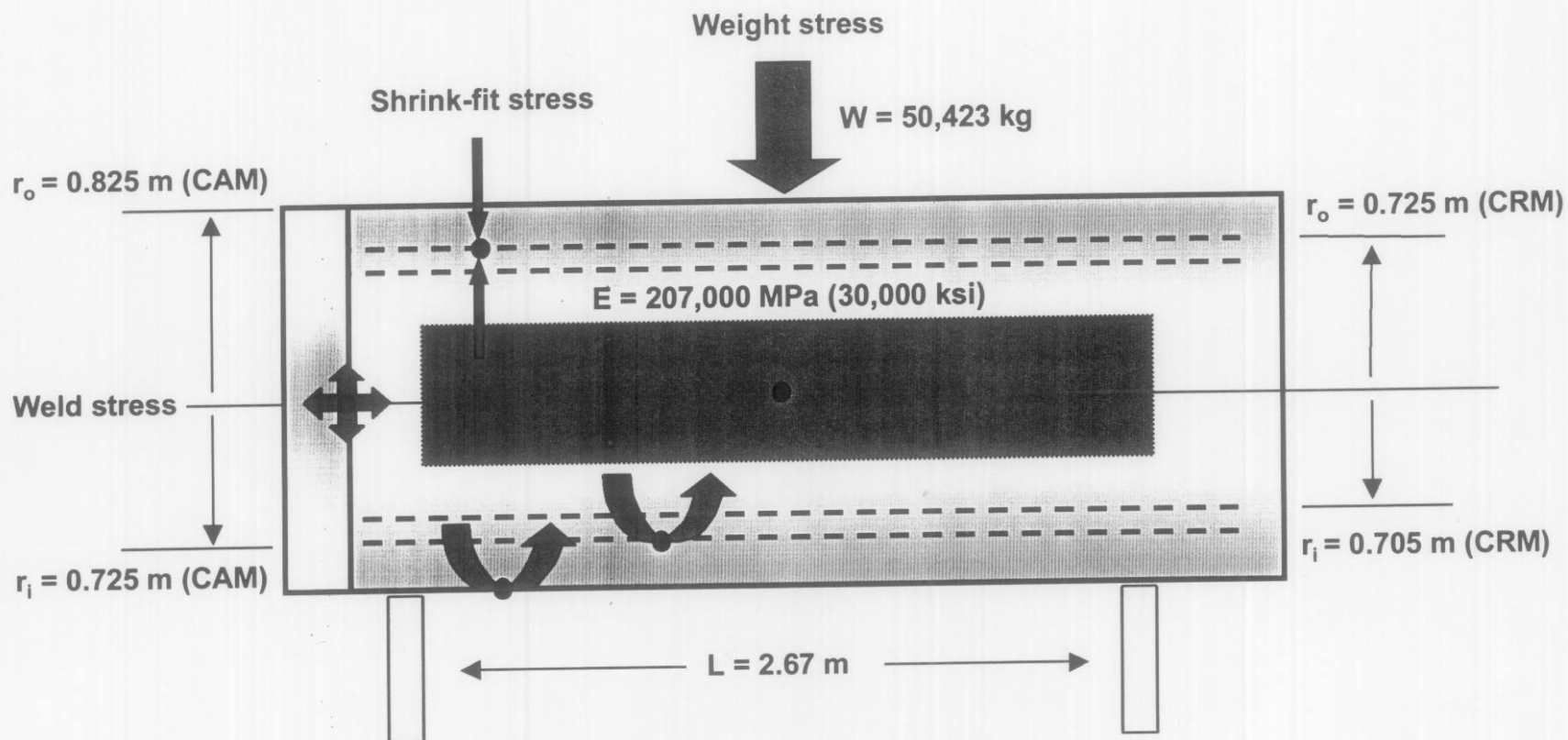


Figure 17. There appear to be three contributions to the overall stress in an unperturbed, horizontally-placed high-level waste container that could promote stress corrosion cracking (SCC). These are the weight stress, the weld stress, and the shrink-fit stress. Note that r_o is the outer radius of the outer barrier (CAM), r_i is the outer radius of the inner barrier, R is the inner radius of the outer barrier, L is the length of the container between supports, and E is the modulus (CAM or CRM).

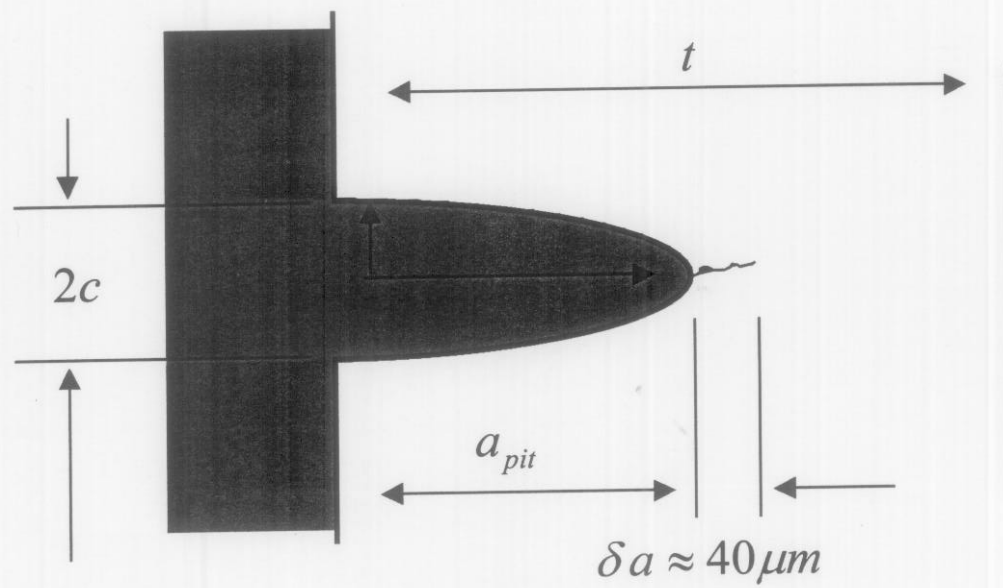


Figure 18. Conceptual representation of the ideal flaw (pit or other imperfection) that was used as the basis for calculating the critical flaw size for initiation of stress corrosion cracking (SCC)

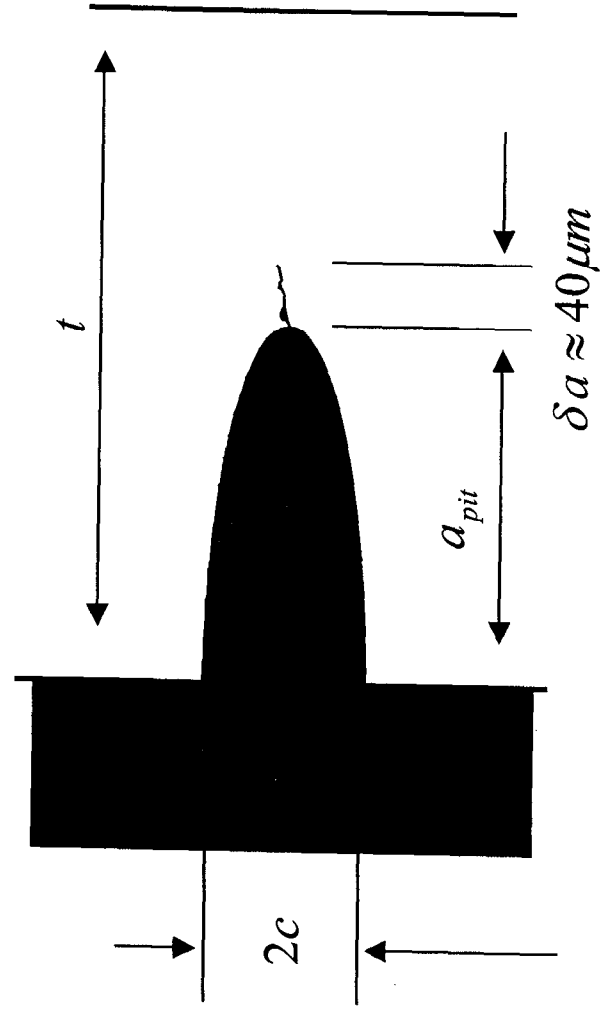


Figure 18. Conceptual representation of the ideal flaw (pit or other imperfection) that was used as the basis for calculating the critical flaw size for initiation of stress corrosion cracking (SCC)